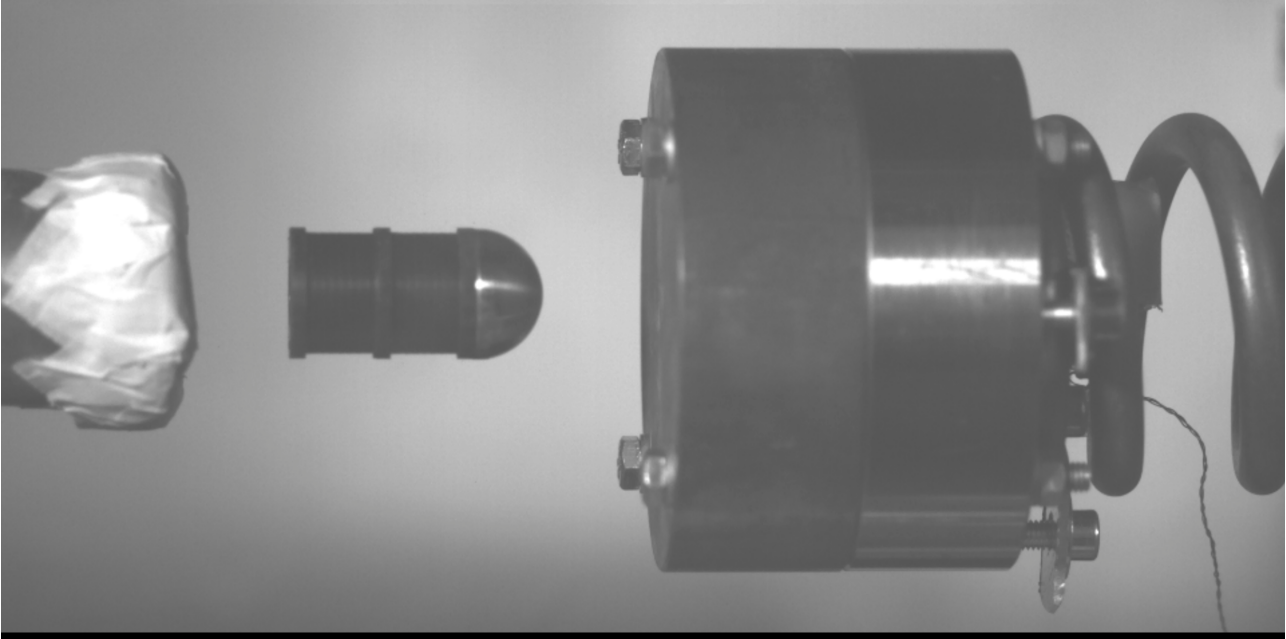

Can Hail Impacts Trigger Delaminations?

Master of Science Thesis

S. Ganesh Ram

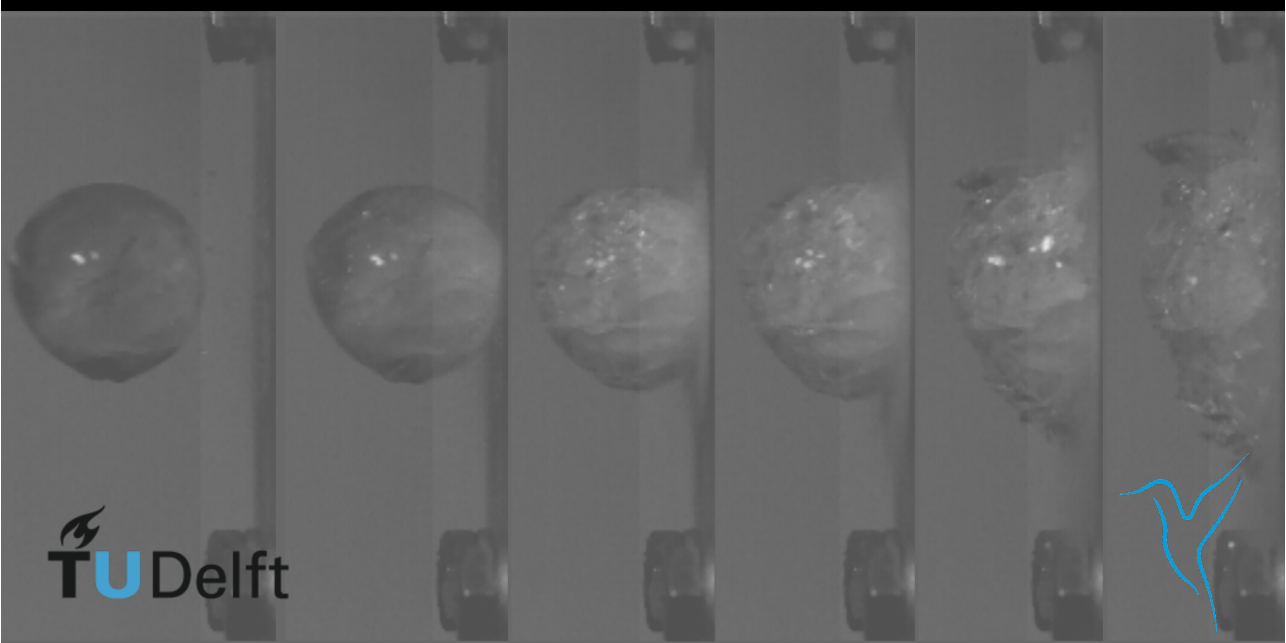

TU Delft

CAN HAIL IMPACTS TRIGGER DELAMINATIONS?

A qualitative study to evaluate the consequences of hail ice impact on composite structures.

by

SRINIVASAN GANESH RAM

in partial fulfilment of the requirements for the degree of

Master of Science
in Aerospace Engineering

at the Delft University of Technology,
to be defended publicly on Wednesday August 18, 2021 at 9:30 AM.

Student number:	5004993	
Project duration:	Nov. 16, 2020 - Aug. 18, 2021	
Thesis committee:	Prof. Dr. ir. René Alderliesten	Chair
	Prof. Dr. Christos Kassapoglou	External Examiner
	Dr. Sofia Teixeira De Freitas	Examiner

TU Delft Delft University of Technology

PREFACE

This document was written to fulfil the requirements for obtaining the Master of Science degree in Aerospace Engineering at the Delft University of Technology. This thesis project is the conclusion of my two years of study in Delft. Working on this project gave me a sense of normalcy and focus in an otherwise tumultuous year courtesy of the COVID-19 pandemic. While there were both high and low points, I walk away from this with a feeling of achievement and fulfilment. This would most definitely not be possible without the support of the people around me.

First of all, I would like to express my immense gratitude to my supervisor, Dr. ir. René Alderliesten. Throughout the last year I have received a vast amount of support, insight and guidance from him. Our meetings were always something to look forward to and a great source of motivation. His feedback and critical questions have shaped this project to what it is today. Secondly, I would like to express my gratitude to all the technicians from the Delft Aerospace Structures and Materials Laboratory (DASML). All of them made me feel welcome throughout the project and helped me out in several critical stages. Thank you Casper van Diën, Victor Horbowiec, Fred Bosch, Dave Ruijtenbeek, Alexander Uithol, Berthil Grashof, Durga Mainali and Ed Roessen. I would be amiss in my duties without extending a special thanks to Alexander Uithol for his constant support and insightful conversations over the last few months. A similar thanks to Lubin Huo for the insightful conversations and guidance.

Furthermore, I would like to thank my parents for their unconditional support and encouragement throughout my academic journey. My sincere gratitude to all the friends I made in Delft and to those back home for their uplifting company. Finally, I owe a special thanks to Nikoleta Pasvanti for her constant encouragement and support that helped me salvage my not so productive days. I am where I am thanks to all of you.

Srinivasan Ganesh Ram
Delft
Aug. 18, 2021

ABSTRACT

The current generation of commercial aircrafts extensively use composite materials such as Carbon Fibre Reinforced Polymers (CFRP) in both exposed and primary structures. These materials lack through-thickness reinforcement and are hence susceptible to out-of-plane impact damages. Barely visible impact damage caused by low energy impacts poses a unique problem, since delaminations, de-bonding and cracking may be present below the surface layers without any indication of damage on the surface. The focus of this research is on one such scenario, multiple site low energy hail impacts, while the aircraft is on the ground. Taking into account the relevant parameters, a hail impact envelope was established both in terms of the initial kinetic energy and peak impact force. Further, contradictions found in literature over the influence of the compressive strength of hailstones were resolved. These were accomplished with the aid of a state-of-the-art finite element model and experiments in the laboratory. With help from a custom designed and assembled impact force measurement experimental setup a relation was established between impacts carried out with steel impactors and those with simulated hail ice impactors. Based on this relation, predictions are made on which hailstones have the potential to cause damages to CFRP structures.

NOMENCLATURE

ACRONYMS

BVID	Barely Visible Impact Damage
FAA	Federal Aviation Administration
EASA	European Union Aviation Safety Agency
FRP	Fiber Reinforced Polymer
CFRP	Carbon Fiber Reinforced Polymer
ASTM	American Society for Testing and Materials
ESWD	European Severe Weather Database
ESSL	European Severe Storms Laboratory
IBHS	Insurance Institute for Business and Home Safety
SHI	Simulated Hail Ice
ASTM	American Society for Testing and Materials
ANSI	American National Standards Institute
FMT	Force Measurement Transducer
FTE	Failure Threshold Energy
KE	Kinetic Energy
SPH	Smoothed Particle Hydrodynamics
TDSFE	Time Domain Spectral Finite Element
DASML	Delft Aerospace Structures and Materials Lab
HPC	High Performance Computing
UTM	Universal Testing Machine
IESIM	Ice Equivalent Steel Impactor Model
HSC	High Speed Camera
LDS	Laser Displacement Sensor
MRO	Maintenance, Repair & Overhaul

SYMBOL LIST

m	Mass [g]
D_{max}	Maximum dimension [cm]
ρ_{ice}	Density of ice [kg/m^3]
V_{eq}	Equivalent volume of SHI [cm^3]
D_{eq}	Equivalent diameter of SHI [cm]
v_{ter}	Terminal velocity [m/s]
g	Acceleration due to gravity [m/s^2]
C_d	Coefficient of drag [-]
ρ_{air}	Density of air [kg/m^3]
$N(D)$	Number of hailstones [m^{-2}cm^{-1}]
D	Diameter [cm]
λ	Slope [cm^{-1}]
N_0	Intercept [m^{-2}cm^{-1}]
F_c	Contact force [N]
k_n	Non-linear stiffness coefficient [-]
p	Characteristic exponent [-]
COR	Coefficient of restitution [-]
m_1	Mass of impactor [kg]
v_0	Impact velocity [m/s]

CONTENTS

List of Figures

List of Tables

INTRODUCTION

The current generation of commercial aircrafts are extensively using composite materials such as Carbon Fiber Reinforced Polymer (CFRP) in both exposed and primary structures. The high specific strength and stiffness, tailorable nature and part integration possibilities make this material extremely attractive to aircraft manufacturers looking to save weight at every possible instance. Naturally, both Boeing and Airbus have escalated its usage, with the 787 and A350 family of aircrafts containing upto 52% reinforced plastics by weight [16].

However, it is essential that the safety levels historically provided by aluminium alloys are not reduced by the introduction of CFRPs. Given these materials lack through-thickness reinforcement, damage resistance in the transverse direction is especially low, making them susceptible to out-of-plane impacts [17]. Hail, tool drops, luggage drops and runway debris are some sources for such impacts, that can eventually result in delaminations and de-bondings in composite parts. Such damages based on severity may have serious consequences to the structural integrity of the aircraft, and hence the trifecta of damage tolerant design, early damage detection (primarily visual inspection) and timely repairs is currently employed by manufacturers and maintenance organisations [18, 19].

In this context, Barely Visible Impact Damage (BVID) caused by low energy impacts poses a unique problem, since delaminations, de-bonding and cracking may be present below the surface layers without any indication of damage on the surface. While damage caused by a single impact may be accounted for in the design, repeated impacts at low energy within the vicinity of each other may lead to the link up of damages leading to damage sizes not currently accounted for. One such scenario is multiple site low energy impacts from hail ice while the aircraft is on the ground, that has in the past led to damages, expensive inspections and repairs [20–24]. Hence a more in-depth understanding of the risk posed by hail ice will aid engineers with both developing better designs and predicting the extent of damage current structures can endure.

This study aims to deepen the current understanding of the hail threat, spread over four parts. The first part attempts to unearth the state-of-the-art of the current understanding of the hail threat and builds upon it to establish scenarios relevant to commercial aircrafts on the ground. It also identifies and plugs gaps existing in current literature. The second part attempts to establish a relation between ice impacts and impacts made using steel, given most CFRP impact experiments in the past were carried out using steel. The third part highlights key takeaways and potential implications of this study through the conclusions and recommendations. The last part is the appendix containing additional data that may be useful for future research.

I

Background & Hail Threat Analysis

INTRODUCTION: PART I

This part attempts to unearth the state-of-the-art of the current understanding of the hail threat and builds upon it to establish scenarios relevant to commercial aircrafts on the ground. The first chapter comprises of the literature study which looks into several aspects relating to our current understanding. One section addresses the risk of hail by looking at current certification regulations and the characteristics of naturally occurring hail to form some generalisations that can be used for further investigations. The other section looks at the evolution of methodologies of testing and modelling hail through the years. The actionable points from this chapter are summed up into research questions in the second chapter. The third and fourth chapter attempt to address these research questions through both numerical modelling and experiments in the Delft Aerospace Structures and Materials Lab (DASML).

1

Literature Review

1.1. Hail Threat

1.1.1. Hail Risk Analysis

This subsection provides an overview of the current regulations regarding the risk posed to aircraft by hailstones and possibilities for an aircraft on the ground to encounter hail.

Manufacturers & Regulators

The Composite Damage Tolerance and Maintenance Workshop hosted by the Federal Aviation Administration (FAA) provides some preliminary insights on the approach of the major commercial aircraft manufacturers, Airbus and Boeing towards safeguarding composite structures against the threat of ground hail [25].

Airbus defines BVID as damages below the threshold that is surely detectable by scheduled inspection corresponding to a 90% probability of detection and a 95% confidence in the interval. Design philosophy here is to sustain the ultimate load even in the presence of BVID. Further, consideration is given to the hail threat by categorising hailstorms based on severity and probability of occurrence. It is of note that the maximum diameter of hailstone considered is $5cm$, accompanied by a velocity of $33m/s$ and Kinetic Energy (KE) of $32J$ at impact [26].

Boeing defines BVID as small damages that may not be identified during visual inspections using conventional lightning conditions from a distance of approximately $1.5m$ ($5ft$). Design philosophy here derives static strength of the structure in question as a function of BVID. Here too consideration is given to the threat posed by hail, with the performance requirement set to the retention of ultimate design strength, nil moisture intrusion and no damage growth within the design service objective. It is of note that the maximum KE considered here is $56.5J$ ($500in-lb$) for a simulated hailstone [27].

Both the European Union Aviation Safety Agency (EASA) and the FAA in their airworthiness regulations on Composite Aircraft Structures [28, 29] require test evidence

to demonstrate that impact damage sustained during manufacturing and service does not reduce the structural strength below ultimate load capability. Further, it is stipulated that the size and shape of the impactors used for this demonstration must be consistent with likely impact damage circumstances that may not be identified through the course of the aircraft's service life. While hail is listed as one of the possible foreign object impacts in the damage threat assessment, no specifics are offered, leaving room for interpretation on the severity of ground hail events to the manufacturers. It is further unclear if tolerance to multiple site damage (blunt impacts from ground hail for example) and possible BVID link-up is a requirement for certification.

A study [7] commissioned by EASA with the goal of creating a global hail threat model based on meteorological data and information available at the time on aircraft structures, provides the following insights. (1) In the development of certification standards careful consideration must be given to a range of hail masses and velocities in order to account for all possible composite failure modes; (2) For the testing of aircraft materials a simple reproducible hailstone equivalent is required. While ice sphere impactors may represent a worst case scenario, metallic sphere impactors do not adequately represent the damages created by hailstones. (3) Aircrafts on the ground may be susceptible to impacts from hail sizes up to $11cm$ in diameter. (4) Multiple hits within each others vicinity by hailstones with diameters smaller than $5cm$ and damage linkup resulting from this are both possibilities to be considered in the design phase.

AIRPORTS IN HAIL AFFECTED AREAS

Figures 1.1 & 1.2 are maps of all the routes operated by the Boeing 787 Dreamliner and the Airbus A350 family of aircrafts in the years 2019 and 2018 respectively. For this study, the airports connected by these routes are of more consequence than the routes themselves.

Figure 1.1: Boeing 787 Dreamliner family flight routes in 2019 [1]

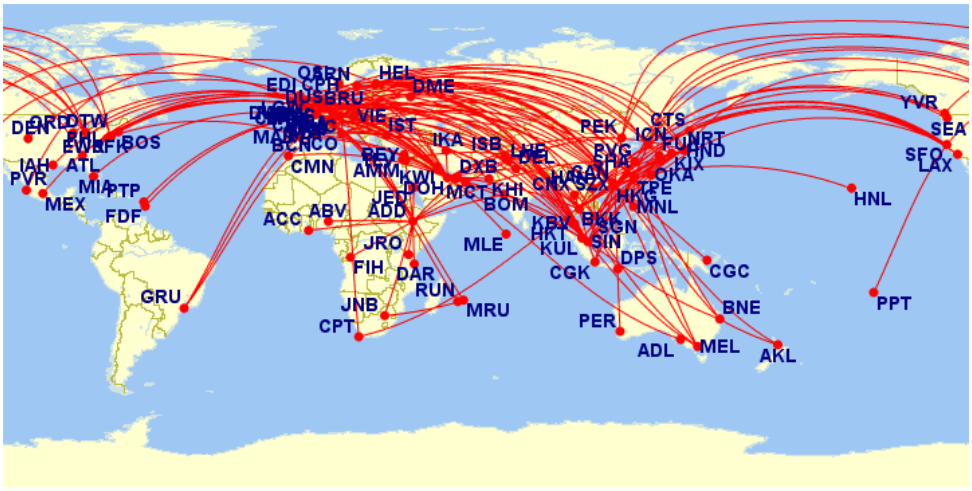

Figure 1.2: Airbus A350 family flight routes in 2018 [2]

In the past, studies [30] attempting to estimate global hail threat have relied primarily on eye witness accounts and hailpads [31] which would imply that the data gathered would be biased towards more populated regions. Given the highly localised nature of hail in tandem with the fact that it does not remain in a solid state for long, this measurement methodology clearly has its limitations. Given this context, recently a model which uses large scale environmental factors such as atmospheric instability, freezing level height, wind shear data and storm relative helicity was developed to make more unbiased estimates of the global hail threat [3]. This model was found to compare well with existing eyewitness and measured data for both the United States and Europe, though uncertainties start to emerge for tropical regions. Figure 1.3 is the result of this model, and maps out the number of annual large hail days across the globe for the period 1979 to 2015. Large hail days are defined as the number of days hailstones larger than $2.5cm$ were predicted. A comparison of figures 1.1, 1.2 & 1.3 demonstrates the intersection of airport locations with hail prone areas in both the United States and Europe. Further two specific cases can be made out for the Finnair and Lufthansa A350 fleets that operate out of Helsinki and Munich respectively [2], both areas with a recorded history of hailstorms [32, 33].

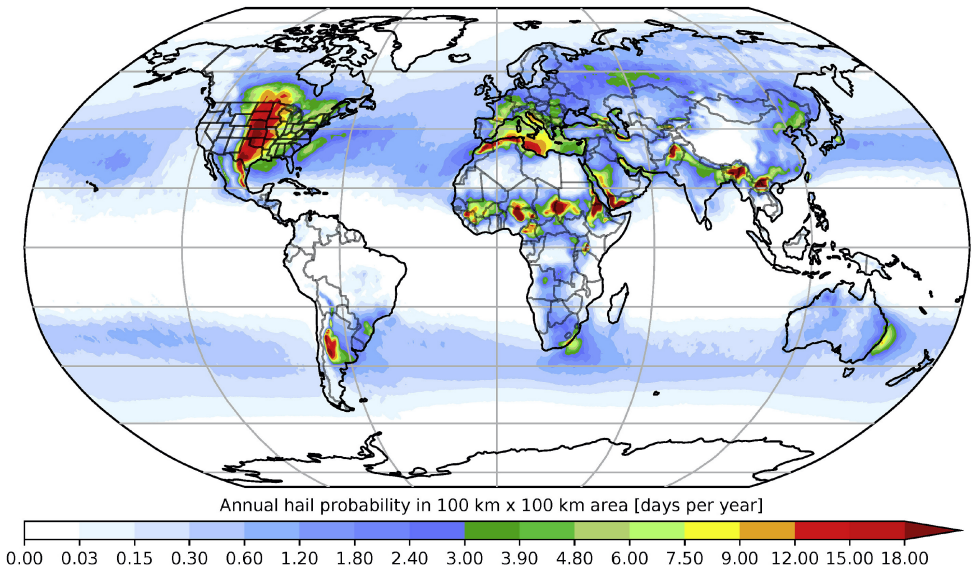

Figure 1.3: Annual probability of large hail days across the globe [3]

Though a large part of this problem statement has been centred around the Boeing 787 Dreamliner and the Airbus A350 it is important to note that, numerous other aircrafts from Boeing (777, 737), Airbus (A380, A320) and other manufacturers also utilise CFRPs for various exposed components [7, 34]. To add to this several incidents have been reported in the past where aircrafts with composite components have encountered hail while on the ground and had to undergo expensive inspections and repairs [20–24]. The special circumstances introduced by COVID-19 resulting in numerous aircrafts being parked in open air spaces [35] only exacerbates the risk of an aircraft encountering a ground hail incident. Recent research into the changing melting level height due to global warming forecasts a 40% increase in hail intensity by 2040 [36]. Under these circumstances a closer look at the potential damages caused by hailstones on CFRP aircraft structures is definetly warranted.

1.1.2. HAIL CHARACTERISTICS

This subsection explores true hail data to ascertain the parameters that should be take into account to effectively replicate the hail impact phenomenon in a laboratory setting.

SIZE

Across literature, $0.5cm$ maximum dimension is regarded as the transition point between graupel and hail, and hence this is considered as the lower limit going forward [37]. In Europe, the European Severe Storms Laboratory (ESSL) in 2006 established the European Severe Weather Database (ESWD) which is a network of voluntary observers and meteorological services across the continent tasked with collecting reports of severe

weather events, including large hail occurrences [38]. Careful analysis of this data by researchers in the ESSL [4] has provided a number of useful insights. Almost 40% of the reports collected that included information about the maximum hail dimension, were for hailstones ranging between $2-2.9cm$. While less than 10% of these reports were of hail sizes larger than $5cm$, the largest reported hailstone in the recent past is $15cm$ in diameter. These occurrences are plotted in figure 1.4. In the context of Europe, the $15cm$ maximum diameter hailstones get multiple mentions in a 2016 review of hail observations and characteristics as well [37].

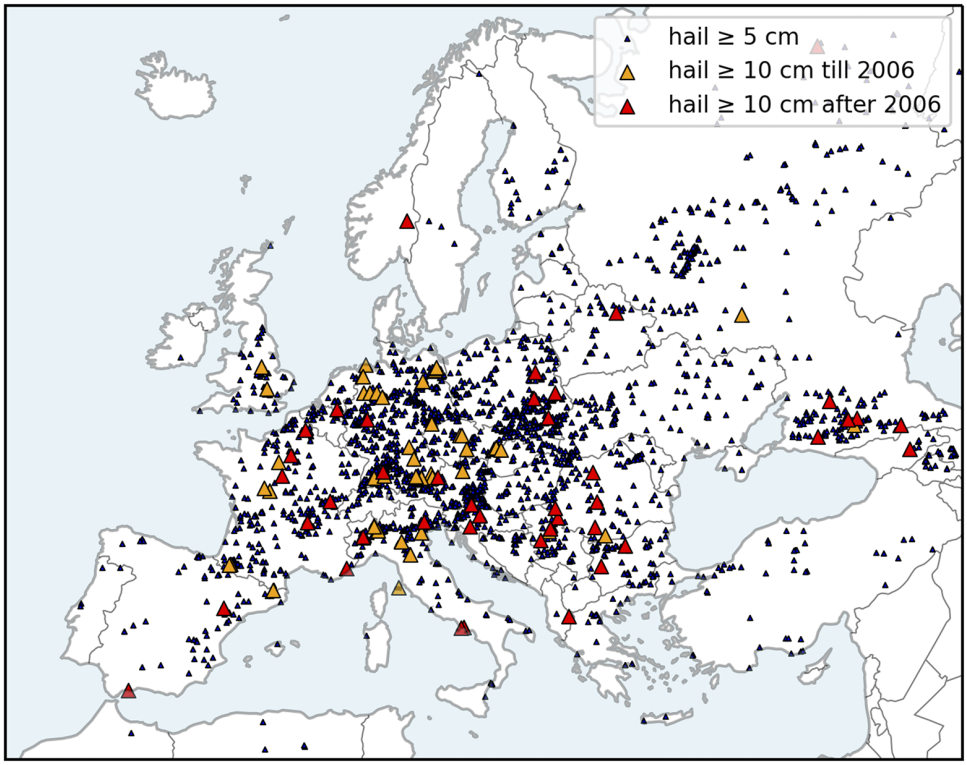

Figure 1.4: Documented large hail occurrences across Europe from the ESWD [4]

In order to further the understanding of the damage caused by hail on building roofs, the Insurance Institute for Business and Home Safety (IBHS) launched a research program in 2010 [39]. Though the goal of this work was towards developing a new testing methodology for the impact resistance of asphalt roofs, the field work conducted between 2012 and 2014 offers a number of useful insights relevant to this study. Over 2500 hailstones were collected across 33 different hailstorms, photographed and subjected to a series of measurements (mass, compressive strength, major and minor diameters) [40]. For the sake of personnel safety, the measurements were carried out only after the storm had passed, thereby leading to some loss in diameter and mass. Under these circumstances, the maximum measured hailstone size corresponded to a

major diameter of 10.71cm. However there are also some extreme cases where hailstone sizes of up to 20cm has been reported in the United States [41].

SHAPE

The IBHS study also made an extensive catalog of the hailstones collected through an analysis of photographs and dimensional measurements. The study found that the majority of hailstones (84%) had a spheroidal shape (see figure 1.6b), while 10% were conical and the rest were irregularly shaped [40]. Another study investigating the behaviour of simulated spheroidal hail ice comparing it to simulated spherical hail ice noted that for any given velocity and mass combination the shape on average had minimal effect on the peak contact force imparted [42]. However in the case of natural hail ice the spheroidal shape is likely to increase the coefficient of drag which in turn results in a lower peak contact force (see sub-subsection 1.1.2.4).

From a practical standpoint, manufacturing spherical simulated hail ice is much simpler and standardised. For this reason researchers [5] have introduced the concept of an equivalent diameter based on data measured in the IBHS study. Figure 1.5 plots the measured mass on the y-axis and the measured maximum dimension on the x-axis.

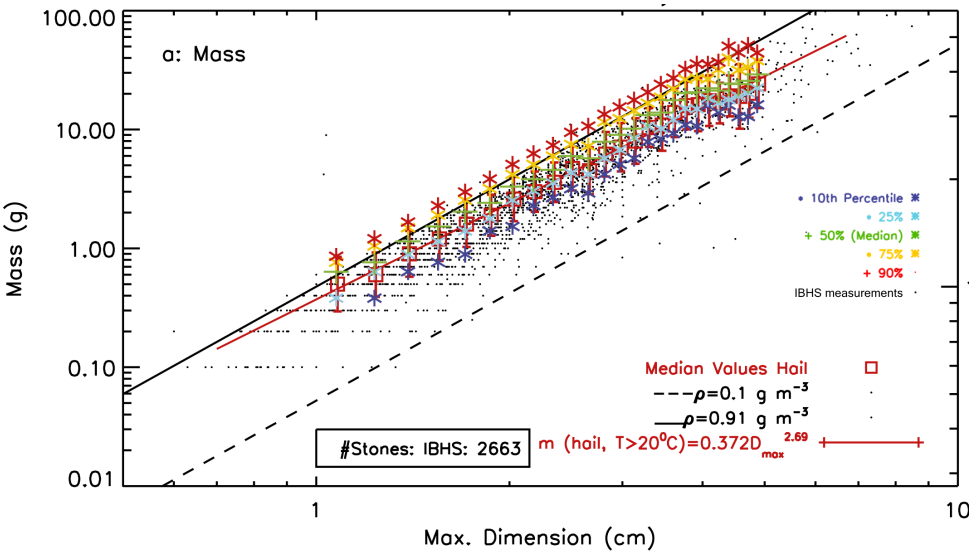

Figure 1.5: Plot of hail mass vs maximum dimension based on the IBHS study [5]

These measurements were averaged out into a best fit power law, resulting in the following relation between mass (m) and maximum dimension (D_{max}):

$$\begin{aligned} m &= 0.372(D_{max})^{2.69} \ [g] \\ m &= \rho_{ice} V_{eq} = \rho_{ice} \frac{1}{6} \pi {D_{eq}}^3 \ [g] \end{aligned} \tag{1.1}$$

$$D_{eq} = \left(\left(0.372 (D_{max})^{2.69}\right) \left(\frac{6}{\pi \rho_{ice}} \right) \right)^{\frac{1}{3}} \quad [cm] \tag{1.2}$$

where, ρ_{ice} is the density, V_{eq} is the volume, D_{eq} is the diameter respectively of the spherical simulated hail.

COMPOSITION

Figure 1.6a shows the cross-section of a large hailstone found after a hail storm in Aurora, Nebraska on 22nd June 2003. In this cross-section the layered nature of hailstones can be clearly observed. Researchers have classified this layered formation to two distinct growth phases called 'dry growth' and 'wet growth'. Dry growth corresponds to the opaque layer where numerous tiny air bubbles are trapped resulting in a spongy composition and the wet growth corresponds to translucent layers where the air bubbles are relatively low resulting in a composition similar to that of ice [6].

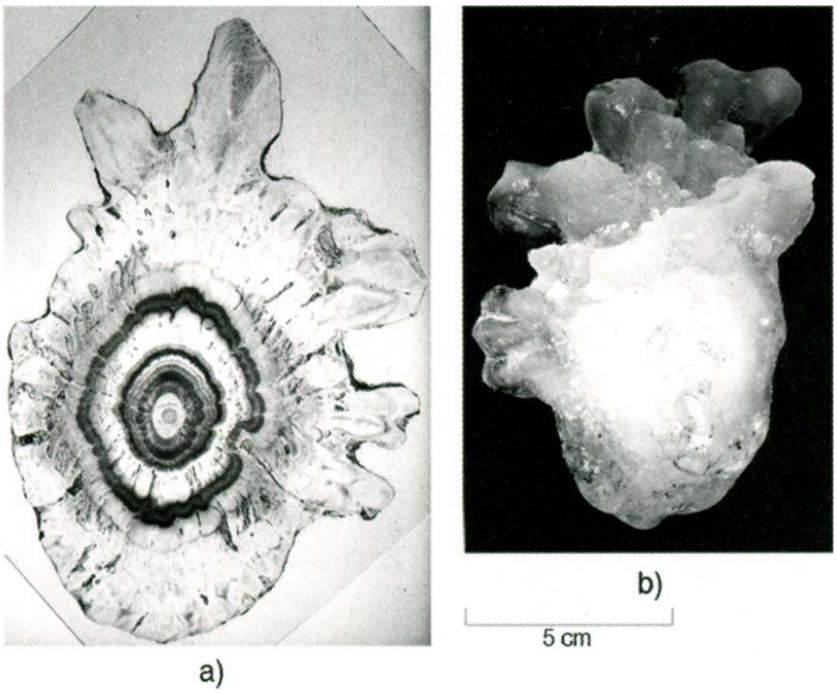

Figure 1.6: Hailstone from Aurora, Nebraska (2003)[6]

It is clear that this layered composition will have an influence on the density of hailstones. Figure 1.7 is a compilation of experimentally determined densities of natural hailstones that can be found in the EASA study [7]. Based on this and the density

bounds in figure 1.5 it may be stated that the density of solid ice ($917 kg/m^3$) may be considered an worst case estimate for natural hailstones. In figure 1.5 some data points may be found beyond either extreme of the density bounds. The authors attribute this to measurement uncertainities and water inclusions that may have drained upon impact [5].

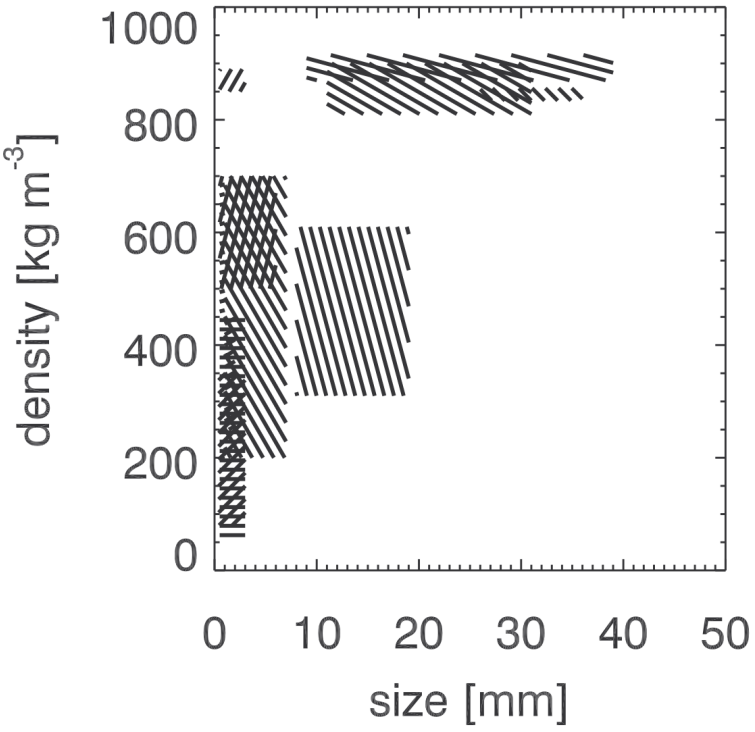

Figure 1.7: Compilation of natural hailstone density measurements[7]

The IBHS study also carried out measurements of the compressive strength of over 900 hailstones using a custom build apparatus [8]. This apparatus measured the peak compressive force up to which the hailstone stayed intact, and based on the measurements of major and minor diameters to determine the area, the results were post-processed to arrive at a value for compressive stress. Figure 1.8 is a plot of the obtained results juxtaposed with laboratory measurements of ice spheres (FM 4473).

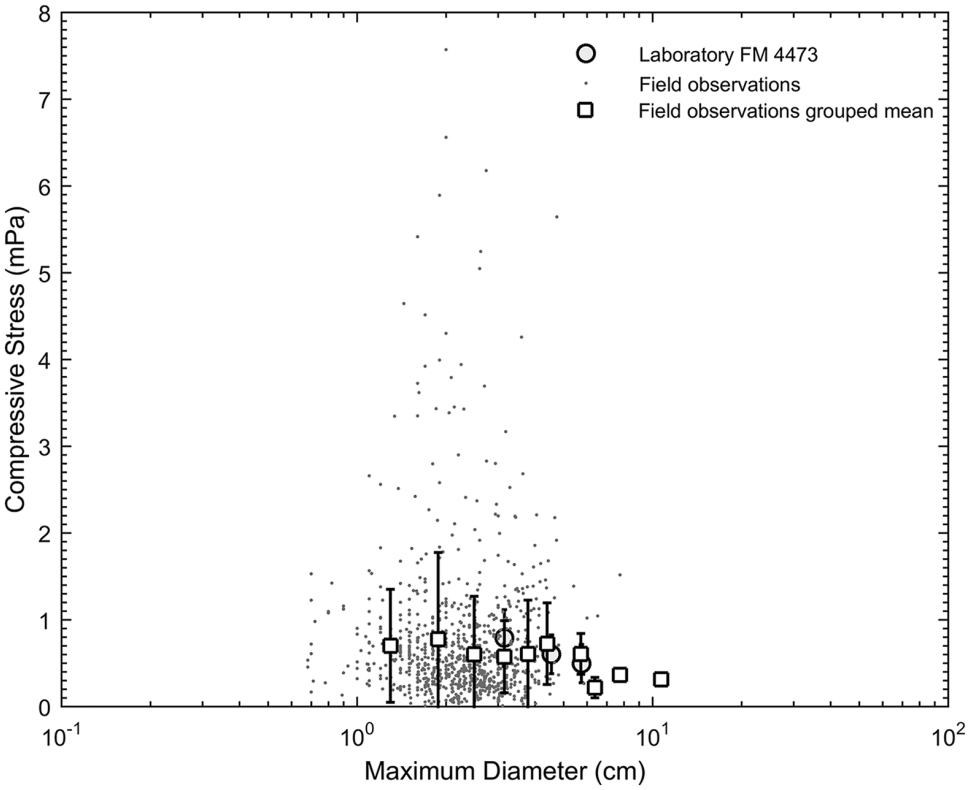

Figure 1.8: Results of Compressive Stress (MPa) from the IBHS study [8]

The results show that on average natural hailstones were stronger than the spherical ice spheres measured in the laboratory. This especially seems to be the case for hailstones below $5cm$ in maximum dimension. However it was noted that wide variability existed in the measured data that may be attributed to several factors such as impurities, inconsistent strain rate application and microstructure variations. Further in this study the sample size for hailstones beyond $4cm$ maximum dimension is limited. Figure 1.9 plots the frequency distribution of the available results against the ratio of the compressive strength of natural hailstones to the mean of ice spheres measured in the lab. These results indicate that while the ice spheres may be representative/ worst case for a majority of hailstones, this does not extend to all hailstones.

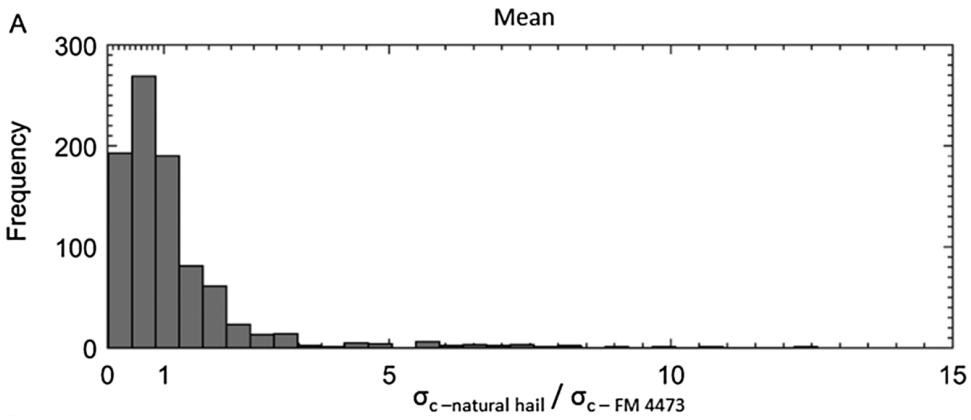

Figure 1.9: Frequency distribution of the normalised compressive strength [8]

VELOCITY

Velocity of a hailstone may be split into vertical and horizontal components [43]. The vertical component may be determined based on the balance between the gravitational force pulling the hailstone to the surface, and the drag force that is resisting the same. Velocity at which this balance is achieved is referred to as the terminal velocity. While the gravitational force is a consequence of the mass of the hailstone, the drag force is a consequence of the coefficient of drag which in turn depends on the shape, frontal surface area and the texture of the hailstone.

A comprehensive study was carried out based on the photographs, measurements and 3D scans of hailstones surveyed as part of the IBHS study [5]. Over 100 models of natural hailstones were created and 3D printed for a range of densities representative of natural hailstones. These plastic hailstones were levitated in a wind tunnel and this wind velocity was tagged as the terminal velocity of the hailstone under investigation. Based on this a relation was developed between the measured maximum dimension and coefficient of drag. These results were extrapolated upon in figure 1.10 for the larger sample of hailstones measured in the IBHS study. The blue line in figure 1.10 tagged 'Laurie' refers to the relation developed by an earlier researcher for a perfectly spherical hailstone based on equating its density to that of an ice sphere [44]. This terminal velocity (v_{ter}) may be expressed as follows:

$$v_{ter} = \left(\frac{4g\rho_{ice}D}{3C_d\rho_{air}}\right)^{\frac{1}{2}} \tag{1.3}$$

where, g is the acceleration due to gravity ($9.81 m/s^2$), ρ_{ice} is the density of ice ($917 kg/m^3$), D is the diameter of the ice sphere, C_d is the coefficient of drag (0.45) and ρ_{air} is the density of air ($1.2922 kg/m^3$) at freezing point.

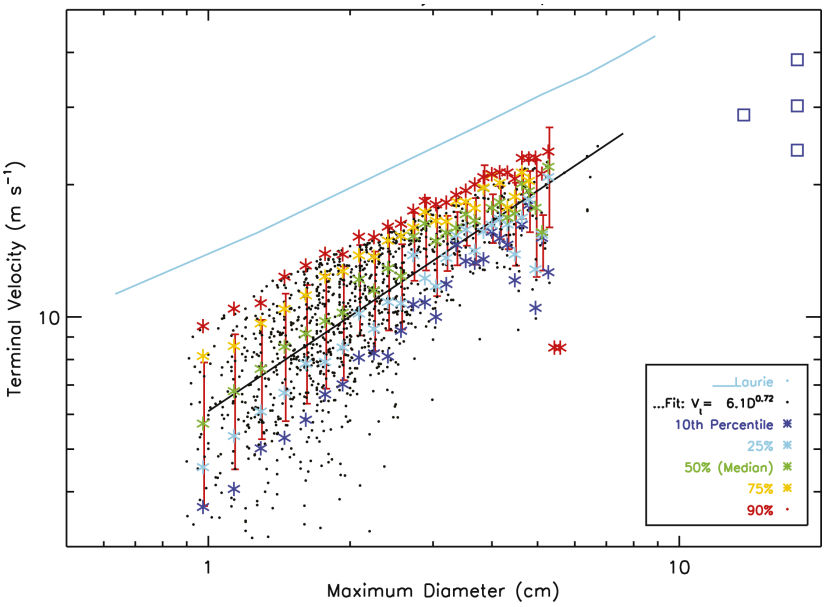

Figure 1.10: Relation between terminal velocity and maximum dimension [5]

Looking at figure 1.10, the Laurie curve appears to be an overestimate of the terminal velocity. Hence the researchers utilise the concept of equivalent diameter (equation 1.2) to arrive at figure 1.11 [5]. From this it is evident that the Laurie curve is an excellent worst case estimate once the equivalence relation is applied to arrive at spherical hail stone equivalent for natural hailstones. This conclusion is complimented well by another study that looked into the aerodynamics of lobed hailstones [45].

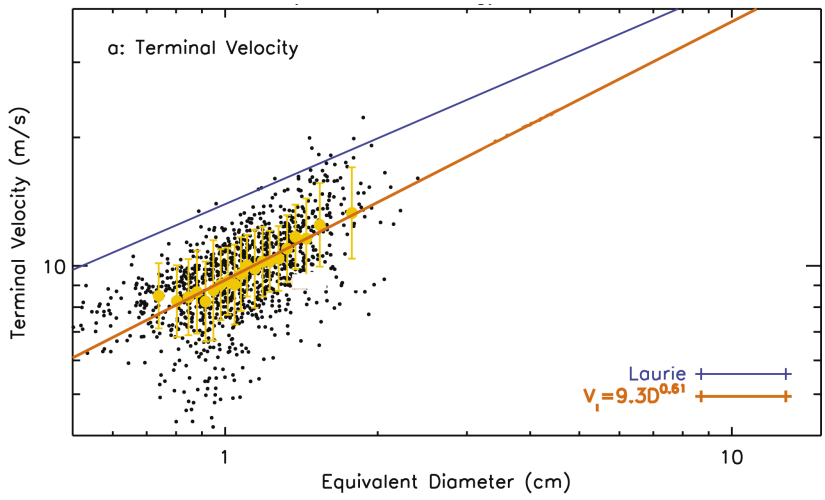

Figure 1.11: Relation between terminal velocity and equivalent diameter [5]

The horizontal component of the velocity is determined by the wind speeds prevailing at the time of impact. Wind is highly stochastic and hence there are several factors that complicate the determination of the same at any given point of time. Literature suggests that during a thunderstorm it can vary from $10 m/s$ in moderate cases to $35 m/s$ in some extreme cases [43, 46]. Experiments conducted on oblique impact of ice spheres on a horizontal surface indicates that the horizontal component of velocity has very little influence on the outcome [47, 48]. The impact can be estimated to be a lower velocity normal impact, implying that only the terminal velocity is the driving factor towards the peak impact force imparted on the horizontal surface. However, if the target is not horizontal such as a sloping roof or sections of an aircraft fuselage, then the horizontal velocity plays an important role.

INTENSITY

Modelling hail size distributions has been a subject of interest for decades with multiple researchers proposing different mathematical models to fit the obtained field data [49–51]. One of the earliest models proposed was an exponential law for modelling the size of raindrops [49] which was subsequently extended for hailstones [52]. This relation is given by:

$$N(D) = N_0 \exp(-\lambda D), \qquad 0.5cm \leq D \leq D_{max} \tag{1.4}$$

where, $N(D)(m^{-2}cm^{-1})$ is the number of hailstones within a diameter interval per unit of surface, $D(cm)$ is the diameter of the hailstone, $D_{max}(cm)$ is the maximum hailstone dimension, $\lambda(cm^{-1})$ is the slope and $N_0(m^{-2}cm^{-1})$ is the intercept on the axis.

A recent study used data obtained from hailpad networks setup across southern France, Spain and Argentina and attempted to fit this exponential model to it using the least squares method [9]. The results reveal that the data available is nearly exponential, though some variations exist from region to region. Based on this for the purposes of this study, this model is considered an adequate representation of hail intensity.

Figure 1.12 has been plotted using a visual estimate of the raw data from this study as original data was not made available. This particular plot pertains to the data acquired from the hailpad network in the Inland Area of France (1987-2005) obtained after analysing over 7 million impacts across almost 2500 hailpads. The N_0 and λ values have been used as is from this study. Note that the purpose of this plot is to demonstrate the exponential trend, and not for a one to one match between the raw data and best fit line.

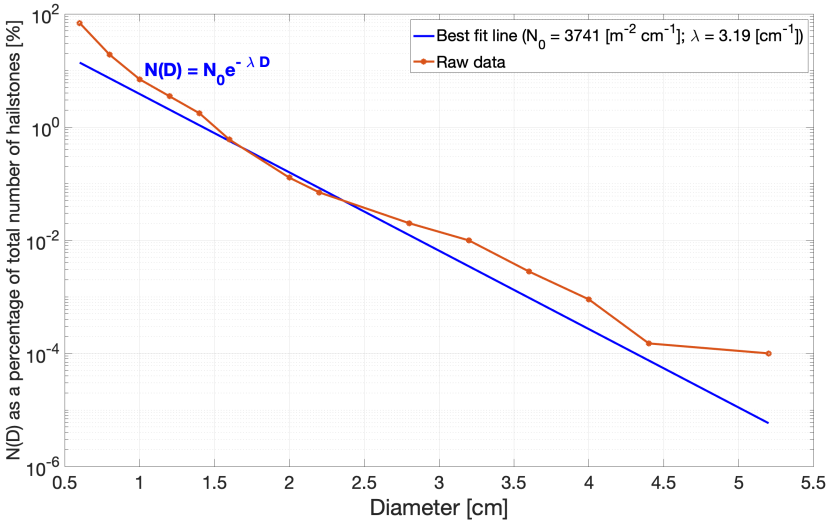

Figure 1.12: Comparison of exponential hail intensity model to raw data collected from hailpads in the Inland Area of France (1987-2005) [9]

It is however noteworthy that recently researchers have developed a model which extends this further by introducing a probability distribution based on previously collected data [53]. This model for any given maximum hailstone diameter and the area of the impacted surface, is able to make predictions of the diameter of the other hailstones that may impact the surface.

1.1.3. SYNOPSIS

Lack of specifics in the current regulatory framework leaves space for interpretation on the level of risk posed by hail ice to aircrafts while on the ground. The different parameters chosen by Boeing and Airbus to test simulated hailstone impacts on CFRP structures is evidence of this. Based on both past incidents and the intersection of airport locations with hail prone areas it is reasonable to state that aircraft ground hail encounter deserves a closer look. While instances of $20cm$ maximum dimension hailstones have been reported, it would not economically feasible to design aircrafts for once in a blue moon events. For the purposes of this study a maximum dimension range of $0.5cm$ to $15cm$ is chosen. Given perfectly spherical ice is representative of a larger natural hailstone, using equation 1.2 this is estimated to equivalent diameters ranging between $0.49cm$ to $10.41cm$. While the density of solid ice ($917kg/m^3$) may be considered representative of a worst case natural hailstone, there is ambiguity on the ability of simulated spherical hailstone to be representative of the compressive strength of natural hailstones.

Based on equation 1.3 the terminal velocities for these equivalent spheres may be determined. The velocity values for the entire range is plotted in figure 1.13. Given the

uncertainty with respect to the horizontal velocity component, figure 1.13 also has the resultant velocity curves under the presence of 10, 25 & 35m/s winds. These resultants are derived with the assumption that the impacted surface is at a 45° angle from the horizontal.

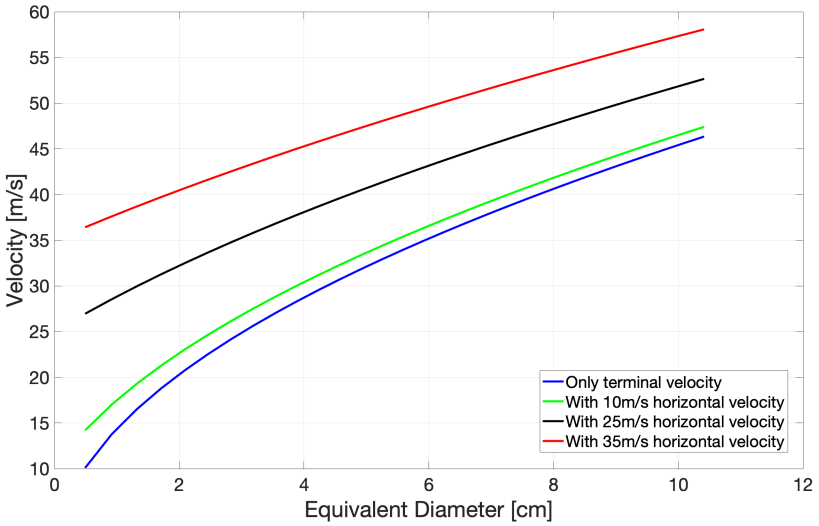

Figure 1.13: Resultant Velocity [m/s] vs Equivalent Diameter [cm]

Based on these velocity values and equation 1.1, the KE ($\frac{1}{2}mv^2$) is derived in figure 1.14 defining the full scope of the problem statement to be tackled in this study.

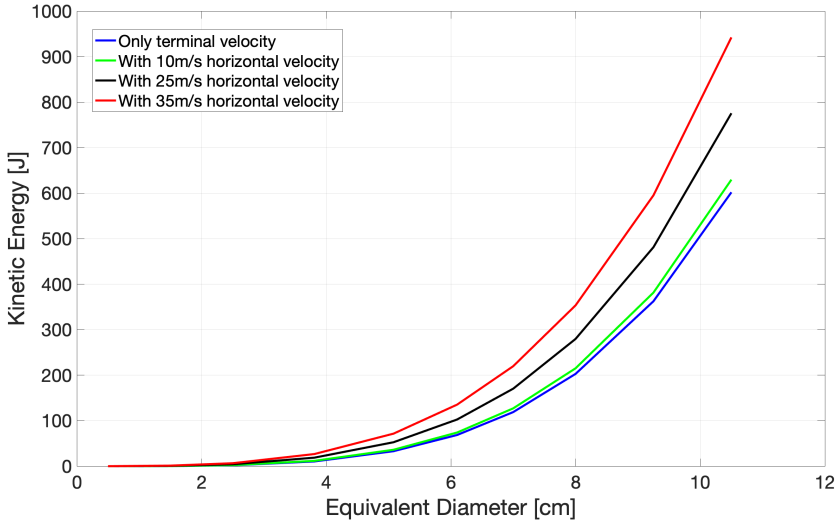

Figure 1.14: Kinetic Energy [J] vs Equivalent Diameter [cm]

1

1.2. SIMULATED HAIL ICE

1.2.1. EXPERIMENTS

This subsection presents the currently available test standards involving Simulated Hail Ice (SHI) and experiments carried out by researchers in this field. Some experimentally determined ice mechanical properties of relevance are looked into as well.

TEST STANDARDS

There are currently no test standards available for testing CFRP structures with SHI. There is only one standard available in the aerospace context from American Society for Testing and Materials (ASTM) which prescribes standard testing procedure for hail impact resistance of aerospace transparent enclosures (windshields) [54]. From the context of testing the impact resistance of roofing materials from hail ice, one standard is available from American National Standards Institute (ANSI) [55]. Two other standards are available from ASTM that are intended for the determination of the hail impact resistance of solar collector covers and photovoltaic modules [56, 57]. There are a number of similarities and interesting deviations in each of these standards which may be of relevance to this study.

The common threads include the requirement of a mould for freezing the SHI, a launcher capable of accurately firing the SHI at the prescribed velocity, a sabot for carrying the SHI sphere, a method for determining SHI integrity, a method for verifying if the mass and size are within the margin of error, a method for measuring the speed of the SHI and safety precautions. Some additional standards pertaining to the aerospace application ASTM test include the introduction of a cotton ball in the SHI mould to increase the strength and the prescription of specific SHI sizes and velocities ($60 - 600 m/s$). While this may adequately represent a mid flight hail impact on the aircraft windshield, researchers have found that SHI prepared in this fashion is significantly more lethal to CFRP panels and are not an accurate representation of natural hailstones [58]. Moreover the minimum velocity tested is higher than the maximum velocity identified in section 1.1.3.

The ANSI standard prescribes some nominal diameters for SHI and their nominal mass. It further prescribes the KE range to be tested, computed using the terminal velocity for each size and mass combination. A 60 second limit is also prescribed for the time allowed between the SHI being taken out of the freezer and the test being carried out [55]. The other two standards from ASTM do not prescribe any nominal sizes for the SHI but instead asks the user to refer to local historical weather records. A 60 second time limit for testing is prescribed in these standards as well. One relevant addition seen in these standards is the consideration of hail accompanied by wind. A $20 m/s$ horizontal velocity is prescribed to be included through vector addition to the terminal velocities of the chosen SHI sizes [56, 57].

EXPERIMENTS BY RESEARCHERS

One of the earliest experiments involving SHI and CFRP materials was carried out to investigate the effect of hail impact on fatigue life [59]. This study was quite limited

given only two SHI sizes (2.53 & 3.81cm) were tested. These test were carried out using an impact gun at a velocity that was the resultant of the terminal velocity and a 36.6m/s horizontal velocity. Another early literature is from a research group based out of the University of California, which has subsequently made multiple contributions towards this subject [60]. The first study is an investigation of high velocity SHI impact on exposed CFRP structures. The experimental setup used involves an impact gun to launch the projectiles, a Force Measurement Transducer (FMT) and CFRP panels. The FMT was made using a dynamic force transducer, sandwiching it between a titanium plate and a steel support. SHI was manufactured by pouring distilled water into a mould and subsequently freezing it. This set up is replicated by multiple researchers. An overview of the size, velocity and significant outcomes are listed in table 1.1 chronologically for parameters within or near the range of interest (section 1.1.3).

Table 1.1: Overview of research carried out with SHI (If both the velocity and size are within the range of interest for this study, the cells are highlighted green)

Diameter (cm)	**Velocity** (m/s)	**Comments**	**Year**	**Reference**
2.53, 3.81	43, 45.9	No damages observed on 16 ply thick quasi-isotropic laminate	1998	[59]
2.54, 4.27, 5.08	30-200	Failure Threshold Energy (FTE) was identified corresponding to KE at damage initiation for quasi-isotropic laminates of thickness 1.22 – 2.62mm; Impact by smaller sphere more severe than larger sphere of equivalent KE; Time lag exists between peak force & peak panel displacement	2000	[60]
2.54, 4.27, 5.08	30-200	Same setup as previous; Woven CFRP panels used as a target & FTE was identified; Flat wise layered ice tested but no major difference was identified when compared to monolithic ice; 4 min time interval from freezer to firing; Linear trend identified between KE and peak contact force	2003	[48]
3.4, 4.8	100-152	Similar test setup as above but no FMT measurements; 5.4mm thick quasi-isotropic laminates tested	2009	[61]
5.08	50-120	FTE was determined for a CFRP bonded single lap joint & was found to be much lower than a panel with no joints	2010	[62]

Diameter (cm)	Velocity (m/s)	Comments	Year	Reference
4	45	Compressed snow was used to make SHI; Pressure sensitive film was used to carry out measurements; Impact zone observed on pressure sensitive film was much smaller than the diameter of the projectile	2011	[63]
1.29, 2.75, 3.74, 4.2	1.5-2.75	Drop weight technique used to impact ice sphere on target surface; critical velocity (defined as the velocity above which ice sphere impacts will lead to alterations such as cracking) is estimated	2012	[64]
3.81, 5.08, 6.10	25-290	FTE evaluation for CFRP panel (thickness $1.59-4.66mm$) manufactured using tape laying; Data closely matches study on woven CFRP panels [48]; Relation proposed to plot FTE as a function of velocity of SHI projectile, thickness of target panel and diameter of SHI projectile	2012	[65]
3.4, 4.8	117	Experiment carried out on non-crimp fabrics, 2D plain weave & 3D weave CFRP laminates (thickness $4mm$); Delaminations in woven laminates start to appear at a lower velocity as compared to non crimp fabrics	2012	[66]
3, 4, 5	50-250	Contact force measurements were carried out; Relation proposed between delamination area & a non dimensional variable derived from the KE, frontal area & laminate thickness	2015	[67, 68]
5, 5.75, 6.35	28.4, 30.5, 32	Closest match to parameters identified in section 1.1.3; Setup and results are discussed in detail below (1.2.1.2)	2015	[10]
5	70	A pressure Hopkinson aluminium bar based sensor is used for measuring force-time history	2018	[69]
2.5	60.6-190	Cross ply CFRP laminates of thickness $1mm$ were tested	2018	[12]
3.5	150-200	Aluminium/CFRP dual plate was impacted with SHI; Internal/external damage evolution was identified	2020	[70]

One major draw back of the experiments listed in table 1.1 is that they are discrete results that are not easily compared with each other nor easily extendable over the range of SHI size and velocity parameters relevant to this study. Another drawback is that in order to prevent damage, measurement sensors such as FMTs and strain gauges are shielded by a metallic plate or the CFRP panel being impacted. This shielding introduces a fictitious force that effectively reduces the severity of the peak force in measurements. Some researchers have sought to solve this by exposing the sensors directly to impacts, risking damage, such as in the case of using a pressure Hopkinson aluminium bar sensor [69].

However one study stands out as a notable exception to these drawbacks [10]. SHI of sizes that fall within the parameters of interest for this study have been tested at their terminal velocities with the aim of realising a peak contact force prediction model. An apparatus was designed and custom built by the authors to carry out the peak force measurement. This apparatus comprises of one impactor facing lumped mass, one immobile lumped mass and a spring connecting the two masses. The impactor lumped mass was fitted with an accelerometer (a_2) and a high speed camera was used to track the displacement of the spring (x_2). The contact force would equal the sum of the inertia force of the impactor lumped mass and the reaction force of the spring as per the principle of dynamic equilibrium. Hence, as long as the mass of the impactor facing lumped mass (m_2) and stiffness of the spring (k_2) is known, the impact force can be easily evaluated using the sensor measurements (a_2 & x_2). Figure 1.15 is a representative model of the setup.

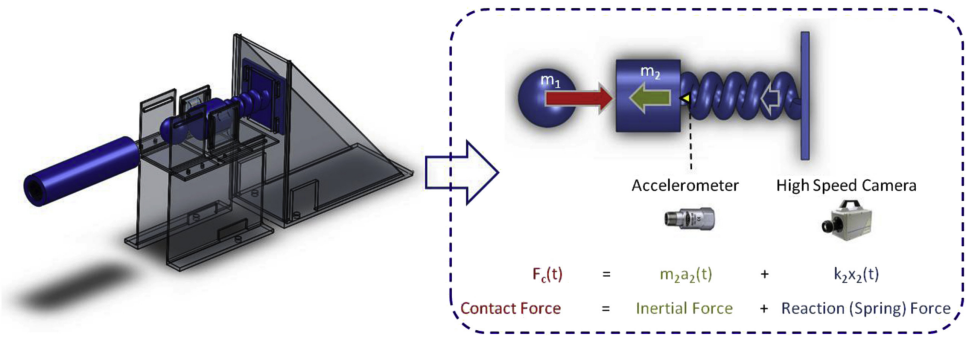

Figure 1.15: Peak contact force measurement apparatus [10]

Further the impact scenario has been modelled as a 2DOF mass-spring-damper system. A parametric study was carried out to determine the non-linear contact stiffness parameters used to model the mass-spring-damper system to find the best fit for the experimentally determined target displacement time history. Based on this the following algebraic expression is derived for analytically estimating the contact force (F_c):

$$F_c = k_n \left[1 + (0.2p + 1.3)\left(\frac{1 - COR}{COR}\right)\left(\frac{-b + \sqrt{b^2 + 4c}}{2}\right)\right] \times \left(\frac{p+1}{2k_n} m_1 v_0^2 COR\right)^{\frac{p}{p+1}} \left[1 - \left(\frac{-b + \sqrt{b^2 + 4c}}{2}\right)^2\right]^{\frac{p}{2}} \tag{1.5}$$

$$b = \frac{p \times COR}{(p+2)(0.2p + 1.3)(1 - COR)^2}$$
$$c = \frac{2}{p+2} \tag{1.6}$$

where, k_n = non-linear stiffness coefficient, p = exponent characterising spring behaviour, COR = Coefficient of Restitution, m_1 = Mass of the Impactor and v_0 = Impact Velocity.

Once the parameters are calibrated correctly, this equation has the ability to predict a range of contact force values for impactors of different mass and velocity combinations. This provides some degree of flexibility during tests as it isn't possible to get an exact value for impact velocity with the impact gun. To demonstrate this, the researchers have put together a design chart that estimates the peak contact forces for a range of SHI sizes and velocities. This chart has be reproduced as figure 1.16.

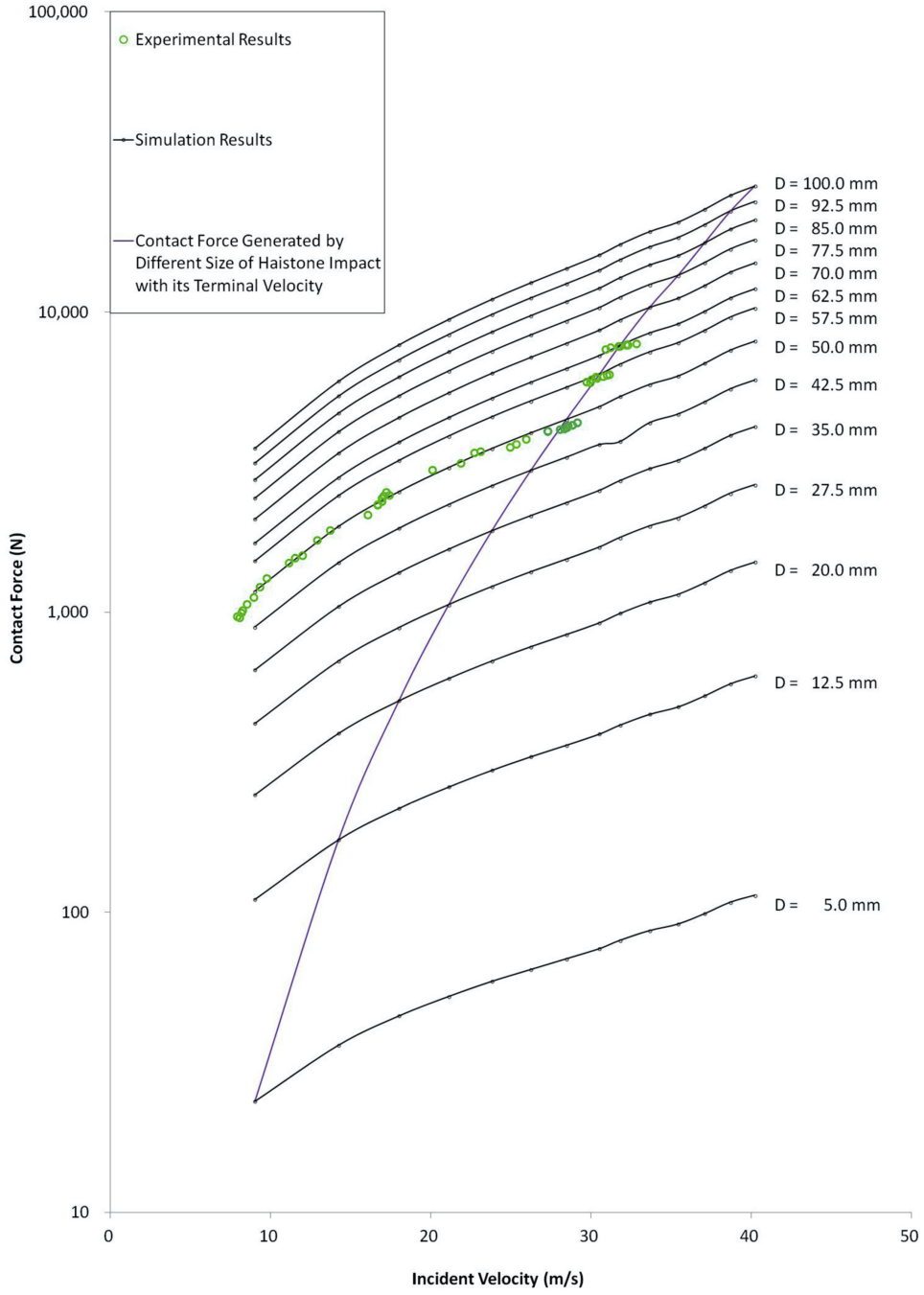

Figure 1.16: Design chart with estimates of peak contact force generated by SHI of varying sizes and velocities [10]

Though this may be a deviation from the experimental methodology discussed so far, it is noted that one study has attempted to replace the steel impactor head with an impactor head made of ice in a typical drop tower apparatus. However the accuracy of the results obtained were affected by inconsistencies in the behaviour of ice impactor heads leaving it unclear if any equivalence can be drawn to hail stone impacts [71]. Hence for the purposes of this study, firing SHI projectiles using an impact gun is deemed the state-of-the-art for replicating hail impacts.

MECHANICAL PROPERTIES

A 2003 review of the mechanical properties of ice provides an excellent overview and identifies parameters that can affect them [72]. The Young's Modulus was found to be in the range of $9.7 - 11.2GPa$ and the Poisson's ratio in the range of $0.29 - 0.32$ at a temperature of $-10°C$. The tensile strength was found to vary between $0.7 - 3.1MPa$ but showed no sensitivity to either temperature or strain rates. However the compressive strength showed wide variability with changing temperature and strain rates. Parameters such as grain size and volume may also play a role in determining the tensile and compressive strength. While the effect of grain size can be minimised with standardised ice manufacturing and impact testing procedures, a drop in compressive strength is to be expected with increasing volume due to the presence of more defects in the microstructure.

Early research suggested that as strain rates were increased, a distinct transition point existed at which the compressive strength peaked and brittle mode took dominance over a ductile mode of failure [73]. This transition point was identified to be around a strain rate of $10^2 s^{-1}$. However subsequent research carried out on the subject have disproved this theory and the compressive strength was found to increase as strain rates were increased [74, 75]. Figure 1.17 reproduces a plot compiling all of these results as found in another study [11].

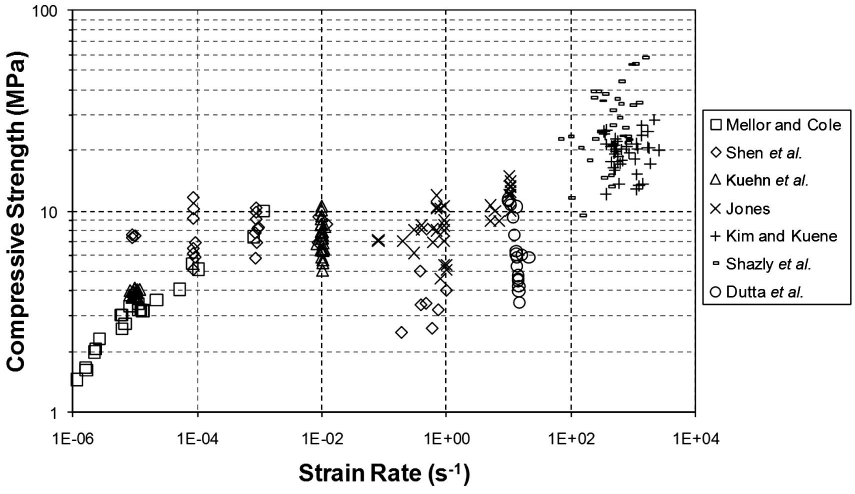

Figure 1.17: Compressive Strength vs Strain Rates [11]

The experiments carried out for strain rates near $10^3(s^{-1})$ is said to correspond to the strain rates expected in an impact scenario, though it is unclear to what extent this is applicable to impact velocities lower than $30m/s$. For modelling impacts, knowing the precise compressive strength is critical as compressive failure is the dominant mode. Decrease in the temperature from $0°C$ to $-40°C$ was found to cause a 4 fold increase in compressive strength [72]. This can be demonstrated from the data in figure 1.17, where experiments tagged 'Kim and Kuene' were carried out at $0°C$ [74] and the experiments tagged 'Shazly et al' were carried out between $-10°C$ and $-30°C$[75]. The increased compressive strength is evident in the later case. However it is to be noted that temperatures below $-10°C$ aren't of much consequence to this study since the focus is on ground hail impact events.

1.2.2. NUMERICAL MODELLING

It is common practice in engineering to utilise commercial finite element software suites for carrying out simulations with the aim to improve the reliability of the design and reduction of the costs. A numerical model that has the ability to accurately capture the hail impact phenomenon would be hugely beneficial, given the requirement of expensive equipment and the complexities with handling SHI for experimental testing. Naturally this has been a subject of interest for researchers, and two decades ago the first such model was proposed [60]. This utilised a fairly basic elastic-plastic material model with failure and attempted to tune it to the limited experimental results available at the time on SHI impacts. From here on various incremental updates have been made to this model over the years and an overview of the same can be found in table 1.2. Note abbreviation Smoothed Particle Hydrodynamics (SPH).

Table 1.2: Overview of numerical modelling of SHI;
Models within the parameters relevant to this study are highlighted in green

Software	Impactor Mesh	Velocity (m/s)	Comments	Year	Reference
DYNA3D	Lagrangian	> 70	Simple elastic-plastic model with failure; Tuned to match experimental results;	2000	[60]
LS-DYNA	Eulerian	> 90	Introduction of strain rate dependent failure parameters;	2006	[76]
LS-DYNA	SPH	> 70	Same as previous [60]; SPH introduced; Tuned to match experimental results	2009	[61]
LS-DYNA	SPH	45	Same as previous [60]; Tuned to match experimental results	2011	[63]
LS-DYNA	SPH	> 100	Same as previous [61]; Tuned to match experimental results	2012	[66]
ABAQUS	Lagrangian	> 60	Strain rate sensitive material model for spherical ice impact; See (1.2.2)	2013	[11]

Software	Impactor Mesh	Velocity (m/s)	Comments	Year	Reference
ABAQUS	SPH	> 70	Same as previous [11]; SPH introduced; See (1.2.2)	2018	[69]
LS-DYNA	Lagrangian	> 50	Modelled using the Druker-Prager yield function; Tuned to match numerical results [76]	2018	[77]
ABAQUS	Lagrangian	> 60	Improvement on existing model [11]; See (1.2.2)	2019	[12]
LS-DYNA	SPH	< 46	Same as previous [76]; SPH introduced;See 1.2.2	2019	[13]

One of the key ingredients to capturing the behaviour of ice in a numerical model is to ensure that mechanical properties (See section 1.2.1.3) such as the strain rate dependence of the compressive strength are accounted for. Two numerical models that have accounted for this form the basis on which the state-of-the-art rests on [11, 76]. These will be referred to as the Tippmann model and the Carney model going forward. A key benefit offered by both models is the elimination of the need to manually tweak the material input parameter based on experimental results, thereby offering an element of universality to them. The Tippmann model was specifically developed for modelling spherical ice projectiles and the peak contact forces generated by them in the early stages of impact. The dynamic force history measurements showed good agreement with previously executed experimental work on SHI [60].

Another study makes iterative improvements on the Tippmann model by introducing mesh-free (SPH) methods to model the impactor [69]. This method was already employed to model bird strike scenarios and demonstrates the ability to handle high strain levels better than traditional methods while also improving the processing speed. This model showed good agreement when juxtaposed with both the Tippmann model and experimental data independently gathered. However when looked at purely from the perspective of computational efficiency, one model stands out [12]. This model is a derivative of the Tippmann model and manages to cut down the size of the dynamic system by over 98% with acceptable levels of deviations from the baseline for velocities over $100 m/s$. This level of efficiency is achieved by the introduction of a visco-plastic contact law and Time Domain Spectral Finite Element (TDSFE) with explicit time integration and geometric nonlinearity. Figure 1.18 plots the same, juxtaposed with the numerical results of the Tippmann model and its experimental validation.

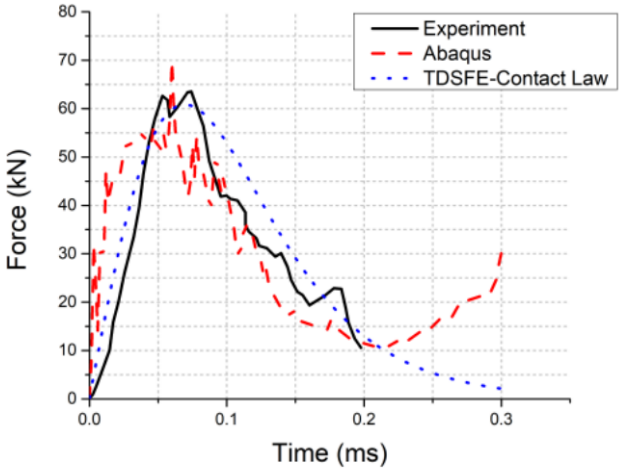

Figure 1.18: Force-time history for SHI with diameter 5.08cm and velocity 144.1m/s [12]

Only one study so far has looked into modelling SHI in the velocity regime that falls within the parameters of interest for this study [13]. This study was carried out in the context of investigating hail impact damage on metallic roof panels. This is done by carrying out a set of finite element simulations developed as an iteration on the Carney model. For reasons previously discussed, SPH is introduced as well. This model is first verified against the results obtained by the Carney model and subsequently setup for the velocity regime of free falling hailstones. The SHI sizes considered here are 5.08, 7.62 and 10.16cm. The force-time histories so obtained were compared with previous experimental results [10] and found to be within a margin of 15%. Figure 1.19 is a screen grab from the validation process.

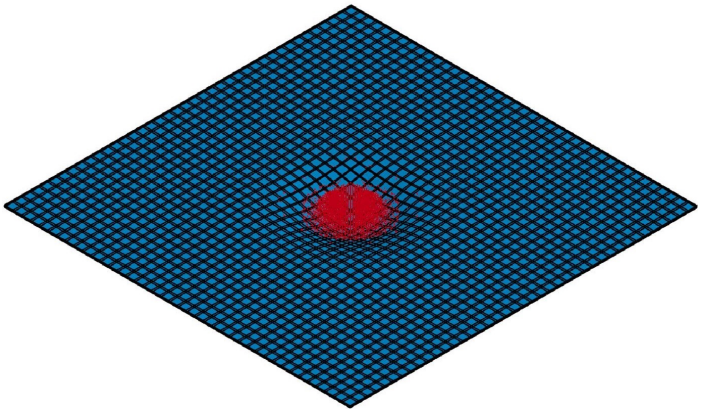

Figure 1.19: Screen grab from the validation process [13]

The researchers then go on to model a metallic roof panel and carry out multiple simulations to investigate the effect of SHI impact. Multiple hail impact simulations (Diameter $> 5cm$) are also carried out consecutively on the same location, though no detailed phenomenological reasoning is offered for it. Significant finding of this simulation is the ability for an existing large diameter hail impact damage to be exacerbated by otherwise not so significant impacts.

It is noted here that a number of studies are also to be found that model both the CFRP panels and the SHI impact damage evolution competently [78, 79]. However these are at the moment outside the scope of this study.

1.2.3. SYNOPSIS

No test standard has been established so far for testing SHI impact on CFRP structures, however useful insights on best practices may be found in standards developed with a different use case in mind. Early experimental research indicates that there was no damage to be found in CFRP panels after impact testing with SHI within sizes and velocities identified in synopsis 1.1.3. This is however contrary to the numerous reports of aircrafts being damage by ground hail incidents identified in the previous section [20–24].

Given the lack of standardised test practices, the experiments looked at in preceding sections do not readily compare with each other in terms of measured values such as peak contact force. Hence in figure 1.20 a compilation of the mass and velocity combinations tested can be found, juxtaposed with the range that is within the parameters established in section 1.1.3. A number of them are outside the parameters of interest for this study, but however may prove useful as they form the foundation for the state-of-the-art numerical models. One study [48] investigated flat wise layered ice and deemed the variations introduced in compressive strength to be insignificant. Subsequent researchers [10] cite this result and draw an equivalence to the layered composition of natural hailstone being insignificant as well. This is in contradiction to the finding in synopsis 1.1.3.

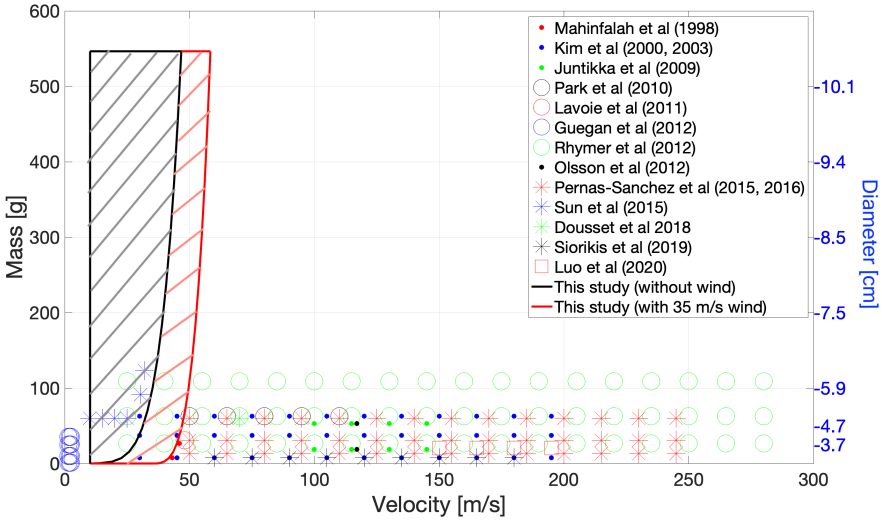

Figure 1.20: Compilation of the mass and velocity combinations of SHI found in literature

The lack of standardised test practices would also imply that any numerical model developed would require experimental validation to carry scientific weight. The custom built spring-lumped mass apparatus offers a number of unique advantages both in terms of experimental flexibility and extrapolation capabilities. Replicating this may be considered for carrying out experimental measurements with SHI. The impact gun is also ascertained to be the leading methodology for SHI impact tests.

Both temperature and strain rates are critical factors that determine the compressive strength of ice. It would therefore be wise to minimise the time the SHI stays outside the freezer prior to impact and standardise this time for all tests. Numerical models have found to show good correlation to experimental results, when strain rate sensitive material models are used. Given the specificity with which the Tippmann model was developed and the ability to speed up simulations [12] to find estimates for a broad set of parameters quickly, this is chosen as leading for all proposed numerical models. Additionally the use of SPH mesh free methods is proposed for modelling the impactor if higher precision is required for a specific set of results. Carney model may be utilised for verification if the need arises. This overview so far also makes it clear that these numerical models have been validated only with a couple of experimental tests. The results are also depended on the mesh sizes which may introduce variations of their own.

2

Research Questions

How do the characteristics of hail ice influence the severity of impact?

- What would be a reasonable estimate of kinetic energy of the hailstone prior to impact?
  A: *This study has determined that the kinetic energy can vary from* $0.003J$ *to over* $900J$ *depending on the size of the hailstone and the prevailing winds.*
- Given the brittle nature of ice and low velocity at impact, peak force at the point of impact might be a better measure of severity than the kinetic energy. What levels of peak force is hail ice capable of generating?
- Can an ice sphere be deemed a reasonable worst case estimate to naturally occurring hail ice?
  A: *Based on this study yes, but questions over the compressive strength and the consequent impact force remain.*
- Wide variability in compressive strength of ice spheres has been previously documented. Is there a way to make the properties more consistent?

3

Development of Numerical Model

As laid out in the literature study (synopsis 1.2.3), given the specificity with which the Tippmann model [11] was developed it was deemed most suitable for arriving at peak impact force estimates for a broad set of parameters identified in section 1.1.3. This chapter explains the setup and implementation of this model in the ABAQUS 2019 finite element analysis software on the High Performance Computing (HPC) cluster of the Faculty of Aerospace Engineering, TU Delft.

3.1. Baseline Model Setup

A quarter symmetric model of the SHI and rigid target plate was created as shown in figure 3.1, with the goal of minimising the computation time. For the first model, the SHI had a diameter of 50.8 mm to aid in easy comparison with previously published results. The rigid target plate has a surface dimension of 50 mm by 50 mm and a thickness of 1 mm. A hard and frictionless contact interaction was setup between these parts. Appropriate symmetric boundary conditions were applied in addition to fixing the displacements and rotations for the rigid target plate. A predefined velocity loading of 60.6 m/s was applied to the SHI in line with the reference literature. The rigid target plate is defined as a rigid body in ABAQUS so as to extract the maximum force that SHI can potentially impart on a body.

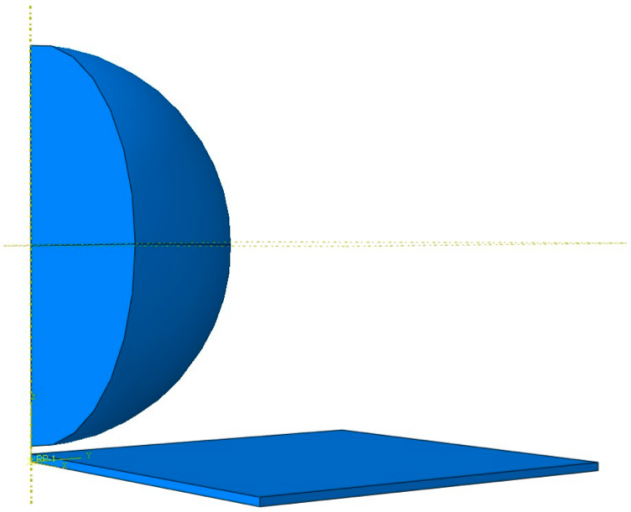

Figure 3.1: Quarter symmetric model of SHI impactor and target plate

The material properties used to define ice are drawn from section 1.2.1.3 and the ones used in the Tippmann model [11]. A summary of these properties can be found in table 3.1.

Table 3.1: Summary of material property definition for ice

Property	**Value**
Young's modulus	9380 MPa
Poisson's ratio	0.33
Density	917 kg/mm^3
Tensile failure pressure	0.517 MPa
Quasi-static yield strength	5.2 MPa
Rate dependent yeild strength	See appendix A.1
Linear bulk viscosity coefficient	1.2
Quadratic bulk viscosity coefficient	0

For this baseline model a very fine mesh, with a global element size of 0.381 mm was chosen for the SHI impactor to enable easy comparison of functionality to existing literature. Element type used here is an eight-node reduced integration hexahedral linear brick element. The rigid target plate uses the same element type, though with a much larger size and one element thick along the thickness direction. Subsequently a dynamic explicit analysis is carried out on the HPC cluster. Further details regarding the model setup and input parameters can be found in appendix A.2.

3.2. BASELINE VERIFICATION & VALIDATION

The force-time history of the SHI impact was taken to be the key result to be verified and validated. Specifically the reaction force on the rigid target plate along the velocity vector is tracked for this purpose.

3.2.1. ANTI-ALIASING: BUTTERWORTH FILTER

Upon progressively increasing the field output sampling parameter, it was evident that a high sampling rate and an effective low pass filter are essential to extract a meaningful data from this analysis. After a quick survey of the possible low pass filter approximations, a second order Butterworth Filter was deemed to be a good option given flat pass band and reasonably steep roll-off between the pass band and stop band frequencies. The cutoff frequency was set to around 123 kHz, more than sufficient to capture the peak of the reaction force. This data filtering was carried out in MATLAB with zero phase delay after extracting the readout from ABAQUS since operating the front end on the HPC cluster using X forwarding was a rather cumbersome process.

The results so obtained are plotted in figure 3.2 and contrasted with the experimental and numerical simulation results obtained by Tippmann [11]. These results are deemed to be a satisfactory reproduction of previously documented literature based on the similarity of the obtained peak force magnitude and time.

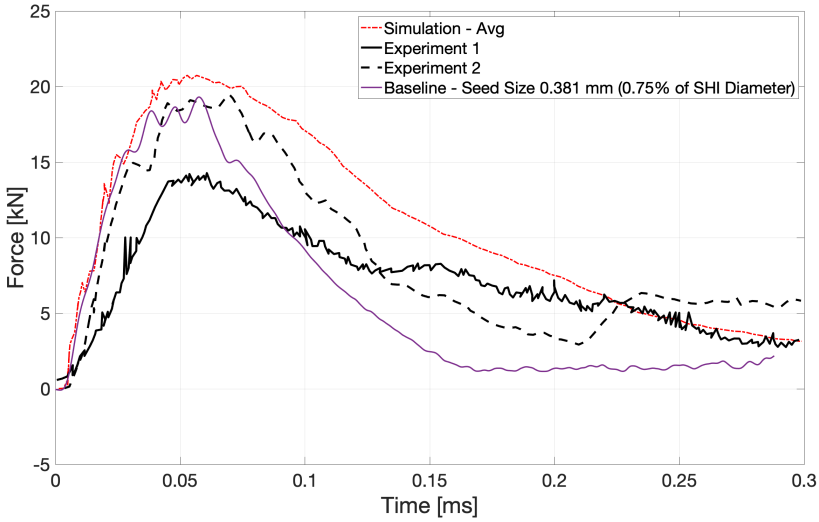

Figure 3.2: Baseline verification against experiments and numerical simulation carried out but Tippmann et al [11]

3.2.2. MESH CONVERGENCE STUDY

With the functionality of the methodology verified in the previous step, a mesh convergence study was performed with the aim of confirming the validity of the obtained

results and to possibly optimising the solve time. The mesh configurations used for this study range from a global seed size of 5.08 mm (10% of SHI diameter) to 0.254 mm (0.5% of SHI diameter). In addition to this several hybrid mesh combinations were tried out. A 50%-50% mesh having global element sizes at a 1.5%-1% size ratio to the SHI diameter with the smaller elements populating the quadrant encountering the impact first showed the most promise. This meshing scheme is shown in figure 3.3. The results of this convergence study can be seen in figures 3.4 and 3.5.

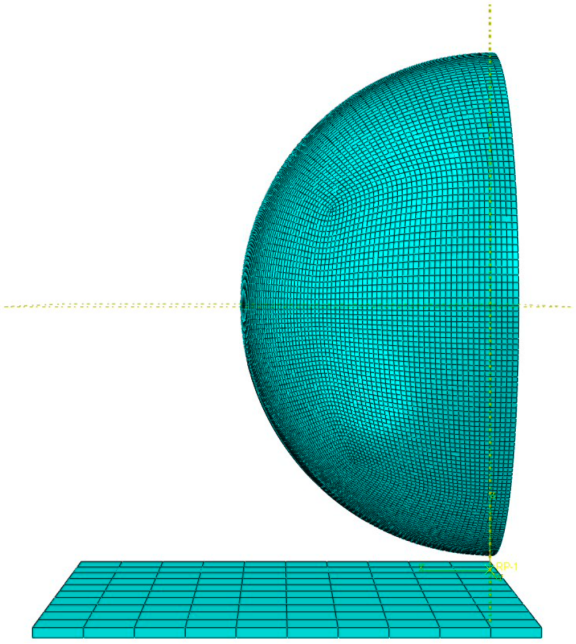

Figure 3.3: Baseline model with hybrid mesh

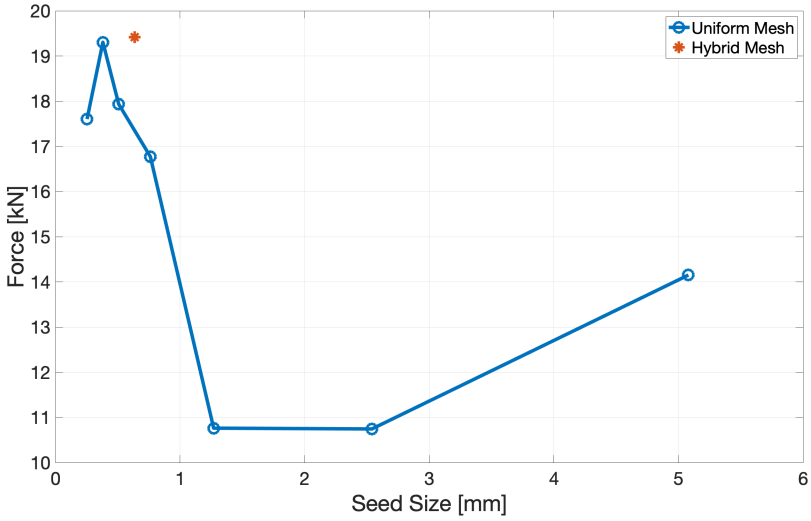

Figure 3.4: Mesh Convergence Analysis: Peak Force

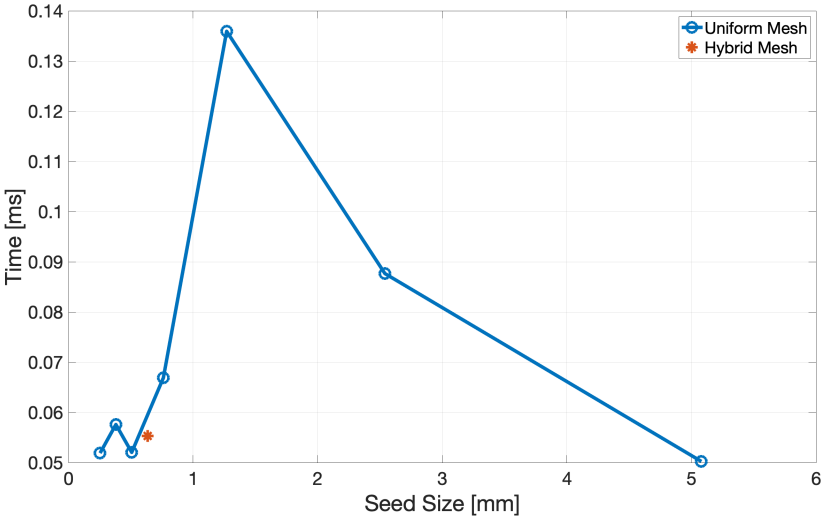

Figure 3.5: Mesh Convergence Analysis: Peak Force Time

This exercise both confirms the validity of the results and offers an optimal hybrid meshing scheme that cut analysis time by upto 60% with minimal consequence on the peak force readout. Figure 3.6 offers a comparison between this hybrid mesh and previously plotted results.

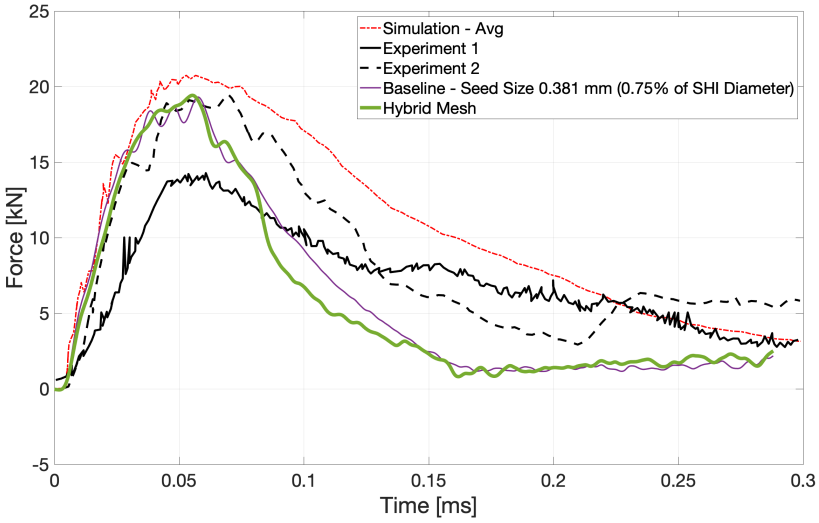

Figure 3.6: Hybrid meshing scheme results contrasted with results from figure 3.2

This model was further validated against published results for SHI of different sizes and velocities. This can be found in appendix A.3 along with the individual force-time histories from the mesh convergence analysis.

3.3. SIMULATION RESULTS

Using the setup of the baseline model as a reference, a number of size-velocity combinations are analysed. The sizes considered are in line with the findings in section 1.1.3 at their respective terminal velocities and are listed in table 3.2. Additionally a worst case scenario of the resultant velocity from a 35 m/s horizontal wind gust is also computed for these size-velocity combinations.

Table 3.2: SHI size-velocity combinations analysed

Diameter $[cm]$	**Terminal Velocity** $[m/s]$	**Resultant Velocity** $[m/s]$ with 35 m/s gust
0.5	10.2	36.5
1.5	17.6	39.2
2.5	22.7	41.7
3.81	28.0	44.8
5.08	32.4	47.7
6.1	35.5	49.9
7.0	38.0	51.7
8.0	40.6	53.6
9.25	43.7	56.0
10.5	46.5	58.2

Upon running an analysis for these 10 size-velocity combinations in the HPC cluster and applying the anti-aliasing filter, the results shown in figure 3.7 were obtained.

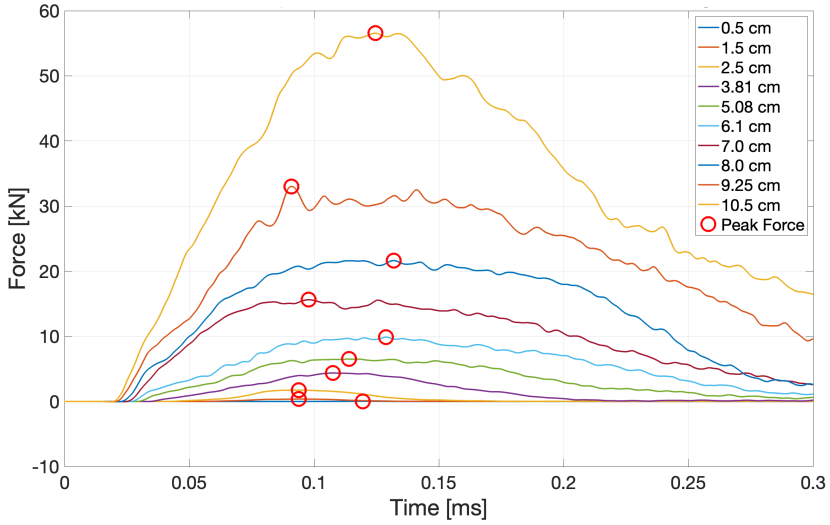

Figure 3.7: Size-Velocity combinations of interest

By isolating just the peak force values and plotting them against their respective sizes, figure 3.8 is obtained. Note that a 3rd order polynomial fit correlates quite nicely with the observed peak force trend and may be used for predicting peak force values for SHI sizes between the ones mentioned in table 3.2. This analysis was repeated taking in to account the resultant velocity arising from a 35 m/s horizontal wind gust to establish the hail impact envelope in figure 3.9.

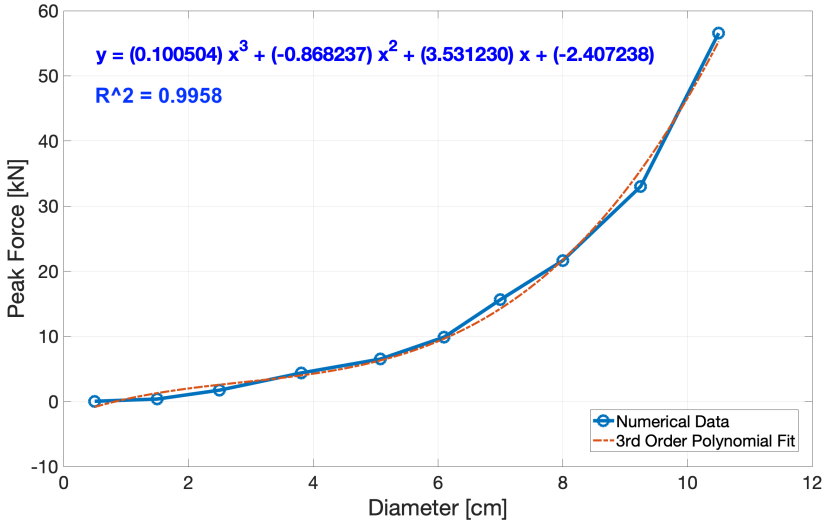

Figure 3.8: Peak force and size relationship at corresponding terminal velocities

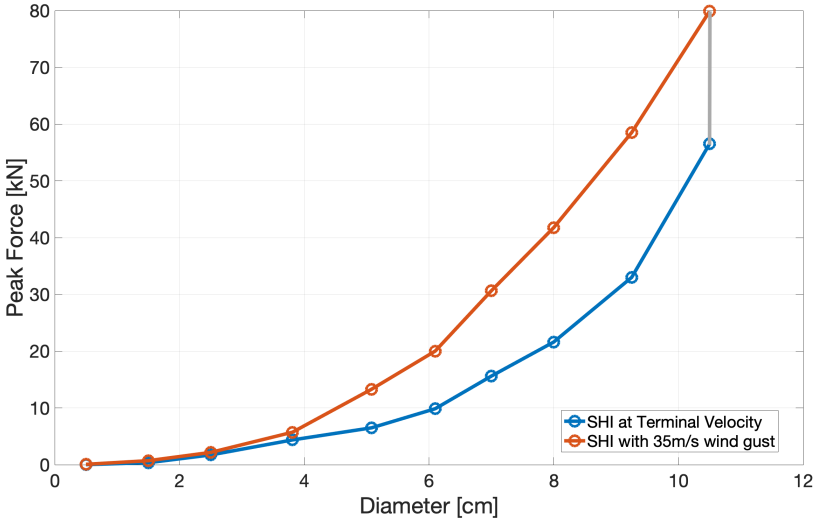

Figure 3.9: Hail impact envelope

3.4. PEAK FORCE VALIDATION

In order to validate these peak force predictions, the analytical model for predicting the peak contact force (F_c) proposed by Sun et al [10] was natively plotted for the size and velocity combinations of interest. This is done so using equation 3.1. This equation has

been reproduced below along with the parametric inputs used, for the convenience of the reader.

$$F_c = k_n \left[1 + (0.2p + 1.3)\left(\frac{1 - COR}{COR}\right)\left(\frac{-b + \sqrt{b^2 + 4c}}{2}\right)\right] \times \left(\frac{p+1}{2k_n} m_1 v_0^2 COR\right)^{\frac{p}{p+1}} \left[1 - \left(\frac{-b + \sqrt{b^2 + 4c}}{2}\right)^2\right]^{\frac{p}{2}} \tag{3.1}$$

$$b = \frac{p \times COR}{(p+2)(0.2p + 1.3)(1 - COR)^2}$$
$$c = \frac{2}{p+2} \tag{3.2}$$

where,

k_n = non-linear stiffness coefficient = $1000 \times ((2.2 \times v_0) + 170.269)$,
p = exponent characterising spring behaviour = $(0.01 \times v_0) + 1.263$,
COR = coefficient of restitution = $(-0.001 \times v_0) + 0.049$,

The mass of the SHI impactor is given by m_1 and the impact velocity is given by v_0. These parameters are set to match the ones listed in table 3.2. This result is comfortably within an acceptable margin of error and is plotted in figure 3.10. It is to be noted that the analytical model by design has a limited scope of validity and cannot yield results for velocity values beyond 48 m/s.

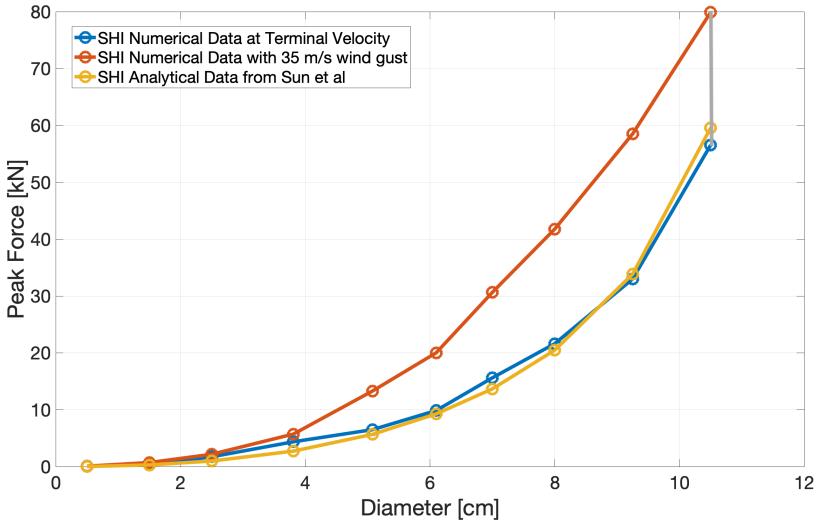

Figure 3.10: Validation of SHI numerical model with analytical data

The fact that a numerical model and an analytical model for peak force prediction developed by two independent research groups confirm each other is deemed sufficient to confirm the validity of the results presented here. In addition to this, impacts with SHI of 2 *cm* diameter were carried out in the DASML at velocities close to terminal and resultant of severe wind gust. Specifics of how this was done is covered in Part II of this thesis. An excerpt of the results are presented in figure 3.11 for the limited purpose of additional validation to the peak force predictions printed here.

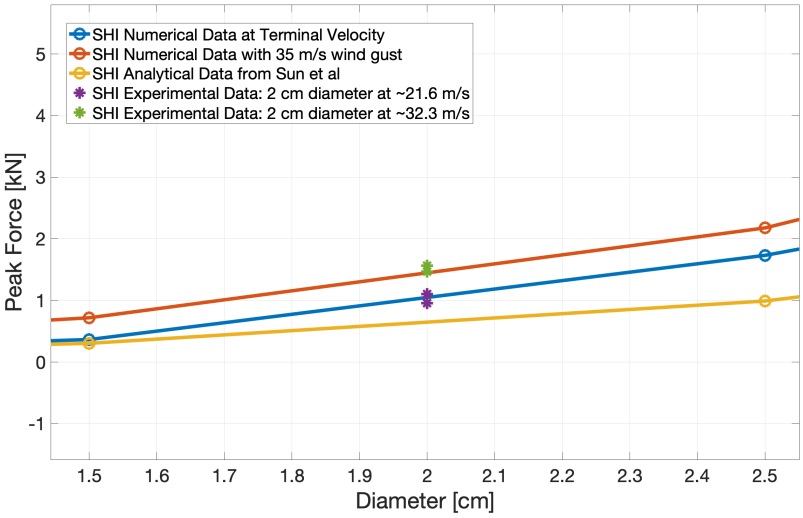

Figure 3.11: Validation of SHI numerical model with experimental data

4

COMPRESSIVE STRENGTH INVESTIGATION

The literature study revealed that natural hailstones were documented to have a higher compressive strength than lab made SHI. Most testing carried out so far with SHI assumes it to be sufficiently representative of natural hailstones based on limited experimental evidence. This chapter attempts to offer more insight into the influence compressive strength may have on the severity of a hail impact incident.

4.1. BASELINE EXPERIMENTS

As a first step to doing this and to get some experience handling SHI, a baseline study is carried out to evaluate the compressive strength of SHI. Five distinct diameters ($1.3, 2.5, 3.8, 4.5$ & $5.1\ cm$) are picked for this purpose which have a good intersection with the diameters used in existing test standards and studies [8, 54]. The mould for making SHI was manufactured via additive manufacturing with PLA filament. Care was taken to account for volumetric expansion of water while under going a phase change to ice with a provision of a vent hole. Additionally, the mould wall was reinforced by increasing wall thickness and infill percentage. The mould was oversized slightly to account for the shrinkage of the mould itself and potential loss of material during de-moulding. Furthermore, care was taken to use only distilled water to closely replicate the chemical composition of natural hailstones and the filling process was done gradually with a syringe to avoid bubbles. A glimpse of this process can be seen in figure 4.1. After filling, the moulds were placed in the freezer at $-22°C$ overnight. After this the SHI was de-moulded, transferred to ziplock bags, weighed and returned to the freezer.

Figure 4.1: Filling of moulds with distilled water using a syringe

The test itself was carried out on a Zwick 20kN Universal Testing Machine (UTM) available at the DASML. Upon noticing excessive melting of the SHI samples on the clamps of the UTM, a temperature controlled chamber was introduced as seen in figure 4.2. This chamber was maintained at $-5°C$ using active liquid nitrogen cooling. A close up image of the sample and clamps can also been seen in figure 4.2.

Figure 4.2: Zwick 20kN UTM with the temperature control chamber

Care was taken to ensure all SHI samples were tested within 60 seconds of removal from the freezer in line with best practice recommendations from other researchers. Moreover, it was ensured all samples tested were within ±5% of the expected weights for each of the tested sizes. The specifics of these quality control measurements can be found in appendix B.1. The measurements itself were carried out at a sampling rate of 500 Hz. The tests were performed at speeds of 1 mm/s and 10 mm/s, with 5 samples being tested for each speed. The variability seen from sample to sample is quite high and hence no discernible differences could be documented between tests carried out at 1 mm/s and 10 mm/s. As a consequence, figure 4.3 has a summary of the results obtained from these tests merged together. Note that the peak is obtained at later stage in some samples due to a portion of the ice chipping away and/or rotating upon loading.

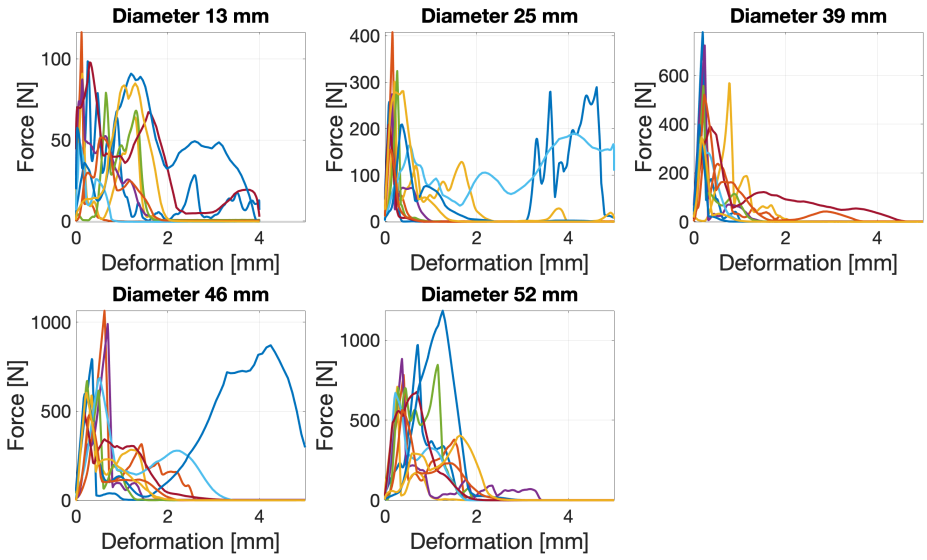

Figure 4.3: Results from SHI compression tests

The peak compressive force observed is compiled in figure 4.4 against their respective sizes and contrasted with data published by Giammanco et al [8]. In spite of the variability observed in testing, the general trend shows a good correlation with published data and serves to expand the same for previously untested sizes. In line with expectations, it can be noted from the length of the error-bars that the variability in peak compressive force readouts increases with size, as with increasing volume the number of defects in the ice microstructure also increases.

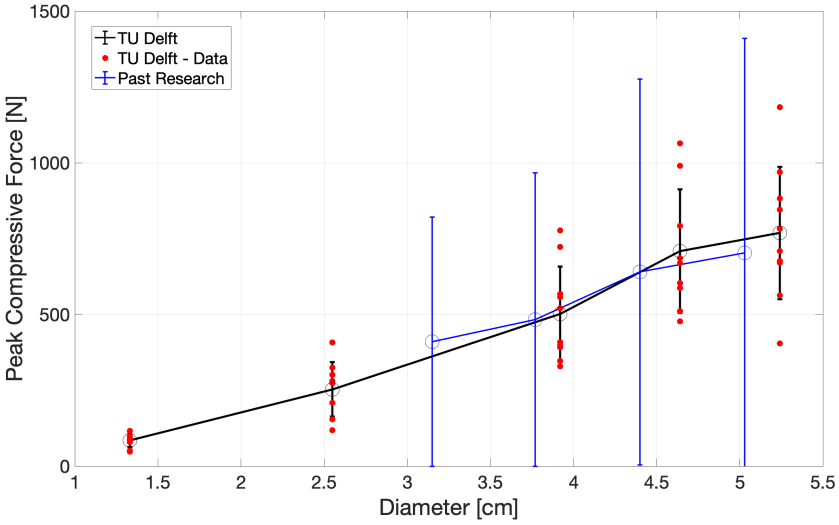

Figure 4.4: Comparison of peak compressive force results with data published by Giammanco et al [8]

4.2. EXPERIMENTS WITH COTTON

It was previously established that tests carried out with the introduction of cotton reinforcement in ice in accordance with ASTM F320 standards [54, 58], led to significantly more damage in CFRP panels when compared to SHI. The cotton weight fraction proposed by ASTM for various sizes are 12% or above. This section attempts to examine if the introduction of a lower weight fraction of cotton reinforcement in SHI could lead to a marginal increase in compressive strength and possibly reduce the variability seen in the pure SHI samples.

For these tests, the same procedure described for pure SHI manufacturing is followed except for the introduction of cotton while filling the moulds, weighed to meet the stipulated weight fractions. The specifics of these measurements can be found in appendix B.2. The result of this manufacturing process can be seen in figure 4.5.

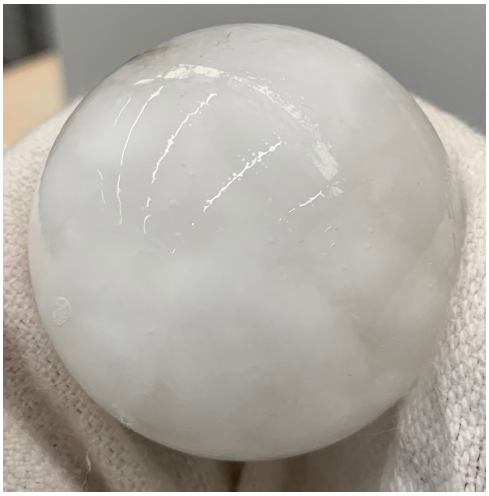

Figure 4.5: SHI with cotton at 10% weight fraction

Upon carrying out the compression tests for cotton reinforced SHI at 10% weight fraction it was immediately apparent than the deformation process was very different from what was observed in pure SHI (see B.1). While the pure SHI grew cracks through the cross section and collapsed after reaching it's peak resistance, the cotton fibre served as an extremely good reinforcement, preventing collapse. This can be seen in figure 4.6.

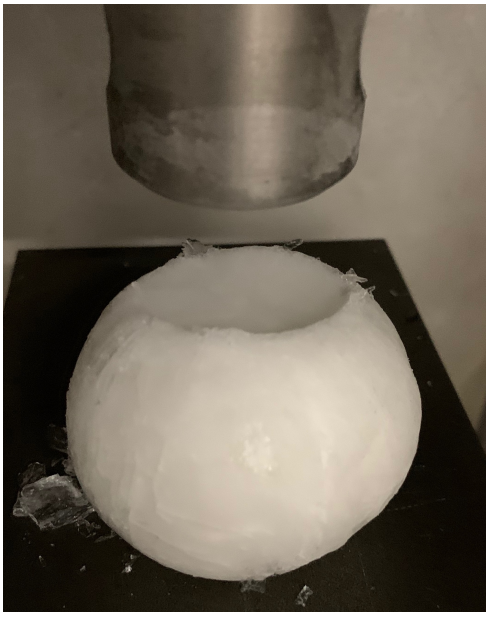

Figure 4.6: Cotton SHI of 5.1 cm diameter and 10% cotton weigh fraction

Correspondingly, the peak compressive force recorded also kept increasing to magnitudes much higher than what was seen in pure SHI. The results obtained for 5 samples of 5.1 cm cotton reinforced SHI at 10% weight fraction can be seen in figure 4.7. These results are also contrasted with the results obtained for pure SHI in the same figure.

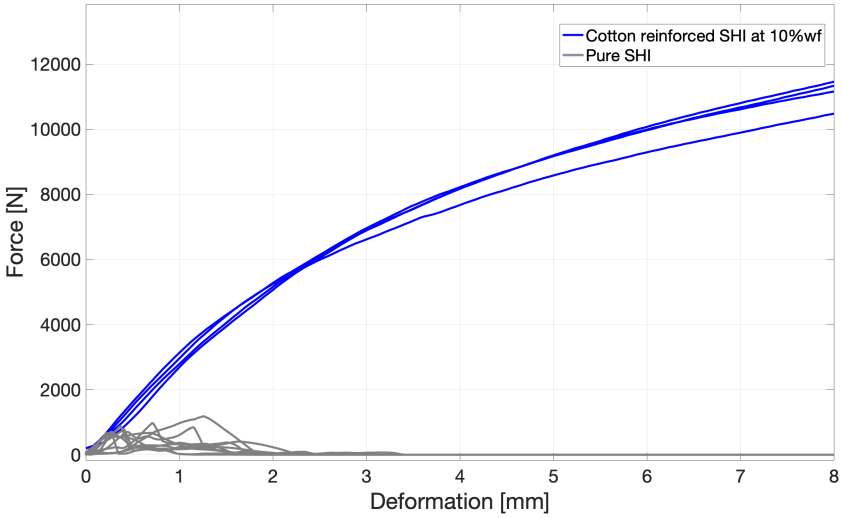

Figure 4.7: Force vs deformation readings for 5.1 cm cotton reinforced SHI at 10% weight fraction

While it is clear that the objective of variability suppression was met, the objective of marginally increasing the compressive strength was not. In an attempt to improve on this, cotton reinforced SHI at 5%, 2.5% and 1% weight fraction was tested as well for the 5 sizes previously identified. However, with the drop in cotton weight fraction, while the peak compressive forces dropped, the variability increased. The deformation process continued to be starkly different from what was observed in pure SHI. In order to take the deformation process closer to pure SHI short cotton fibres (1.5 cm) were also experimented with for the larger samples. From the force-deformation graphs obtained for each of these tests, the peak compressive force is assumed to correspond to the same deformation point as that of pure SHI peak force for the explicit purpose of comparing the results. This assumption is closer to reality for the lower weight fraction cotton reinforced SHI (1%) but could also potentially hold true for impact scenarios in general since the contact duration is minimal. The results so obtained can be seen in figure 4.8. The results of individual compression tests can be found in appendix B.3.

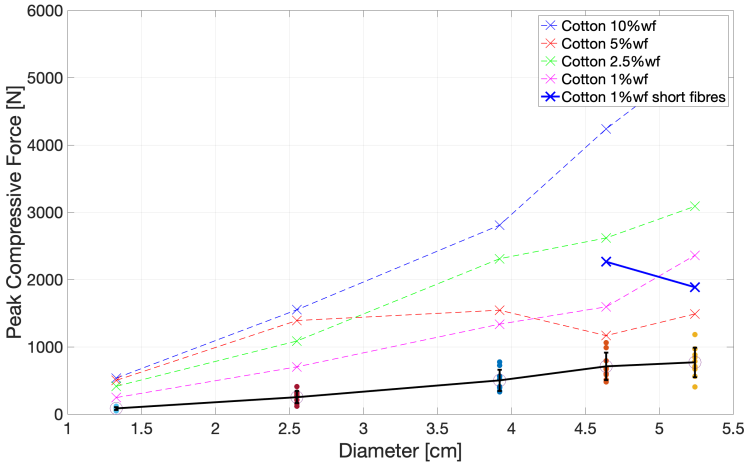

Figure 4.8: Comparison of cotton reinforced SHI at different weight fractions with pure SHI

Since reduction in variability and marginal increase to compressive strength are inversely relate to each other as we decrease the weight fraction of the cotton reinforcement in addition to following a wholly different deformation mechanism, cotton reinforced SHI was deemed to not be representative of natural hailstones. This is also additionally backed up by peak force measurements carried out in the DASML for 2 cm cotton reinforced SHI (at 10% weight fraction) and pure SHI. Specifics of how this was done is covered in Part II chapter 8 of this thesis. Cotton reinforced SHI (at 10% weight fraction) was found to be almost twice as lethal as pure SHI as shown in figure 4.9. The difference in damage evolution is also documented in figures 4.10 and 4.11.

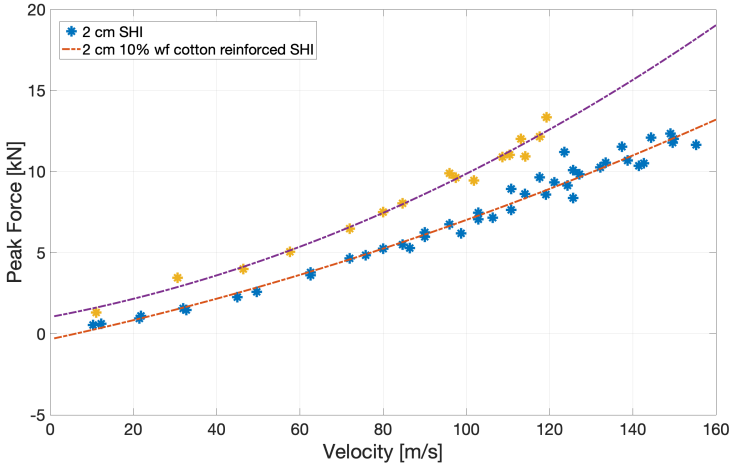

Figure 4.9: Comparison of peak forces generated upon impact by cotton reinforces SHI and pure SHI

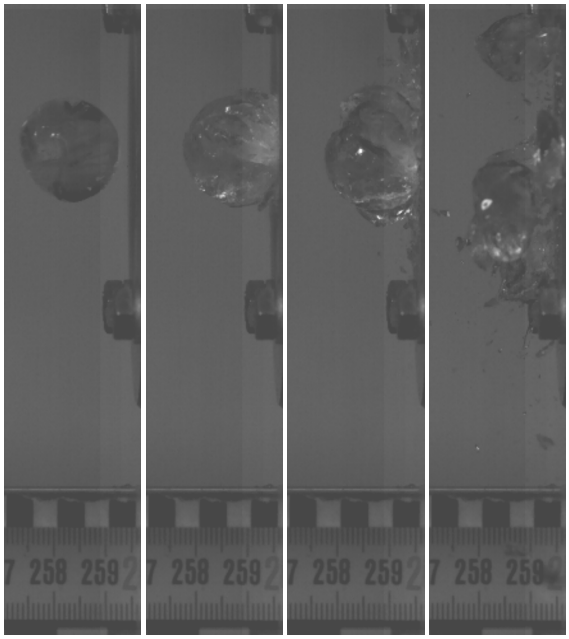

Figure 4.10: Damage evolution in 2 cm SHI impactor at 10.36 m/s

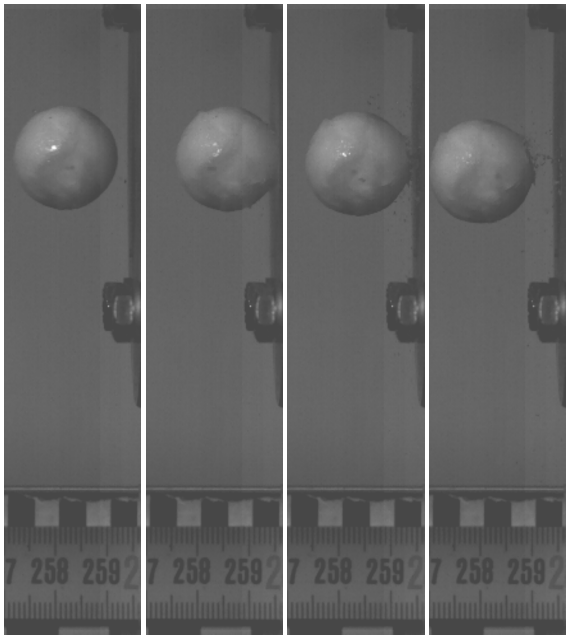

Figure 4.11: Damage evolution in 2 cm cotton reinforced SHI impactor at 11.08 m/s

4.3. NUMERICAL TEST

It was observed that a several fold increase in compressive strength seen in 10% wf cotton reinforced SHI led to the peak force almost doubling. This raises the question of how significant would an 1.5x to 3.0x (context figure 1.9) increase in compressive strength be on the peak forces witnessed during impact. While it would not be easy to experimentally investigate this, tweaking the material parameters in the baseline numerical model developed in chapter 3 offers a simple way to obtain an estimate. The strain rate depended yield strength parameters listed in appendix A.1 are scaled by the following factors: 0.2x, 1.5x, 3.0x & 20.0x. These results are plotted in figure 4.12. It is clear from this graph that a 1.5x to 3.0x increase in compressive strength does not lead to a major change in observed peak forces upon impact. The differences observed may be attributed to numerical noise and be considered to be within acceptable the margin of error.

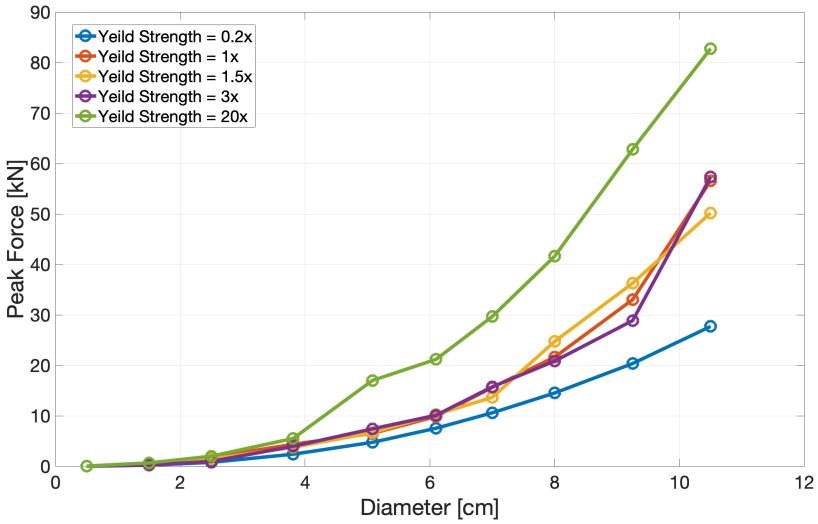

Figure 4.12: Numerical investigation into effect of compressive strength on peak impact force

II

Ice Equivalent Steel Impactor Model

INTRODUCTION: PART II

This part attempts to establish a relation between SHI impactors and impactors made of other materials specifically steel, given most CFRP impact experiments in the past were carried out using them. The first chapter looks at the literature on substitute impactors with the potential to replicate the behaviour of SHI in experimental testing. The actionable points from this chapter is summed up into research questions in the second chapter. The third and fourth chapter attempt to address these research questions through both numerical modelling and experiments in the DASML.

5

LITERATURE REVIEW

5.1. SUBSTITUTE IMPACTORS

5.1.1. METALLIC IMPACTORS

One of the earliest studies on CFRP damage from SHI impact, also carried out impacts at the same KE with aluminium spheres [59]. The results revealed that there were no damages in the specimens impacted with SHI while visible damages could be found in the specimens impacted with the aluminium sphere. While it is noted that due to the difference in material hardness, metallic impactors are not a good substitute to SHI, no further investigations were carried out to investigate a relationship between the two. The sensitivity of CFRP to impactor related properties is well recorded, as described in one of the ASTM standards used to measure damage resistance of Fiber Reinforced Polymer (FRP) to a drop-weight impact event [80]:

"The damage resistance properties generated by this test method are highly dependent upon several factors, which include specimen geometry, layup, **impactor geometry**, **impactor mass**, **impact force**, **impact energy**, *and boundary conditions. Thus, results are generally not scalable to other configurations, and are particular to the combination of geometric and physical conditions tested."*

In testing practices, there already exists a split in methodology. Under very low velocity impact loading scenarios where the capability of the target body to absorb energy is crucial, quasi-static indentation may be deemed a reasonable approximation to projectile impact testing. On the other hand, under high velocity impact loading the projectile induces a local target response and boundary effects are not as important [81].

Prior research has been carried out in TU Delft, with the aim of investigating hail impact on CFRP structures [82]. The scope of this work was focused towards investigating multiple site impacts and its impact on fatigue life of the laminates. Therefore, while acknowledging that the relationship between ice and metallic

impactors is unknown, the research goes ahead with carrying out quasi-static tests with a hemispherical steel indenter. Further preliminary results from unpublished work in progress at TU Delft concurrent to this study suggests that SHI may show a hybrid behaviour. This theory is based on observed results comparing the contact time at the maximum deflection with the incident velocity of the SHI numerical model [83].

Only one research group till date makes a direct comparison between metallic and SHI projectiles [84, 85]. However both the experimental work and subsequent simulations (using the Tippmann model) were carried out at energies corresponding to ballistic impacts. This puts it beyond the scope for any comparison with the parameters identified by this study. However they make the following statement, which has also been the finding of this study:

"To date (2018), there are no direct comparisons of these features (of ice impact) with those of rigid-projectile (metallic) impacts, especially in terms of deformation behaviour during the impact event."

5.1.2. MISCELLANEOUS

As part of a project to investigate the hail impact resistance of various building materials, for handling and economic reasons, the researchers switched over from SHI to polyamide spheres [14]. In this process, there were able to perform a comparative study of the indentation patterns formed on steel sheets. Figure 5.1 is the result of the same. It is clear that damages formed by polyamide spheres of comparable KE are more severe owing to their higher density and resistance to fracture.

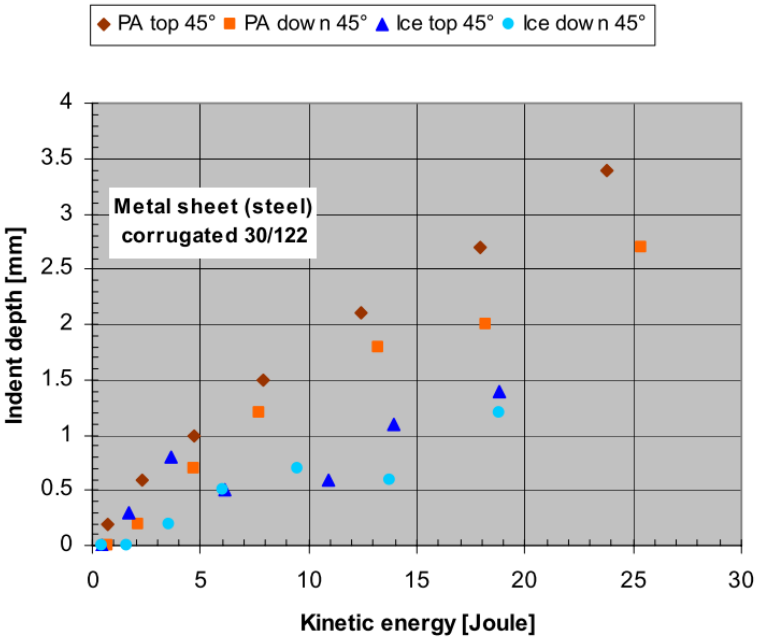

Figure 5.1: Indentation (mm) vs KE (J); Top 45° and down 45° refer to the orientation of the impacted spots in the corrugated steel sheet [14]

Recently a study was carried out to investigate the effects of projectile hardness on CFRP panel behaviour under impact loading [86]. Two projectiles, one soft (Gelatine) and one hard (high-density polyethylene) manufactured to be the same mass were chosen to carry out this experiment. They were propelled to the same velocity so as to keep the KE constant. While the CFRP panel showed the similar values of major strain and out of plane displacement, the harder high-density polyethylene induced more severe damages than gelatine. This has been attributed to the force transfer to the CFRP panel occurring over a larger area in the case of gelatine owing to the flow of the material upon impact. In effect the peak impact force seen by the CFRP panel is higher in the case of the hard projectile.

Another study attempts to estimate the amount of force generated by wind-borne debris upon impact on buildings and other exposed installations [15]. For this materials such as gravel (spherical & irregularly shaped), wooden spheres, brick spheres and concrete spheres are impacted upon a spring-lumped mass force measurement apparatus (same as the one described in section 1.2.1.2). These tests are carried out within the size and velocity parameters relevant to this study. Of these the wooden spheres may be of some significance given its density ($704 kg/m^3$) is closest to that of solid ice ($917 kg/m^3$). In figure 5.2 a preliminary comparison between the two can already be made. Though the size and velocity of the spheres are nearly the same, there

is a mismatch in KE due to the difference in densities. Note that the inertial force peaks at a similar time scale, but the peak for the wooden sphere is over 3 times larger, most likely a consequence of the material hardness.

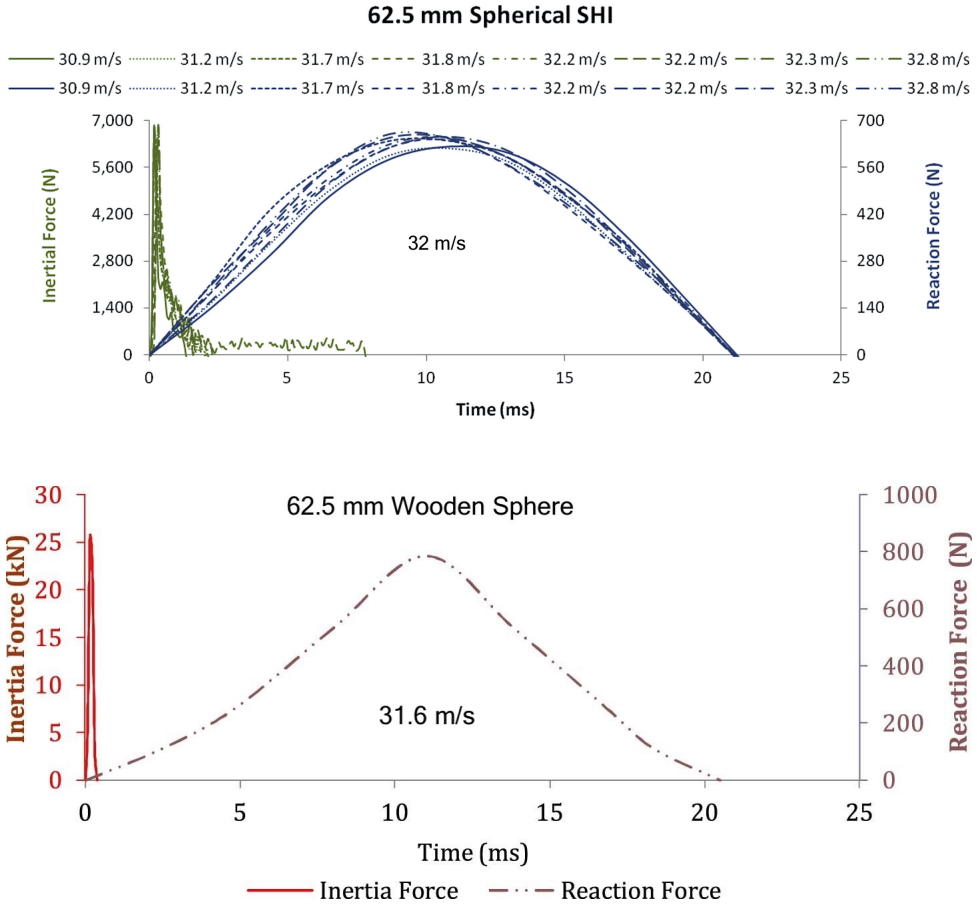

Figure 5.2: Inertia force and reaction force generated by SHI and wooden ball [10, 15]

5.1.3. SYNOPSIS

Currently there are no established substitutes for SHI for impact testing. A potential equivalence relation between SHI and steel would have a far reaching impact, as numerous impact/ indentation experiments carried out both in TU Delft and outside can be projected to its hail ice (mass & diameter) equivalent. It is also possible that another material that does not involve the complications in handling that comes with SHI could stand in as a substitute for testing. While a few interesting options found in literature were presented here, a better understanding of the ice impact phenomenon could help find a more suitable substitute.

6

Research Questions

Given the peak forces for a range of hail impact scenarios have been mapped out, based on this can a different material such as steel act as a substitute in impact tests?

- How much more severe is a steel impact when compared with an ice impact?
- Given a vast majority of impact tests are carried out with steel impactors/ quasi static indenters is there a relation to be drawn between steel and ice?
- Is there another material that's easier to handle than ice and can exhibit similar behaviour up on impact?

What is the behaviour of CFRP structures when exposed to the results of the above questions?

- What is the least severe impact scenario that has the ability to cause delaminations?

7

NUMERICAL MODEL OF STEEL IMPACTOR

This chapter attempts to form a relation between a SHI impactor and a metallic impactor. In order to do this the numerical model described in chapter 3 is modified with the replacement of the ice material properties with that of steel. The material properties used are of Stainless Steel 430F, a commonly used raw material in the DASML. These properties are listed in table 7.1.

Table 7.1: Summary of material property definition for stainless steel 430F

Property	**Value**
Young's modulus	200000 MPa
Poisson's ratio	0.285
Density	7800 kg/mm^3

Following the same post processing methodology as before, a comparison of SHI and steel data is made in figure 7.1. Note that the size and velocity combinations used for SHI (table 3.2) are used as is for the explicit purpose of highlighting how much more severe a steel impactor is.

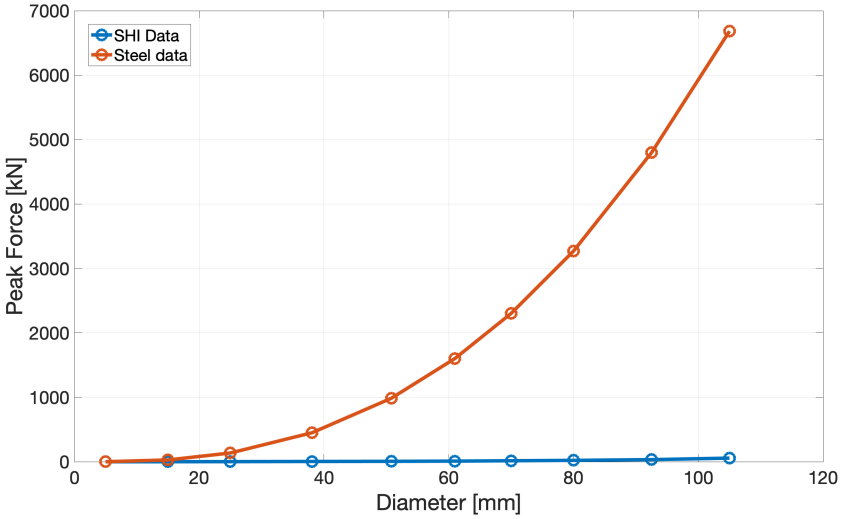

Figure 7.1: Comparison of peak force generated by SHI and steel impactors at similar size and velocity combinations

It is clear that any comparison between steel and SHI that is going to be made will be at the lower velocity regime of steel impactors ($<< 50\ m/s$). For this reason, it was elected to continue with the elastic material model described in table 7.1 and not include plasticity effects.

7.1. EQUAL ENERGY APPROACH

Researchers in the past [82] have taken the equal energy approach where the kinetic energy of SHI prior to impact is taken as an input parameter for quasi-static indentation and drop tower impacts. The same approach is considered here to evaluate the actual severity of a steel impact even when energy is equivalent to that of a hailstone. The results of the calculation made in this regard are shown in table 7.2. For computing equivalent velocity, a constant mass of 63.81 g which amounts to a diameter of 2.5 cm is considered. This number was picked as the impact gun available in the DASML can only accommodate a maximum diameter of 2.5 cm. For computing equivalent mass, a constant velocity of 25 m/s is considered.

Table 7.2: Summary of equal energy computation for steel impactor

SHI Properties				Steel Properties	
Diameter (cm)	**Mass (kg)**	**Velocity (m/s)**	**Kinetic Energy (J)**	**Equivalent Velocity (m/s)** (for constant mass)	**Equivalent Diameter (cm)** (for constant velocity)
0.5	0.00006	10.2	0.003	0.31	0.13
1.5	0.00162	17.6	0.25	2.80	0.58
2.5	0.00750	22.7	1.93	7.78	1.15
3.81	0.02655	28	10.41	18.06	2.01
5.08	0.06294	32.4	33.04	32.18	2.96
6.1	0.10898	35.5	68.67	46.39	3.78
7.0	0.16469	38	118.90	61.05	4.53
8.0	0.24583	40.6	202.61	79.69	5.41
9.25	0.38001	43.7	362.85	106.64	6.58
10.5	0.55582	46.5	600.91	137.23	7.78

With these equivalent sizes and velocities, the numerical model is rerun to generate new peak force estimates. These results are plotted in figure 7.2. From the figure it is clear that in both cases a similar trend is observed when it comes to peak force. However from a practical point of view, it is much easier to use one impactor and vary the velocity rather than the other way around. It is to be noted that even under equal initial energy conditions, steel impact is estimated to be several folds more severe than a SHI impact.

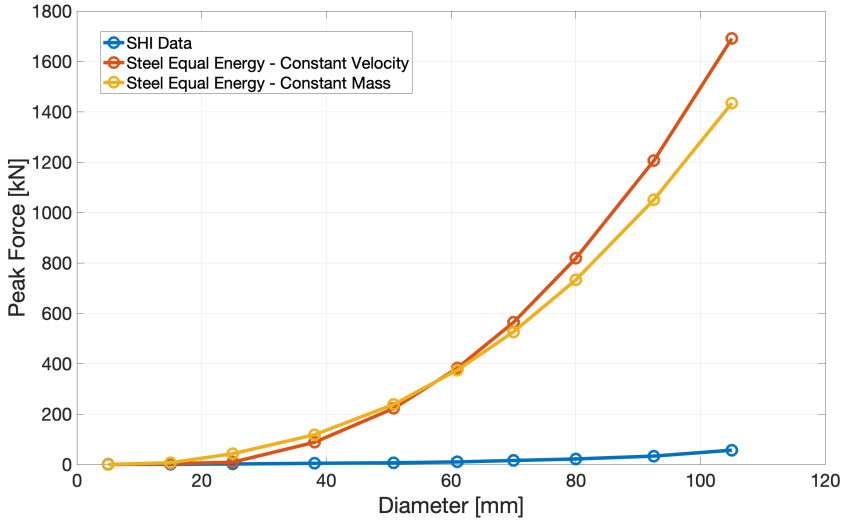

Figure 7.2: SHI data compared with equal energy steel impactor data

7.2. INTRODUCING IESIM

Zooming into the peak force graph for the constant mass steel impactor case and replacing the x-axis with velocity, figure 7.3 is obtained. Note that a few more equal energy cases were added to obtain a good curve fit. This second order polynomial fit is also displayed in figure 7.3.

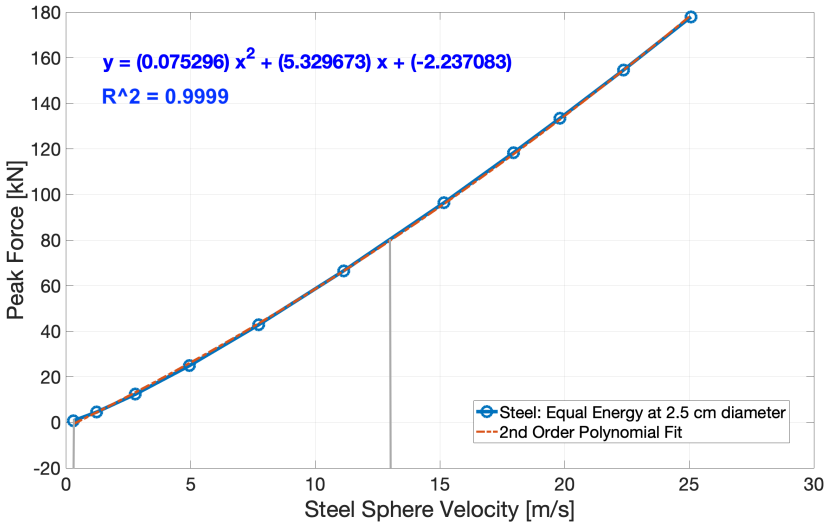

Figure 7.3: Steel constant mass impactor peak force vs velocity

Comparing this with the peak forces obtained from the SHI numerical model in figure 3.9, it is clear that impacts between 0 m/s to 13m/s with this constant mass steel impactor are sufficient to cover the whole range. This leads to the proposal of an Ice Equivalent Steel Impactor Model (IESIM). This model is fundamentally a one to one mapping of peak forces seen in the hail impact envelope (see figure 3.9) with a similar peak force obtained with the steel impactor. This was achieved by the means of a simple MATLAB script (see appendix C) which takes the required peak force as an input and outputs the corresponding steel impactor velocity using the second order polynomial relation derived here. This functionality was confirmed by rerunning the steel numerical model with the velocity prescribed by the IESIM with verification of the desired peak force.

It is important the establish a limit of validity at this point for the IESIM. It is well documented that for low velocity impacts, the damage creation is primarily deformation driven and the boundary conditions play an important role. For higher velocity impacts, the damage creation is dynamic and is primarily driven by the local stress wave. The effects are localised and the boundary conditions do not play a major role. Therefore this model is only applicable where both the ice impact effect to be replicated and the steel impactor fall under the low velocity regime. The velocity threshold for this transition

changes from material to material but at this stage the velocities considered under the IESIM are assumed to fall under the low velocity regime for both SHI and steel.

The IESIM also offers an unique insight into the portion of initial KE that eventually contributes to the peak impact force. Table 7.3 lays out the energy differences between a SHI impactor and IESIM steel impactor to achieve the same peak impact force. Relatively speaking, on average less than 1% of the initial energy goes into the peak force generation in the case of SHI. While it is noted that SHI impacts tend to not have a sharp peak in the force-time history plot and sees a relatively more prolonged impact event, a vast majority of the energy is still lost due to the crushing effect.

Table 7.3: Energy comparison between SHI and IESIM

Peak Force (N)	**SHI KE (J)**	**IESIM KE (J)**	**Energy Difference (%)**
0.39	0.251	0.008	96.94
1.75	1.934	0.017	99.10
4.72	10.435	0.052	99.50
7.22	32.978	0.096	99.71
11.31	68.563	0.192	99.72
17.49	118.895	0.397	99.67
23.24	202.830	0.645	99.68
36.27	362.526	1.393	99.62
57.38	601.908	3.079	99.49

8

EXPERIMENTAL VALIDATION

Experimental validation is crucial to confirm the practical applicability of the IESIM. The first aspect needing validation is the peak force estimate drawn up for the 2.5 cm steel impactor. The second aspect is a comparison of the damages produced in CFRP panels by a SHI impactor and an IESIM impactor. The common thread between these two aspects is the steel impactor itself. While the numerical models utilise a spherical impactor, this is not aerodynamically optimal for carrying out tests with the impact gun available in the DASML. This impact gun has a barrel diameter of 2.5 cm and capable of pressurising up to 30 bar. Taking inspiration from impactor designs of previous researchers, the impactor shown in figure 8.1 was manufactured. The tip of this impactor was made of Stainless Steel 430F and has a diameter of 2.5 cm. The total weight was tailored to match that of the numerical model.

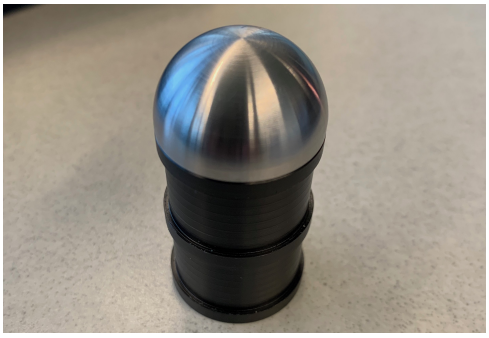

Figure 8.1: Steel impactor designed to be used for IESIM validation

8.1. SPRING-LUMPED MASS SETUP

As determined in section 1.2.3 the spring-lumped mass force measurement setup showed the most promise for carrying out these measurements. Taking inspiration from

Sun et al [10], a similar force measurement setup was build in the DASML with a few improvements. The principle of working is the same as what was described in section 1.2.1.2 and figure 1.15. However the spring displacement measurement is now carried out using a Laser Displacement Sensor (LDS) placed behind the impactor facing lumped mass. This provides the possibility of utilising a stiffer spring as the cumbersome task of tracking the spring displacement need not be done manually using High Speed Camera (HSC) footage. This in turn affords the possibility of using a much heavier impactor facing lumped mass without the spring sagging downwards. This heavier mass allows the utilisation of an accelerometer of relatively lower range ($\pm 500\ g$) when compared to the shock accelerometer ($\pm 2500\ g$) used by Sun et al [10]. The lower range accelerometer cost one-tenth the price tag of the shock accelerometer and still comfortably met the measurement requirements.

A number of parameters are simultaneously tracked while carrying out these measurements. The impact gun requires a pressure setting to fire, and offers no guarantee of the impactor velocity being reproducible. For this reason in addition to the pressure setting, the velocity of the impactor is tracked for each test with the help of the HSC and the distance ruler. This ruler along with the rest of the setup can be seen in figure 8.2. For the sake of versatility, the impactor facing lumped mass was built as two connectable masses. The first mass along with the spring attachment clamps weighs 2.044 kgs in total. Both masses put together along with the connecting bolts and spring attachment clamps weighs 4.239 kgs. Ultrasonic gel was applied in the interface between these masses to suppress noise in the accelerometer readings. The spring was subjected to compression tests in the DASML at two different speeds and the spring constant was found to be approximately 115 N/mm. Additional details on this compression test, assembly and calibration process can be found in appendix D.

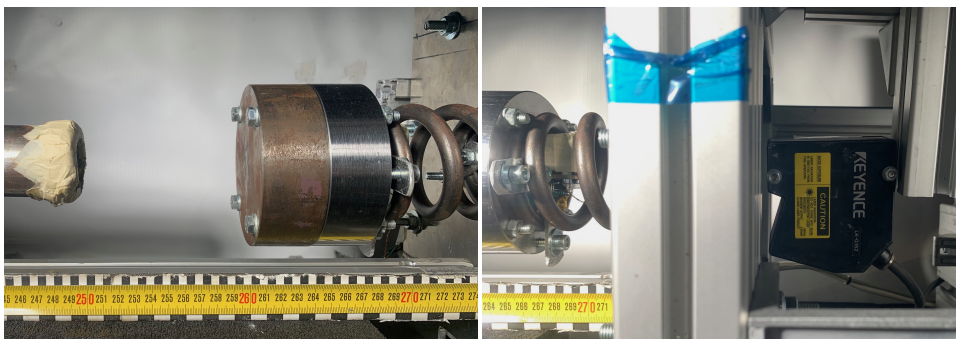

Figure 8.2: Spring-lumped mass force measurement setup

Data acquisition was carried out at a frequency of 128 kHz, more than 5 times the maximum sampling frequency of the accelerometer ($24kHz$) in order to ensure the peak is captured in the measurement. The same data acquisition system was used to gather data from the LDS (sampled at 50 kHz) as well. The second order Butterworth

filter described in section 3.2.1 was utilised here as well to filter out noise. For the accelerometer the cutoff was set to $24kHz$ and for the LDS the cutoff was set to 10 Hz. As an additional check, the power supply voltage to the accelerometer was tracked to check for any fluctuations. A plot of these readouts can be seen in figure 8.3. These voltage readouts were subsequently post-processed to obtain peak displacement and peak acceleration values to compute the peak impact force in MATLAB. A close up look at the accelerometer mounted on the lumped mass along with the laser tracker of the LDS can be seen in figure 8.4.

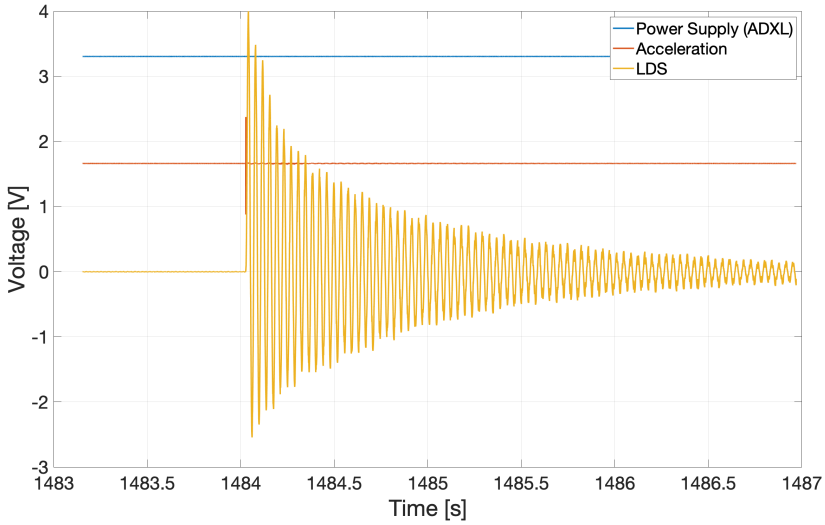

Figure 8.3: Data acquisition system output

Figure 8.4: Close up view of the accelerometer and laser tracker of the LDS

8.1.1. IESIM VALIDATION

Following the methodology described above, a series of tests were conducted with the steel impactor shown in figure 8.1. The first set was conducted with just one lumped mass attached to the spring. This setup has a designed measurement limit of around 10 kN for the peak force. The second set was conducted with both masses attached to the spring with ultrasonic gel at the interface. This setup has a designed measurement limit of around 20 kN for the peak force. A frame from the HSC footage of one of the tests is shown in figure 8.5. Note that the spacing between the barrel of the impact gun and impactor facing lumped mass is kept to 10 cm for all the tests. This was done since the impactor starts to drop quite steeply due to gravity at lower velocities. Limiting the spacing enabled measurements to be made before the vertical component started to dominate the heading of the impactor.

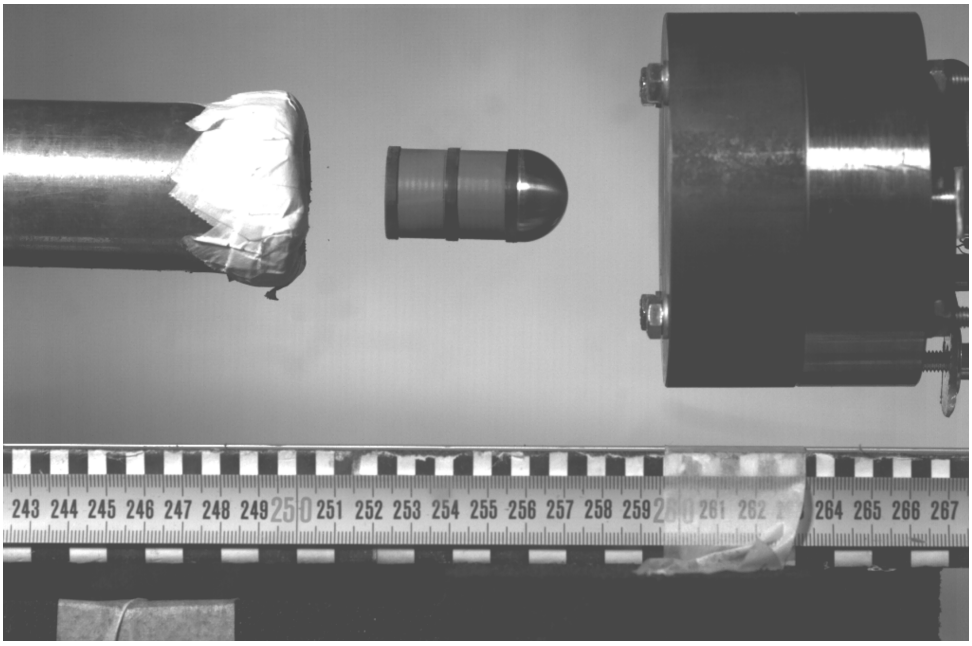

Figure 8.5: Screenshot from the HSC footage of the steel impactor

The results from these tests are juxtaposed against the lower end of the IESIM numerical predictions made in figure 7.3 and plotted in figure 8.6. It is reasonable to see some deviations given a number of factors such as the rigidity of the setup, flexure in the backplate the spring is mounted to, sensor errors and air friction are not taken into account in the numerical model. That said, the obtained results follow the predicted trend quite well and are deemed satisfactory for validation of the IESIM. Addition information on the data gathered for individual tests can be found in appendix E.

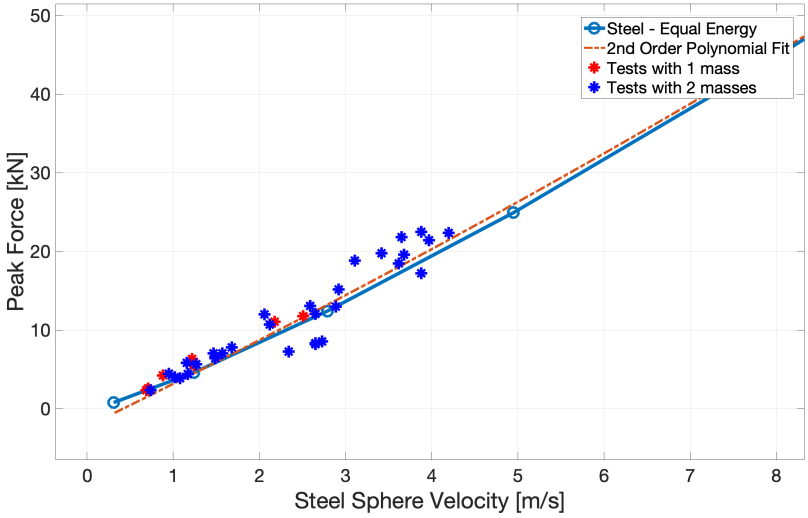

Figure 8.6: Validation of IESIM

8.1.2. ADDITIONAL TESTS

Given this force measurement setup was built and available, a few additional tests were carried out to complement the results obtained in Part I of this thesis. However in order to do this constraints presented by the diameter of the impact gun barrel and express melting of the ice when in contact with the steel barrel had to be addressed. A number of options were tried out but the solution that showed most promise was to insert a plastic tube with an external diameter of 2.5 cm and an internal diameter of 2 cm into the impact gun barrel. While this further limited the SHI test sizes, it provided a way to achieve consistent impacts with no compromise to the integrity of the SHI. Additional details about this constraint and solution can be found in appendix F.

The same manufacturing and handling procedure mentioned in chapter 4 was followed to carry out tests with 2 cm SHI. Using these 2 cm SHI samples, first the additional validation results shown in figure 3.11 were obtained. Following this peak force measurements were carried out for cotton reinforced SHI (10% wf) and pure SHI for a wide range of velocities. These results can be seen in figure 4.9. The images shown in figures 4.10 and 4.11 we captured by the HSC while carrying out these tests.

8.2. DAMAGE IN CFRP PANELS

The second aspect to confirm was to check if the damages produced in a CFRP panel by a SHI impactor and IESIM impactor produced comparable damages. The limit of validity for such a comparison was already established in chapter 7 for a generic case. Specific to CFRP panels, the ideal scenario for comparison would be in the case of a thin panel.

The expectation was that in the case of a thin laminate the delamination when subjected to a low velocity impact is driven primarily by the bending of the laminate and would be found at the back of the panel.

For the purpose of these tests, 18 CFRP panels with dimensions 30 cm X 15 cm were manufactured. These were 8 plies thick with a symmetric quasi-isotropic layup with a stacking sequence as follows: $[0\ 45\ 90\ -45]_s$. These specifications were picked to ensure the test results would be comparable to previously published work [79]. More details on the material, curing and cutting can be found in appendix G. Once the samples were ready, they were subject to a quality check in the form of a C-scan. These results can be found in appendix H.

Since maximum versatility in peak force generation is available with the IESIM impactor, the first series of impacts are carried out with them to identify the point at which BVID initiates. A screenshot from this test is shown in figure 8.7. Table 8.1 contains the specifics of each of these impacts along with their peak impact force and initial KE estimates. Note that for the c-scans a signal difference of 4dB or higher is considered as a delamination/ damage.

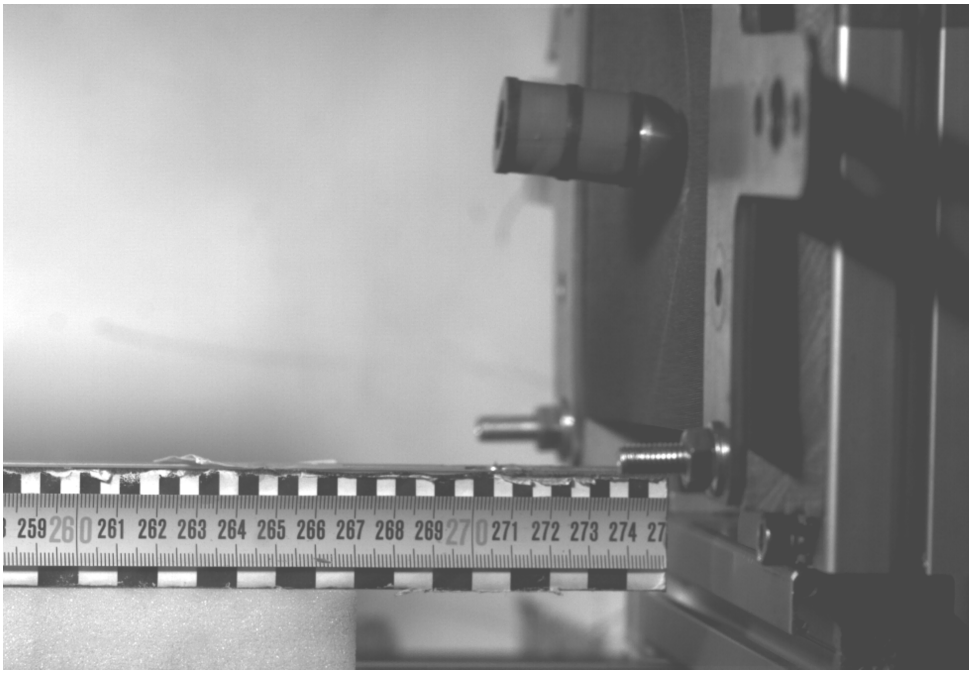

Figure 8.7: Screenshot from HSC footage of CFRP impact tests

Table 8.1: CFRP impact tests

Test no.	Velocity (m/s)	CFRP panel no.	Damage	Peak Force (kN)	KE (J)	Figure
1	4.95	3	No	25.99	0.70	8.8
2	11.90	4	No	71.84	4.06	8.8
3	17.24	5	Yes	112.03	8.53	8.9
4	21.74	6	Yes	149.22	13.56	8.9
5	13.51	7	Yes	83.51	5.24	8.10
6	14.71	8	Yes	92.46	6.21	8.10
7	10.00	9	No	58.59	2.87	8.11
8	12.20	10	Yes	73.99	4.27	8.11
9	150.00	1	Yes	12.10	49.22	8.13

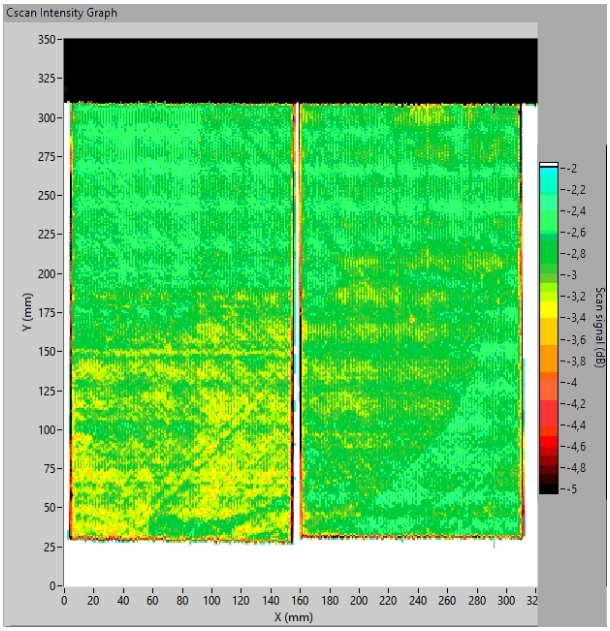

Figure 8.8: C-scan of CFRP panels 3 (left) and 4 (right)

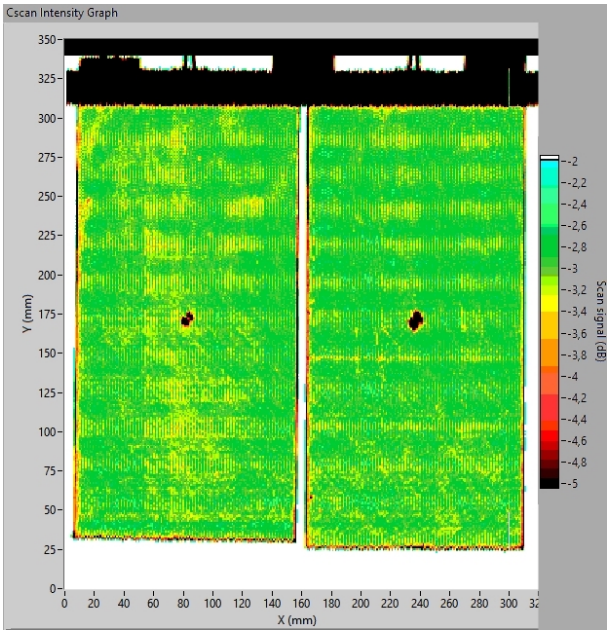

Figure 8.9: C-scan of CFRP panels 5 (left) and 6 (right)

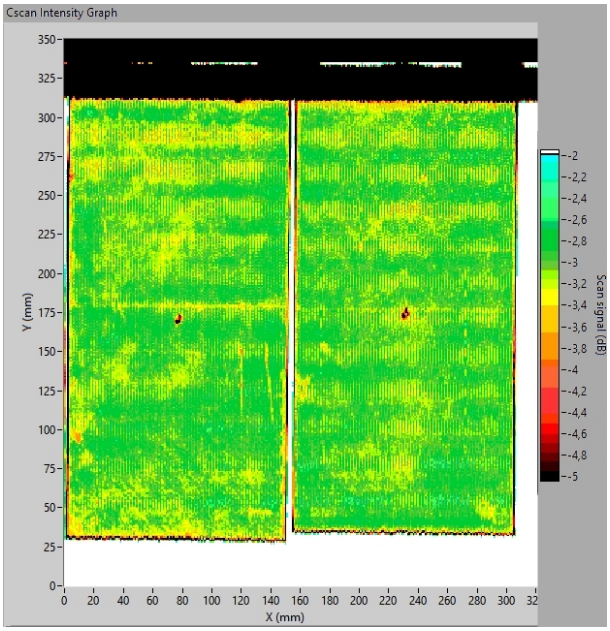

Figure 8.10: C-scan of CFRP panels 7 (left) and 8 (right)

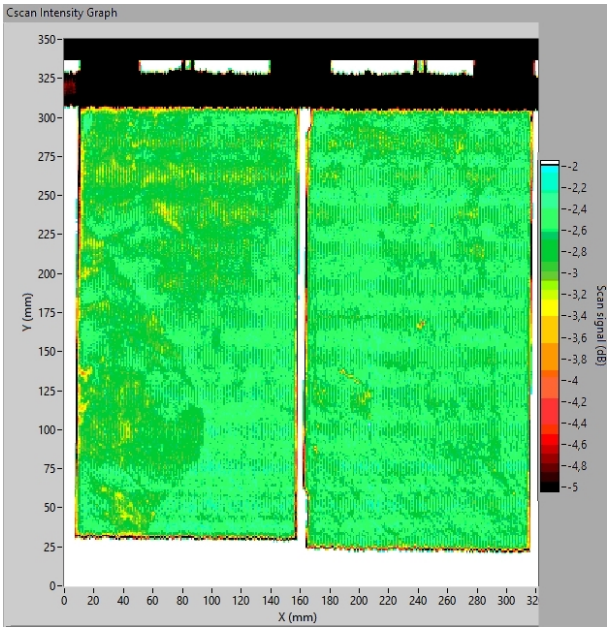

Figure 8.11: C-scan of CFRP panels 9 (left) and 10 (right)

From these tests, the BVID threshold was found to crossed at approximately 12 m/s. It was additionally verified that no damage initiation took place below this velocity even under repeated impacts. More specifics regarding this can be found in appendix H. From the IESIM graph this velocity is found to correlate to a peak force of approximately 72 kN. With a quick hand calculation the initial KE was found to be 4.13 J. It is however not possible to create such a peak force with SHI at low velocity with the available impact gun. An attempt was made to measure the maximum possible peak force that can be generated with a 2 cm SHI. As shown in figure 8.12, a force of approximately 13 kN can be generated when the SHI is propelled to 150 m/s. An experiment was run nonetheless to see the effects of such an impact. As expected the stress wave takes precedence causing significant damage to the CFRP panel as seen in figure 8.13. The limits of validity of the IESIM no longer hold in this case.

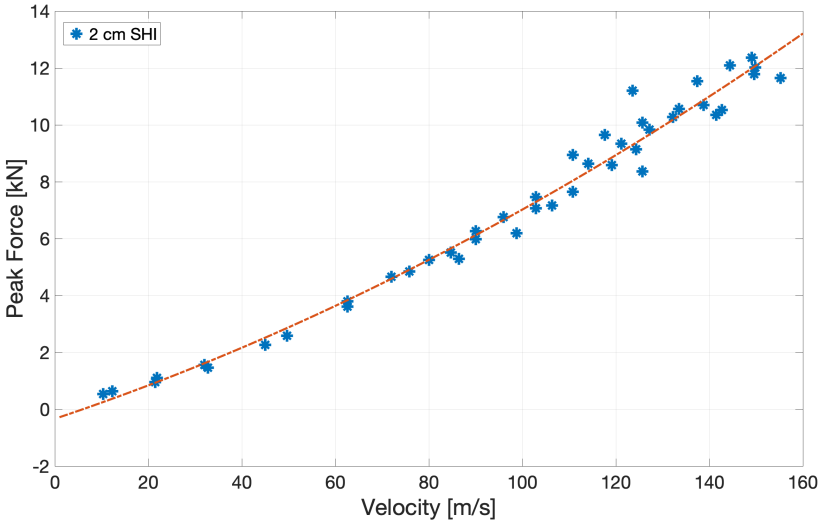

Figure 8.12: Peak force vs velocity plot for 2 cm SHI

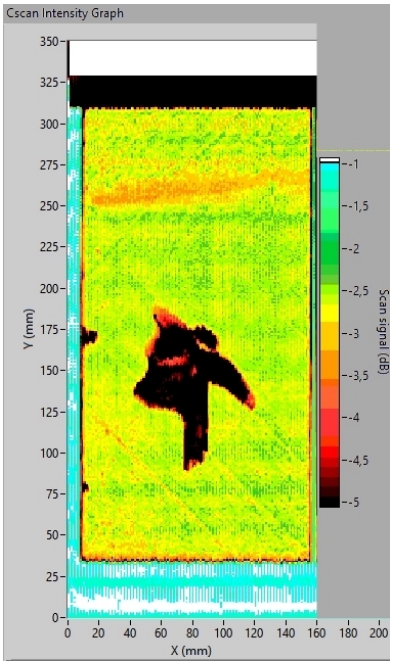

Figure 8.13: C-scan of CFRP panel 1

While the practicality of the IESIM could not be tested to it's full extent due to

limitations imposed by the impact gun available in the DASML, the least severe impact scenario with the ability to trigger delaminations was identified. Translating this IESIM peak force of 72 kN this into its hailstone equivalent would imply that only hailstones larger than 14 cm in maximum dimension subject to heavy wind gust will have the ability to trigger delaminations in thin CFRP panels following a single impact. This size estimate was obtained by identifying the equivalent diameter from the hail impact envelope (figure 3.9) and utilising equation 1.2 to calculate the maximum dimension.

While a recent publication by Spronk et al [87] states that low velocity impacts and quasi-static indentation cannot be interchanged and compared for material characterisation, for the limited purpose of offering additional insight to previously performed quasi-static indentation this is considered acceptable. The result of delamination being triggered at 4.13 J for an 8 ply laminate fits in nicely with the result of quasi-static indentation triggering delaminations at 6 J in a 16 ply laminate obtained by previous research at TU Delft [82]. Mapping back to its hailstone equivalent, this would approximately be comparable to a maximum dimension of 18 cm. These results however require additional verification by testing with SHI impactors. From chapter 1 it is know that the probability of encountering hailstones of such large sizes is extremely low and the probability of multiple such impacts in the vicinity of each other is even lower.

III

Closure

9

CONCLUSIONS

This study has clearly established a hail impact envelope that an aircraft on the ground may be subject to both in terms of initial kinetic energy and peak impact force. This envelope takes into account a wide range of hail parameters such as size, shape, velocity and prevailing winds making this the most comprehensive assessment found in literature that the author is aware of. This was done with the aid of a numerical model developed by Tippmann et al [11], which was previously untested in the low velocity regime. This study validates the functionality of this model using existing literature and experiments in the DASML.

Contradictions found in literature over the influence of the compressive strength of natural hailstones and as a consequence the validity of tests performed with SHI were examined. The marginal increase (1.5x to 3x) in compressive strength seen in natural hailstones when compared to SHI was found to have negligible contribution to the peak force. This leads to the conclusion that lab made SHI is a good enough representation of natural hailstones in testing. The compression tests carried out with pure SHI additionally serve to expand the available literature for previously untested sizes. Furthermore, the experiments with cotton reinforced SHI failed to meet their planned objectives of marginal compressive strength enhancement and variability reduction. While it was documented that cotton reinforced SHI at 12% wf and above was more lethal than pure SHI, this study attaches a number to that. Cotton reinforced SHI at 10% wf was found to be almost twice as lethal as pure SHI. While it is a matter of comfort that aircraft windshields are tested with cotton reinforced SHI, it is definitely an overestimate. The differences in damage evolution for both these impactors are also documented in this study.

This study indicates that the peak impact force might be a better measure to evaluate hail impacts as compared to the initial KE. This is done on the basis of most of the initial energy being lost in the crushing process of ice. It was found that to generate the same peak force with a steel impactor, less than 1% of the initial KE was required on average.

Under the conditions of low velocity impact and displacement driven damage evolution a steel impactor in principle has the same effect as that of an ice impact of comparable peak force. A one to one mapping of steel impactor peak forces was carried out with SHI peak forces with the introduction of the IESIM. Numerical predictions of these peak forces were validated with experimental results obtained using a custom built spring-lumped mass force measurement system.

As setup in the introduction, this study has managed to offer some insights into the threat levels posed by hailstones to composite aircrafts on the ground. Primary CFRP aircraft structures tend to be thicker [88] and therefore stronger than the 8-ply laminates tested in this study. This in tandem with the damage tolerant design philosophy would indicate that hailstones, under the parameters identified in the hail impact envelope, are unlikely to seriously compromise structural integrity. While further investigation is warranted using SHI for the testing, this study does not find cause for any serious alarm. Detailed documentation from Maintenance, Repair & Overhaul (MRO) organisations on the type of damages seen on exposed composite aircraft structures due to hailstones would be an important tool to steer the direction of further research.

10

RECOMMENDATIONS

10.1. PRIMARY RECOMMENDATIONS

There are two primary recommendations based on this study for future research. The force measurement apparatus put together for this study (with appropriate adjustments) and the methodology of the IESIM can assist in carrying out both these recommendations. The first is the use of an impact gun with a larger barrel size to verify the similarity of damages created in CFRP panels by the IESIM impactor. A barrel size of at least 10 cm is recommended for this purpose in order to ensure the requisite peak forces (> 72 kN) are reached within the low velocity regime.

The second is to explore if the use of another material for the impactor will yield results that replicate SHI characteristics better. Even though a relation was drawn between steel and ice, the differences in impact speed and material properties are vastly different. Potential alternative material options to look at in the increasing order of manufacturing complexity are PLA, wood and rubber. PLA impactors can be 3D printed in bulk while retaining good control over weight and shape. The density of wood is comparable to that of ice and provides additional benefits of being slightly pliable while potentially maintaining integrity under repeated low velocity impacts. Rubber impactors will have the ability to better replicate the more prolonged impact event however the weight and stiffness will have to be tuned to obtain optimal results.

10.2. SECONDARY RECOMMENDATIONS

Other methodologies may be tried out for material property variability suppression in SHI if extensive testing has to be carried out with the same. Based on the observations with cotton reinforcement, thicker yarns of a short length (1.5 cm) of either cotton or wool could hold potential. The reasoning behind this is that thicker yarns can suppress crack propagation while not completely changing the damage evolution process due to

poorer adhesion between the fibre and the ice matrix.

If the relation between a metallic impactor and SHI impactor is to be pursued further with the current impact gun in the DASML, it may be a good idea to switch to an aluminium impactor. Aluminium at the same volume has a lower weight than steel, implying it may be fired at a slightly higher velocity to produce the same peak force. Experience indicates that this will result in much better control.

IV

Appendix

A

ABAQUS NUMERICAL MODEL

A.1. STRAIN RATE DEPENDENT YIELD STRENGTH

Table A.1: Strain rate dependent yield strength for ice (source [11])

Stress Ratio	**Strain Rate** (s^{-1})
1	0
1.01	0.1
1.495577759	0.5
1.709011483	1
2.204589242	5
2.418022966	10
2.913600725	50
3.127034449	100
3.622612208	500
3.836045932	1000
4.331623691	5000
4.545057415	10000
5.040635174	50000
5.254068897	100000
5.749646657	500000
5.96308038	1.00E+06

A.2. INPUT FILE

Excerpts from the abaqus input file can be found below:

```
*Heading
** Job name: II508\_v74 Model name: Model-1
** Generated by: Abaqus/CAE 2019
```

A

```
*Preprint, echo=NO, model=NO, history=NO, contact=NO
**
** PARTS
**
*Part, name=IceImpactor
*Node
      1,   25.3999996,   25.3999996,           0.
.
.
.
.
 214360,   16.9686413,   33.9644165,   16.1528549
*Element, type=C3D8R
     1,   7801,   7802,  25289,  20662,     45,     46,    548,    547
.
.
.
.
206010, 149561,  18365,  16882, 145972, 214360,  19048,  16881, 149014
*Nset, nset=_PickedSet2, internal, generate
      1,  214360,       1
*Elset, elset=_PickedSet2, internal, generate
      1,  206010,       1
** Section: IceSection
*Solid Section, elset=_PickedSet2, material=Ice
,
*End Part
**
*Part, name=RigidBody
*Node
      1,          50.,          50.,           1.
.
.
.
.
    242,           0.,           0.,           0.
*Element, type=C3D8R
  1,  23,  24,  35,  34,   1,   2,  13,  12
.
.
.
.
100, 230, 231, 242, 241, 208, 209, 220, 219
*Nset, nset=_PickedSet2, internal, generate
   1,  242,    1
*Elset, elset=_PickedSet2, internal, generate
   1,  100,    1
** Section: RBSection
*Solid Section, elset=_PickedSet2, material=Ice
```

```
,
*End Part
**
**
** ASSEMBLY
**
*Assembly, name=Assembly
**
*Instance, name=IceImpactor-1, part=IceImpactor
          0.,           0.,           2.
          0.,           0.,           2., 0.577350279552042, ...
*End Instance
**
*Instance, name=RigidBody-1, part=RigidBody
*End Instance
**
*Node
      1,           0.,           0.,           0.
*Nset, nset=IceNodeSet, instance=IceImpactor-1, generate
      1,  214360,       1
*Nset, nset=_PickedSet10, internal
 1,
*Nset, nset=_PickedSet11, internal, instance=RigidBody-1, generate
   1,  242,    1
*Elset, elset=_PickedSet11, internal, instance=RigidBody-1, generate
   1,  100,    1
*Nset, nset=_PickedSet12, internal
 1,
*Nset, nset=_PickedSet13, internal, instance=IceImpactor-1
     1,     3,     4,     5,     6,     7,     8,     9,    10,    11,   ...
.
.
.
.
 16139, 16140, 16141, 16142, 16143, 16144, 16145, 16146, 16147, 16148, ...
*Elset, elset=_PickedSet13, internal, instance=IceImpactor-1
      1,      2,      3,      4,      5,      6,      7,      8,     ...
.
.
.
.
 204849, 204850, 204851, 204852, 204853, 204854, 204855, 205426, 205427, ...
*Nset, nset=_PickedSet14, internal, instance=IceImpactor-1
     2,     3,     4,     5,   217,   218,   219,   220,   221,   222,   ...
.
.
.
.
 14630, 14631, 14632, 14633, 14634, 14635, 14636, 14637, 14638, 14639, 14640 ...
```

A

```
*Elset, elset=_PickedSet14, internal, instance=IceImpactor-1
  23440,  23480,  23520,  23560,  23600,  23640,  23680,  23720,  23760,  ...
.
.
.
.
 172652, 172653, 172654, 172655, 172656, 172657, 172658, 172659, 172660 ...
*Elset, elset=_RigidSurf_S3, internal, instance=RigidBody-1, generate
   1,  100,    1
*Surface, type=ELEMENT, name=RigidSurf
_RigidSurf_S3, S3
*Surface, type=NODE, name=IceNodeSet_CNS_, internal
IceNodeSet, 1.
** Constraint: RigidBody
*Rigid Body, ref node=_PickedSet10, elset=_PickedSet11
*End Assembly
**
** MATERIALS
**
*Material, name=Ice
*Density
 9.17e-10,
*Elastic
9380., 0.33
*Plastic
 5.2,0.
 5.2,1.
*TENSILE FAILURE, SHEAR=BRITTLE,PRESS=DUCTILE
0.517
*Rate Dependent, type=YIELD RATIO
      1.,     0.
    1.01,    0.1
 1.49558,    0.5
 1.70901,     1.
 2.20459,     5.
 2.41802,    10.
  2.9136,    50.
 3.12703,   100.
 3.62261,   500.
 3.83605,  1000.
 4.33162,  5000.
 4.54506, 10000.
 5.04064, 50000.
 5.25407,100000.
 5.74965,500000.
 5.96308,  1e+06
**
** INTERACTION PROPERTIES
**
```

```
*Surface Interaction, name=ContactProp
*Friction
0.,
*Surface Behavior, pressure-overclosure=HARD
**
** BOUNDARY CONDITIONS
**
** Name: Encastre Type: Symmetry/Antisymmetry/Encastre
*Boundary
_PickedSet12, ENCASTRE
** Name: XSymm Type: Symmetry/Antisymmetry/Encastre
*Boundary
_PickedSet13, XSYMM
** Name: YSymm Type: Symmetry/Antisymmetry/Encastre
*Boundary
_PickedSet14, YSYMM
**
** PREDEFINED FIELDS
**
** Name: Velocity   Type: Velocity
*Initial Conditions, type=VELOCITY
IceNodeSet, 1, 0.
IceNodeSet, 2, 0.
IceNodeSet, 3, -32400.
** ----------------------------------------------------------------
**
** STEP: ExplicitImpact
**
*Step, name=ExplicitImpact, nlgeom=YES
*Dynamic, Explicit
, 0.0003
*Bulk Viscosity
1.2, 0.
**
** INTERACTIONS
**
** Interaction: Int-1
*Contact Pair, interaction=ContactProp, mechanical constraint=KINEMATIC, ...
... weight=1., cpset=Int-1
RigidSurf, IceNodeSet_CNS_
**
** OUTPUT REQUESTS
**
*Restart, write, number interval=1, time marks=NO
**
** FIELD OUTPUT: F-Output-1
**
*Output, field, number interval=2000
*Node Output
```

```
RT
**
** HISTORY OUTPUT: H-Output-2
**
*Output, history
*Contact Output, cpset=Int-1
CFN3,
**
** HISTORY OUTPUT: H-Output-1
**
*Output, history, variable=PRESELECT
*End Step
```

A.3. MESH CONVERGENCE & VALIDATION

Individual force-time histories from the mesh convergence analysis can be seen in figure A.1. Additional validations results for the baseline model can be seen in figure A.2. It is to be noted that the peak force results obtained for the lower velocity impacts in the current model is closer to reality than the previously published data.

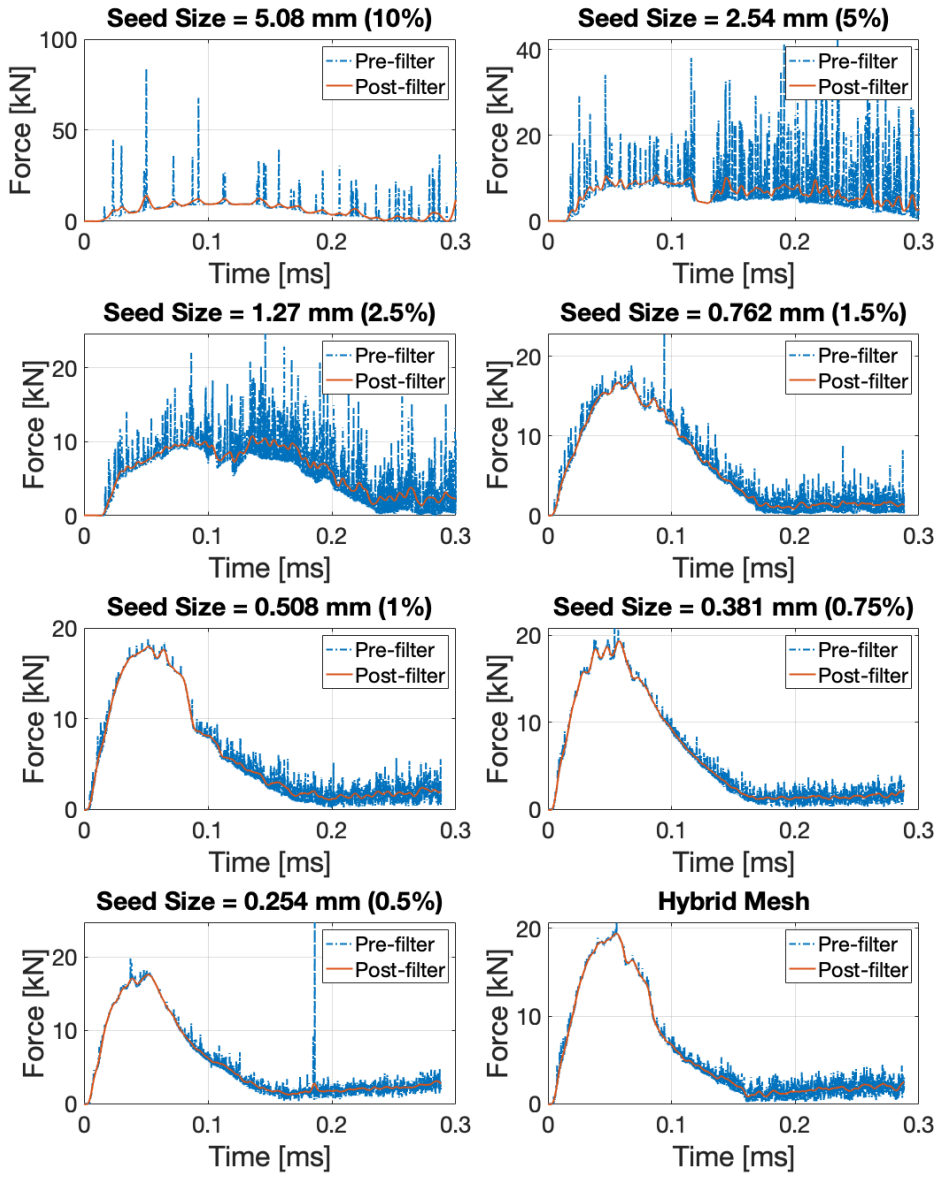

Figure A.1: Force-time histories from the mesh convergence analysis

A

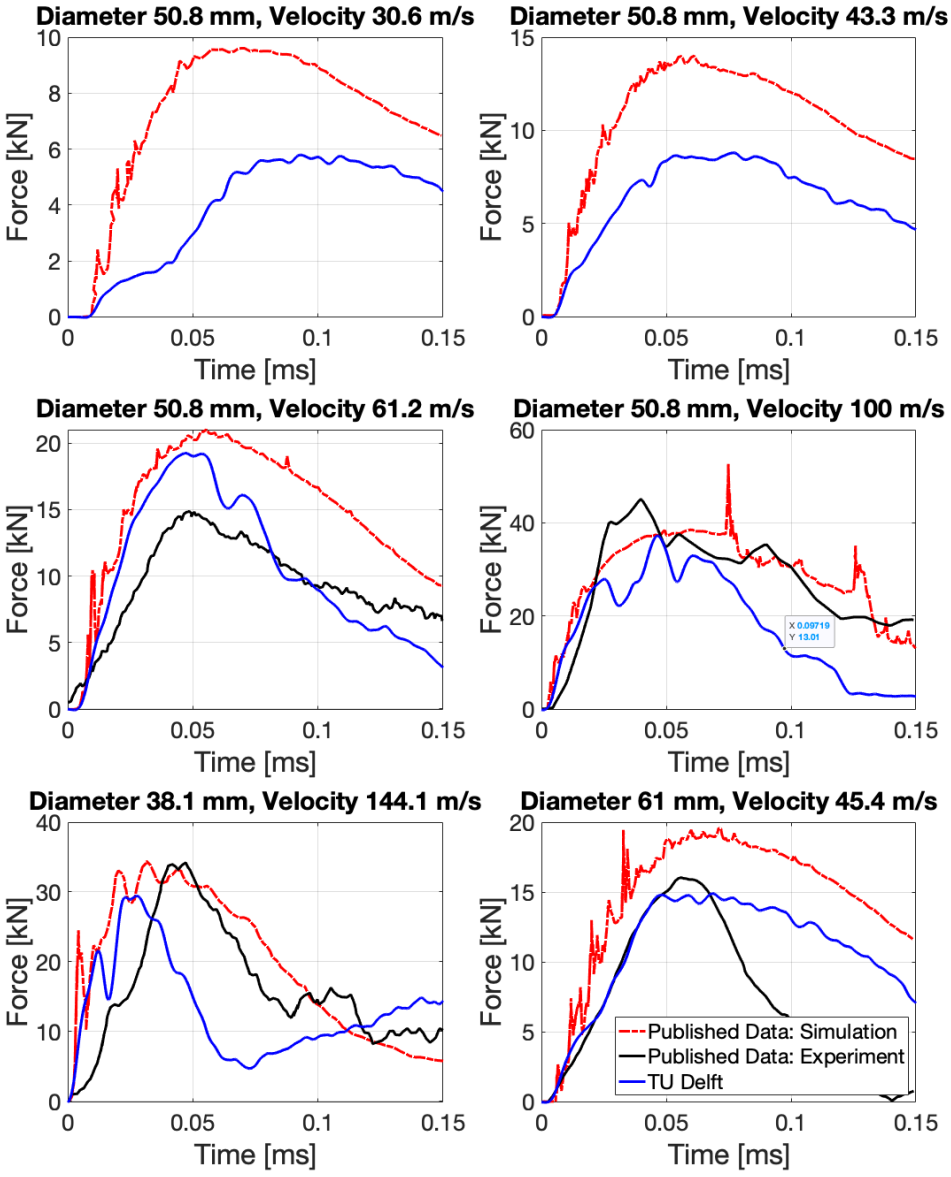

Figure A.2: Additional validation of the baseline model against published data from Tippmann et al [11]

B

Compression Tests

B.1. Pure SHI weight data

Table B.1: Weight data from pure SHI compression tests

Diameter (cm)	Expected Weight (g)	Sample 1 (g)	Sample 2 (g)	Sample 3 (g)	Sample 4 (g)	Sample 5 (g)	Average Weight (g)
1.3	1.1	0.80	0.80	1.40	1.40	1.12	1.1
2.5	7.5	7.70	7.70	8.30	8.30	8.30	8.0
3.8	26.3	28.42	28.48	29.77	29.24	29.12	29.0
4.5	43.8	46.87	48.71	48.92	48.02	46.88	47.9
5.1	63.7	69.53	69.53	69.35	68.57	68.96	69.2

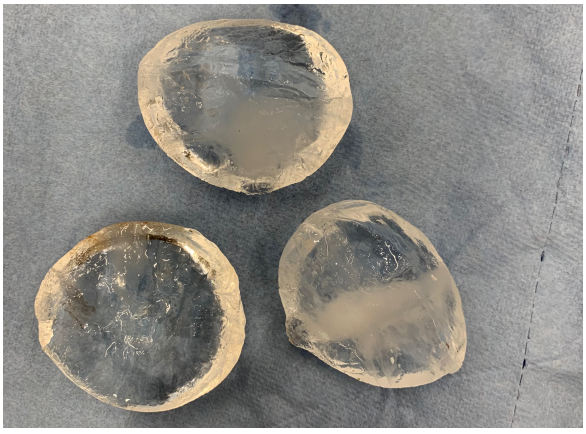

Figure B.1: Pure SHI after compression test

B.2. COTTON REINFORCED SHI WEIGHT DATA

Table B.2: Weight fraction data for cotton reinforced SHI

Diameter (cm)	10% wf (g)	5% wf (g)	2.5% wf (g)	1% wf (g)
1.3	0.12	0.06	0.03	0.01
2.0	0.42	0.21	0.10	0.04
2.5	0.82	0.41	0.21	0.09
3.8	2.89	1.44	0.72	0.30
4.5	4.79	2.40	1.20	0.50
5.1	6.98	3.49	1.74	0.73

Table B.3: Weight data from 10% wf cotton reinforced SHI compression tests

Diameter (cm)	Sample 1 (g)	Sample 2 (g)	Sample 3 (g)	Sample 4 (g)	Sample 5 (g)	Average Weight (g)
13	1.23	1.23	1.24	1.24	1.24	1.2
25	9.12	9.12	9.21	9.19	9.19	9.2
38	31.29	32.07	32.01	32.26	32.19	32.0
45	51.41	51.72	52.11	52.48	53.27	52.2
51	78.04	74.5	75.76	75.98	-	76.1

Table B.4: Weight data from 5% wf cotton reinforced SHI compression tests

Diameter (cm)	Sample 1 (g)	Sample 2 (g)	Sample 3 (g)	Sample 4 (g)	Sample 5 (g)	Average Weight (g)
13	1.19	1.18	1.22	1.22	-	1.2
25	9.08	9.08	8.66	8.50	8.50	8.8
38	31.7	29.28	31.84	29.75	29.84	30.5
45	49.5	50.25	49.46	49.51	52.54	50.3
51	71.25	71.86	72.66	71.53	73.25	72.1

Table B.5: Weight data from 2.5% wf cotton reinforced SHI compression tests

Diameter (cm)	Sample 1 (g)	Sample 2 (g)	Sample 3 (g)	Sample 4 (g)	Sample 5 (g)	Average Weight (g)
13	1.05	1.20	1.20	1.18	-	1.2
25	8.87	8.79	8.79	8.82	8.82	8.8
38	29.6	29.33	29.4	29.51	31.52	29.9
45	48.9	52.05	48.57	48.84	49.55	49.6
51	71.66	71.45	71.9	71.01	70.52	71.3

Table B.6: Weight data from 1% wf cotton reinforced SHI compression tests

Diameter (cm)	Sample 1 (g)	Sample 2 (g)	Sample 3 (g)	Sample 4 (g)	Sample 5 (g)	Average Weight (g)
13	1.18	1.18	1.18	1.18	1.12	1.2
25	8.48	8.60	8.60	8.60	8.60	8.6
38	30.59	29.14	28.92	29.52	29.87	29.6
45	48.21	49.41	48.45	49.03	49.72	49.0
51	71.2	70.39	70.51	71.85	69.21	70.6

B.3. COTTON REINFORCED SHI COMPRESSION TEST DATA

The black vertical line seen in each of these plots correspond to the same deformation point as that of pure SHI peak force. This is for the explicit purpose of comparing these results.

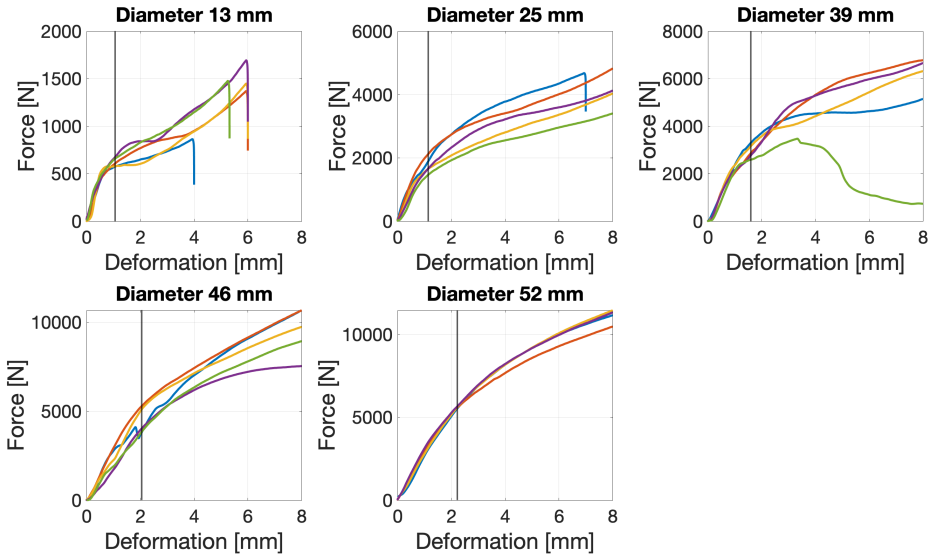

Figure B.2: Results from compression tests with 10% wf cotton reinforcement

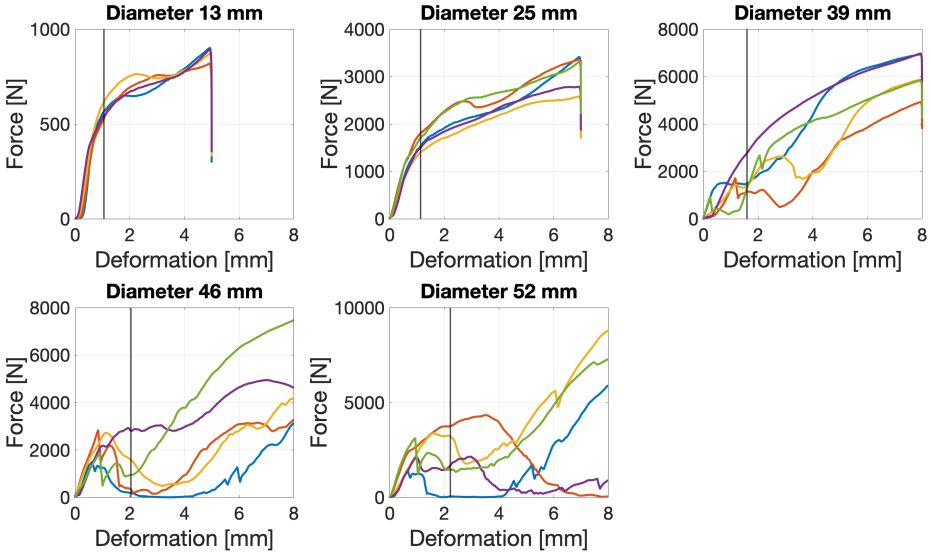

Figure B.3: Results from compression tests with 5% wf cotton reinforcement

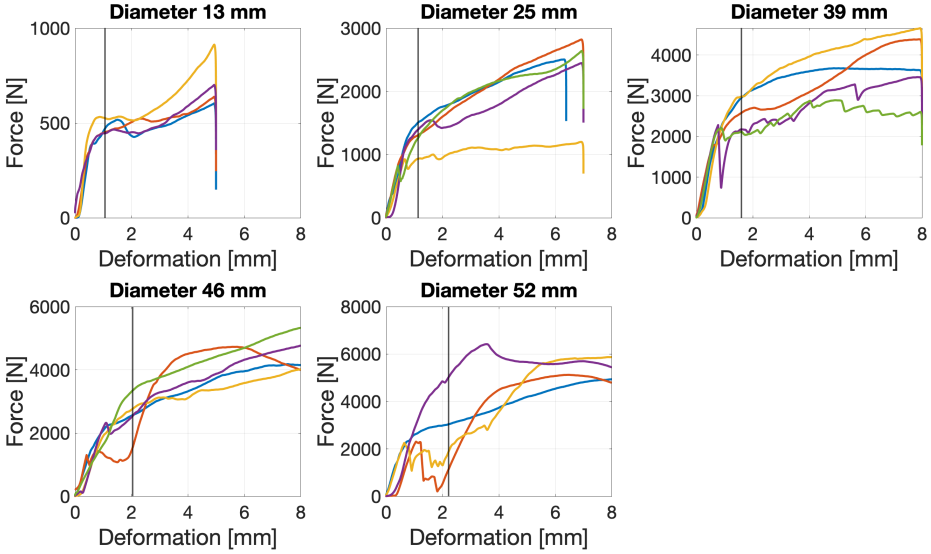

Figure B.4: Results from compression tests with 2.5% wf cotton reinforcement

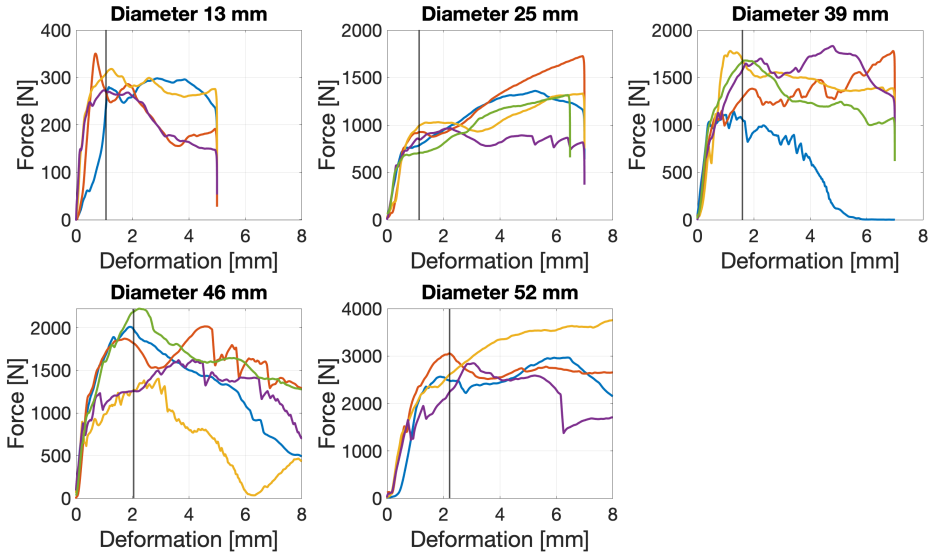

Figure B.5: Results from compression tests with 1% wf cotton reinforcement

C

IESIM MATLAB SCRIPT

```
clear
clc
close all

% Steel diameter 2.5 cm

PeakForceIce = 80; %input parameter [kN]

a = 0.0752960879014907;
b = 5.32967333365336;
c = -2.23708344794845;

PeakForceSteel = 0;
S_Vel = 0; %Steel Velocity
while (PeakForceIce - PeakForceSteel) > 0
     PeakForceSteel = (a.*S_Vel.^2) + (b.*S_Vel) + c;
     S_Vel = S_Vel + 0.00001;
end

PeakForceSteel %output check [kN]

S_Vel %output parameter [m/s]
```

D

MANUFACTURE OF FORCE MEASUREMENT SETUP

The spring compression tests were carried out using the Zwick 10kN UTM available in the DASML. Prior to testing the spring a baseline test for the flexure in the UTM was carried out and the obtained deformation was subtracted from the results obtained for the spring. The spring tests were carried out at speeds of 10 mm/min and 2000 mm/min. These results can be found in figure D.1 and D.2. The spring constant value obtained from the test carried out at 2000 mm/min was deemed more representative of an impact scenario. Hence for subsequent use in post processing results from the spring-lumped mass force measurement setup this value of 114.98 N/mm was used.

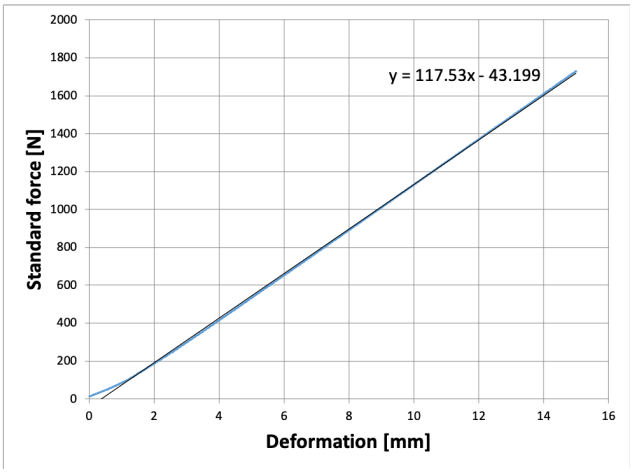

Figure D.1: Spring compression test at 10 mm/min

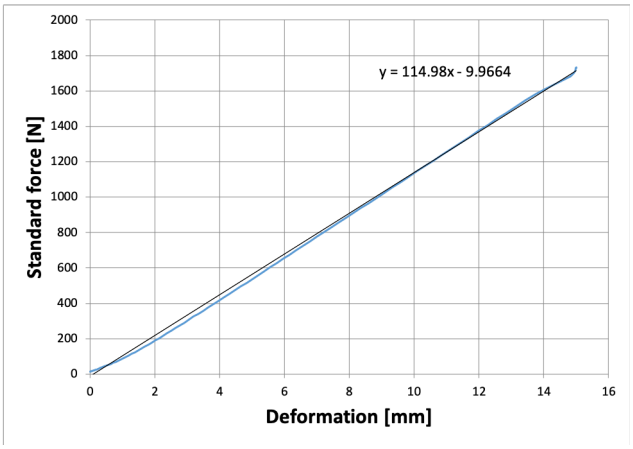

Figure D.2: Spring compression test at 2000 mm/min

The existing support wall in the impact gun enclosure in the DASML was too far away from the impact gun barrel. This implied that for very low velocity impacts with the IESIM impactor, the projectile dropped to the ground before hitting the target. For this reason a custom frame was built to bring the impactor facing lumped mass close enough to the impact gun barrel. A separation distance of 10 cm was used for all the tests. A picture of this custom frame under construction can be seen in figure D.3.

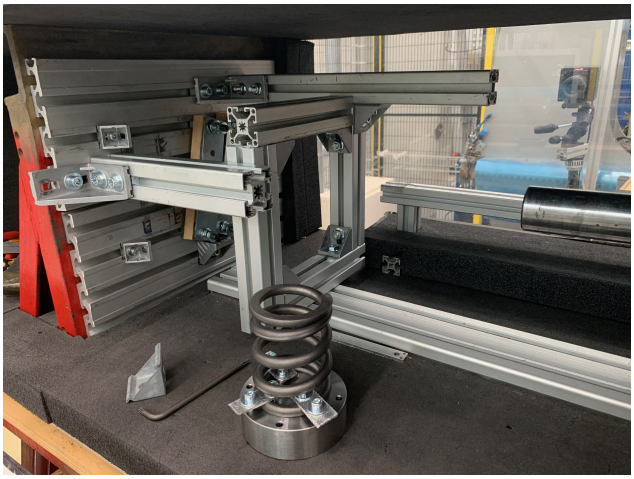

Figure D.3: Force measurement setup custom frame

The specifications of the various components involved in manually putting together the spring-lumped mass force measurement setup is listed below:

- Accelerometer: Analog Devices ADXL1004 evaluation board | Measurement range: ± 500 g | Sensitivity at 3.3 V operating voltage: 0.0027 mV/g

- Laser displacement sensor: Keyence LK-G152 | Measurement range: 150 $mm \pm 40mm$ | Accuracy: 0.5 μm | Programmed sensitivity: 0.3 mm/V
- Mass 1: Diameter: 10 cm | Height: 3.2 cm | Material: Stainless Steel 430F
- Mass 2: Diameter: 10 cm | Height: 3.5 cm | Material: Steel 52
- Compression spring: Tevema D14580 | Material: EN 10270-1-SH
- HSC: Photron FASTCAM Mini AX200 | Image resolution at 6400 fps: 1024X1024 pixels
- Data acquisition system: VTI Instruments EX1403 16 channel bridge/strain benchtop digitizer

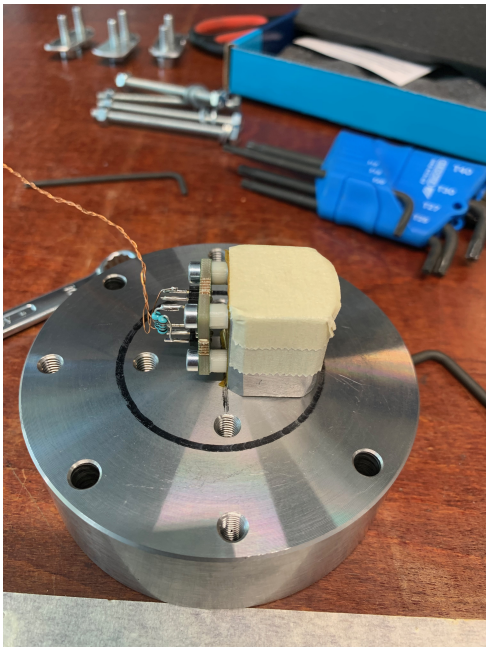

Figure D.4: Image from mounting the accelerometer to the mass and soldering the wiring

The accelerometer was not calibrated as it was brand new and pre-calibrated in the factory. The LDS was calibrated using defined blocks of known thicknesses. By adding and subtracting blocks in the path of the laser the functionality and accuracy of the system was confirmed. Figure D.5 shows this calibration process.

Figure D.5: Calibration of the LDS

E

Experimental Test Data

The summary of post processed data for key results presented in this study can be found in the tables below. Each of these data sets are accompanied by the filename of the HSC video and the CSV file with the raw data from the sensors. The full data set including the HSC footage, raw sensor data and auxiliary experiments (2, 4, 6, 7 & 9) can be found in the TU Delft research data repository.

Table E.1: Experiment set 1: Separation = 10 cms, Frame rate = 10000 fps, IESIM impactor, 1 impactor facing lumped mass = 2.044 kgs

S. No	Pressure Setting (bar)	Velocity (m/s)	Acceleration (g)	Displacement (mm)	Peak Force (N)	Video Name	CSV Name
1	0.1	0.88	209.561	0.135	4217.510	Expt_P010_1	inst0_2021-06-17_13-23-06_0
2	0.12	0.71	128.254	0.106	2585.038	Expt_P012_1	inst0_2021-06-17_14-08-24_0
3	0.14	0.69	116.829	0.104	2357.625	Expt_P014_1	inst0_2021-06-17_14-18-57_0
4	0.16	1.24	276.709	0.196	5571.575	Expt_P016_2	inst0_2021-06-17_14-28-05_0
5	0.18	1.22	315.471	0.208	6348.227	Expt_P018_1	inst0_2021-06-17_14-39-20_0
6	0.2	2.18	548.895	0.358	11044.638	Expt_P020_1	inst0_2021-06-17_14-42-58_0
7	0.22	2.51	584.920	0.413	11772.878	Expt_P022_1	inst0_2021-06-17_14-52-24_0

Table E.2: Experiment set 3: Separation = 10 cms, Frame rate = 10000 fps, IESIM impactor, 2 impactor facing lumped masses = 4.239 kgs, with ultrasonic gel

S. No	Pressure Setting (bar)	Velocity (m/s)	Acceleration (g)	Displacement (mm)	Peak Force (N)	Video Name	CSV Name
1	0.16	0.74	56.767	0.105	2372.721	Expt3_P016_1	inst0_2021-06-22_15-50-34_0
2	0.16	0.95	106.915	0.112	4458.150	Expt3_P016_2	inst0_2021-06-22_15-52-45_0
3	0.16	1.16	140.011	0.141	5836.324	Expt3_P016_3	inst0_2021-06-22_15-55-31_0
4	0.18	1.08	93.308	0.132	3895.012	Expt3_P018_1	inst0_2021-06-22_15-57-46_0
5	0.18	1.02	96.387	0.123	4022.364	Expt3_P018_2	inst0_2021-06-22_16-00-23_0
6	0.2	1.17	106.026	0.136	4424.664	Expt3_P020_1	inst0_2021-06-22_16-02-20_0
7	0.2	1.49	153.708	0.183	6409.565	Expt3_P020_2	inst0_2021-06-22_16-04-33_0
8	0.22	1.47	169.139	0.183	7051.910	Expt3_P022_1	inst0_2021-06-22_16-12-20_0
9	0.22	1.57	168.443	0.176	7023.639	Expt3_P022_2	inst0_2021-06-22_16-15-03_0
10	0.24	1.27	135.344	0.157	5644.034	Expt3_P024_1	inst0_2021-06-22_16-18-46_0
11	0.24	1.68	187.506	0.210	7817.666	Expt3_P024_2	inst0_2021-06-22_16-20-32_0
12	0.26	2.12	256.901	0.262	10708.201	Expt3_P026_1	inst0_2021-06-22_16-22-44_0
13	0.26	2.06	288.481	0.257	12017.669	Expt3_P026_2	inst0_2021-06-22_16-25-01_0

S. No	Pressure Setting (bar)	Velocity (m/s)	Acceleration (g)	Displacement (mm)	Peak Force (N)	Video Name	CSV Name
14	0.28	2.65	288.568	0.317	12031.147	Expt3_P028_1	inst0_2021-06-22_16-29-11_0
15	0.28	2.59	314.025	0.311	13086.085	Expt3_P028_2	inst0_2021-06-22_16-32-00_0
16	0.3	2.89	311.441	0.348	12984.891	Expt3_P030_1	inst0_2021-06-22_16-40-11_0
17	0.3	2.92	364.272	0.358	15181.636	Expt3_P030_2	inst0_2021-06-22_16-42-55_0
18	0.32	3.42	474.097	0.416	19751.025	Expt3_P032_1	inst0_2021-06-22_16-45-05_0
19	0.32	3.11	451.631	0.389	18816.116	Expt3_P032_2	inst0_2021-06-22_16-47-17_0
20	0.34	3.65	523.464	0.460	21808.997	Expt3_P034_1	inst0_2021-06-22_16-50-01_0
21	0.34	3.68	469.590	0.446	19568.966	Expt3_P034_2	inst0_2021-06-22_16-52-01_0
22	0.36	3.88	413.239	0.440	17224.686	Expt3_P036_1	inst0_2021-06-22_16-54-52_0
23	0.36	3.97	514.462	0.459	21437.856	Expt3_P036_2	inst0_2021-06-22_16-58-06_0
24	0.36	3.88	540.072	0.483	22500.192	Expt3_P036_3	inst0_2021-06-22_17-00-13_0
25	0.38	4.20	535.962	0.511	22336.724	Expt3_P038_1	inst0_2021-06-22_17-03-02_0

Table E.3: Experiment set 5: Separation = 10 cms, Frame rate = 30000 fps, SHI impactor, 2 impactor facing lumped masses = 4.239 kgs, with ultrasonic gel

S. No	Pressure Setting (bar)	Ice Weight (grams)	Velocity (m/s)	Acceleration (g)	Displacement (mm)	Peak Force (N)	Video Name	CSV Name
1	0.5	4.5	12.31	14.996	0.065	631.020	Expt5_P050_1	inst0_2021-06-30_16-25-05_0
2	0.5	4.1	10.36	12.798	0.051	537.898	Expt5_P050_2	inst0_2021-06-30_16-31-29_0
3	0.75	4	21.49	22.710	0.107	955.650	Expt5_P075_1	inst0_2021-06-30_16-34-22_0
4	0.75	4.2	21.82	26.313	0.114	1106.396	Expt5_P075_2	inst0_2021-06-30_16-40-01_0
5	1	4	32.00	37.251	0.162	1565.824	Expt5_P100_1	inst0_2021-06-30_15-47-48_0
6	1	4.2	32.73	34.862	0.165	1466.951	Expt5_P100_2	inst0_2021-06-30_15-50-12_0
7	1.5	-	49.66	61.611	0.268	2588.294	Expt5_P150_1	inst0_2021-06-30_15-36-12_0
8	1.5	4.4	45.00	53.967	0.250	2268.508	Expt5_P150_2	inst0_2021-06-30_15-41-38_0

S. No	Pressure Setting (bar)	Ice Weight (grams)	Velocity (m/s)	Acceleration (g)	Displacement (mm)	Peak Force (N)	Video Name	CSV Name
9	2	-	62.61	85.903	0.392	3610.130	Expt5_P200_1	inst0_2021-06-30_15-28-25_0
10	2	4.4	62.61	90.172	0.407	3790.126	Expt5_P200_2	inst0_2021-06-30_15-31-56_0
11	2.5	-	75.79	115.598	0.476	4850.619	Expt5_P250_1	inst0_2021-06-30_15-19-13_0
12	2.5	4.2	72.00	111.064	0.463	4660.150	Expt5_P250_2	inst0_2021-06-30_15-25-09_0
13	3	4	84.71	131.367	0.541	5510.287	Expt5_P300_1	inst0_2021-06-30_14-58-25_0
14	3	4.2	80.00	125.052	0.565	5250.995	Expt5_P300_2	inst0_2021-06-30_15-03-38_0
15	3.5	4.3	90.00	142.584	0.613	5982.714	Expt5_P350_1	inst0_2021-06-30_14-49-11_0
16	3.5	4.3	90.00	149.170	0.656	6260.068	Expt5_P350_2	inst0_2021-06-30_14-55-25_0
17	4	4.5	86.40	124.976	0.574	5294.196	Expt5_P400_1	inst0_2021-06-30_14-23-32_0
18	4	4.3	96.00	161.133	0.694	6758.583	Expt5_P400_2	inst0_2021-06-30_14-32-23_0
19	4.5	4.4	102.86	168.656	0.762	7073.000	Expt5_P450_1	inst0_2021-06-30_14-41-00_0
20	4.5	4.5	102.86	177.972	0.774	7463.081	Expt5_P450_2	inst0_2021-06-30_14-45-44_0
21	5	4.3	106.34	170.754	0.825	7164.891	Expt5_P500_1	inst0_2021-07-01_10-05-43_0
22	5	4.4	98.74	147.515	0.787	6194.187	Expt5_P500_2	inst0_2021-07-01_10-11-02_0
23	5.5	4.5	110.77	213.311	0.901	8938.737	Expt5_P550_1	inst0_2021-07-01_10-24-04_0
24	5.5	4.5	110.77	182.274	0.924	7651.925	Expt5_P550_2	inst0_2021-07-01_10-29-02_0
25	6	4.5	114.09	205.816	0.968	8630.693	Expt5_P600_2	inst0_2021-07-01_10-41-36_0
26	6.5	4.4	117.60	222.991	1.078	9649.744	Expt5_P650_1	inst0_2021-07-01_10-49-56_0
27	6.5	4.1	119.13	204.543	1.047	8581.746	Expt5_P650_2	inst0_2021-07-01_10-52-54_0
28	7	4.3	124.36	218.143	1.102	9146.419	Expt5_P700_1	inst0_2021-07-01_11-01-37_0
29	7	4.2	125.67	240.673	1.118	10086.258	Expt5_P700_2	inst0_2021-07-01_11-05-51_0
30	7.5	4.3	121.20	222.575	1.183	9334.437	Expt5_P750_1	inst0_2021-07-01_14-05-17_0
31	7.5	4.2	123.60	260.370	1.210	11204.448	Expt5_P750_2	inst0_2021-07-01_14-11-48_0
32	8	4.2	133.53	252.142	1.262	10566.750	Expt5_P800_1	inst0_2021-07-01_14-17-45_0
33	8	4.3	127.20	234.772	1.187	9837.079	Expt5_P800_2	inst0_2021-07-01_14-24-42_0

Table E.4: Experiment set 8: Separation = 10 cms, Frame rate = 30000 fps, Cotton reinforced SHI impactor (10% wf), 2 impactor facing lumped masses = 4.239 kgs, with ultrasonic gel

S. No	Pressure Setting (bar)	Ice Weight (grams)	Velocity (m/s)	Acceleration (g)	Displacement (mm)	Peak Force (N)	Video Name	CSV Name
1	0.5	4.3	11.08	31.667	0.070	1324.638	Expt8_P050_1	inst0_2021-07-02_10-28-18_0
2	1	4.9	30.64	82.958	0.180	3468.271	Expt8_P100_1	inst0_2021-07-02_10-33-11_0
3	1.5	4.7	46.45	95.528	0.279	4000.329	Expt8_P150_1	inst0_2021-07-02_10-36-16_0
4	2	4.9	57.60	120.535	0.391	5050.407	Expt8_P200_1	inst0_2021-07-02_10-40-01_0
5	2.5	4.8	72.00	154.772	0.502	6484.920	Expt8_P250_1	inst0_2021-07-02_10-42-42_0
6	3	4.8	80.00	179.203	0.577	7503.386	Expt8_P300_1	inst0_2021-07-02_10-45-19_0
7	3.5	4.4	84.71	192.412	0.616	8054.577	Expt8_P350_1	inst0_2021-07-02_10-48-32_0
8	4	4.5	96.00	236.486	0.721	9894.088	Expt8_P400_1	inst0_2021-07-02_10-51-40_0
9	4.5	4.5	97.48	229.901	0.729	9622.686	Expt8_P450_1	inst0_2021-07-02_10-53-55_0
10	5	4.3	101.83	225.833	0.818	9458.379	Expt8_P500_1	inst0_2021-07-02_10-57-45_0
11	5.5	4.5	108.67	260.605	0.911	10908.363	Expt8_P550_1	inst0_2021-07-05_10-26-45_0
12	6	4.3	110.40	263.847	0.952	11043.483	Expt8_P600_1	inst0_2021-07-05_10-31-23_0
13	6.5	4.4	113.14	287.135	1.025	12016.411	Expt8_P650_1	inst0_2021-07-05_10-34-57_0
14	7	4.5	114.17	261.389	1.078	10946.476	Expt8_P700_1	inst0_2021-07-05_10-39-59_0
15	7.5	4.5	117.60	290.203	1.200	12150.208	Expt8_P750_1	inst0_2021-07-05_10-44-38_0
16	8	4.4	119.31	319.439	1.196	13362.168	Expt8_P800_1	inst0_2021-07-05_10-48-51_0

F

Addressing Barrel Size Constraints

One key hurdle to overcome in order to carry out SHI impacts was the come up with a method to prevent it from melting in the metal barrel. An attempt was made to cool the barrel externally using gel packs cooled at $-22°C$. However this proved insufficient as temperatures dropped only up to $16.5°C$. The solution employed to solve this issue was to use a plastic tube to create an insulating interface between the ice impactor and metal barrel. These attempts can be seen in figure F.1.

Figure F.1: Attempts to prevent SHI from melting prior to impact

While the first hurdle was overcome, it was at the expense of the effective barrel diameter which was reduced to 2 cm. The second hurdle to overcome was this limitation of the maximum SHI diameter. An attempt was made to check if a cylindrical impactor with a hemispherical tip could effectively substitute a larger diameter SHI. The results of the geometric calculations made in this regard are shown in table F.1.

Table F.1: Cylindrical impactor with hemispherical tip geometric approximations

Diameter (mm)	**Total Volume (mm^3)**	**Cylinder Volume (mm^3)**	**Equivalent Cylinder Height (mm)**
25	8181.23	4090.62	8.33
38.1	28958.33	24867.72	50.66
50.8	68641.97	64551.36	131.50
61	118846.97	114756.36	233.78
70	179594.38	175503.76	357.53
80	268082.57	263991.96	537.80
92.5	414403.89	410313.27	835.88
105	606131.03	602040.42	1226.47

The ABAQUS model was utilised to evaluate this hypothesis and is shown in figure F.2. The results of these simulations are shown in figure F.3.

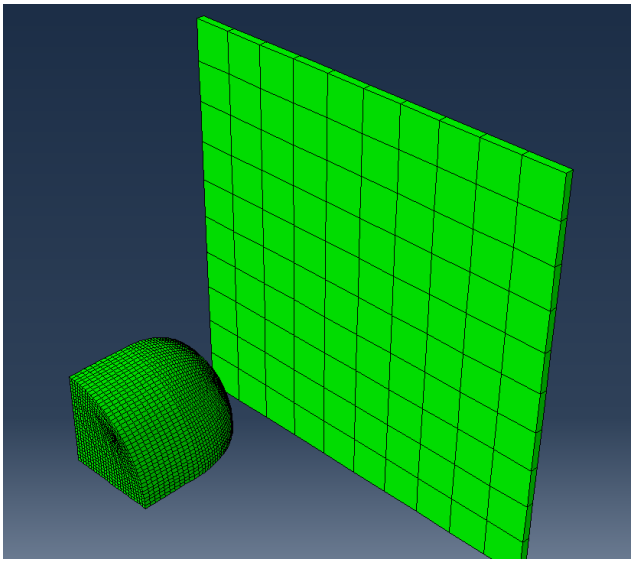

Figure F.2: Cylindrical impactor with hemispherical tip model

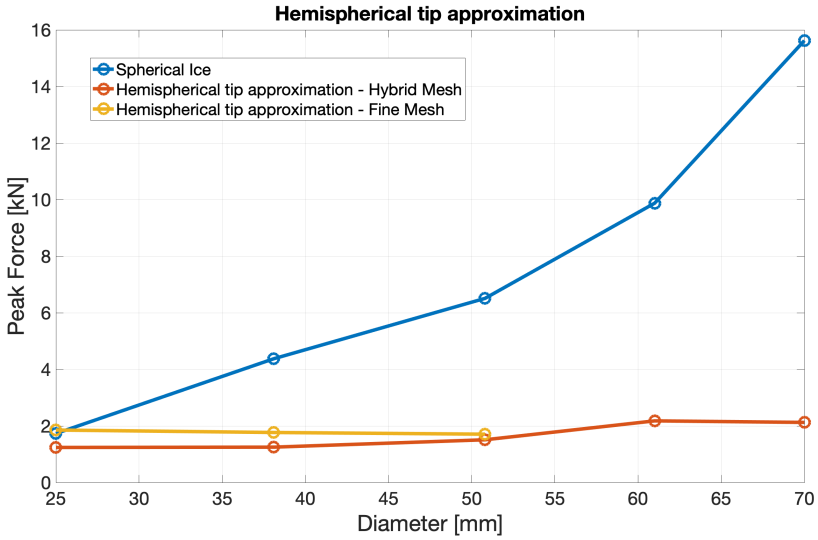

Figure F.3: Numerical simulations results of the cylinder with hemispherical tip approximation

From these results it can be inferred that this approximation does not lead to the desired results. Closer examination of the impactor damage evolution in the ABAQUS model revealed the growth of cracks across the cross-section. This prolonged the impact event but caused no significant increase in the peak impact force. In this context, all tests with SHI in this study were limited to a 2 cm diameter.

G

MANUFACTURE OF CFRP PANELS

There were a total of 18 CFRP specimens manufactured. Each specimen had an approximate dimension of 30 cm x 15 cm. These specimens were prepared in two batches. The first batch contained only 2 specimens and served as a trial run for the entire procedure. The other 16 samples were prepared in one batch to ensure equal properties. The procedure followed to prepare these 16 samples is described in this chapter.

Aerospace grade Hexcel HexPly 8552 unidirectional CFRP prepreg with a roll width of 1.2 m was used. Individual ply's were cut as per the cutting plan shown in figure G.1 using the Gerber cutting machine available in the DASML. The result of this process is shown in figure G.2.

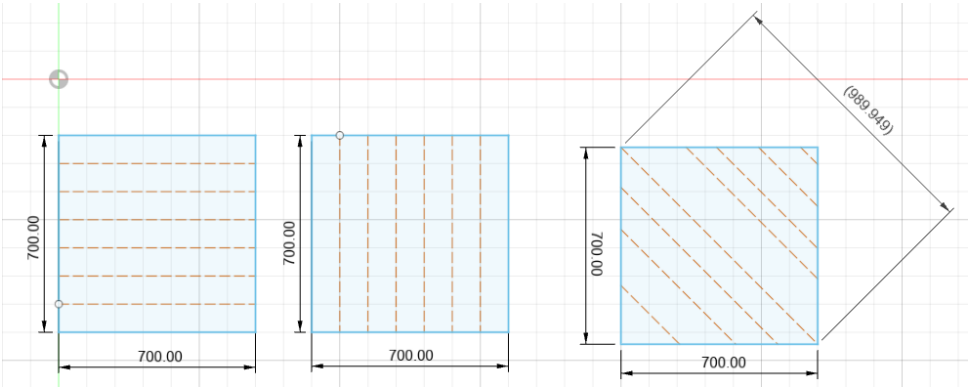

Figure G.1: Ply cutting plan (units are in cm)

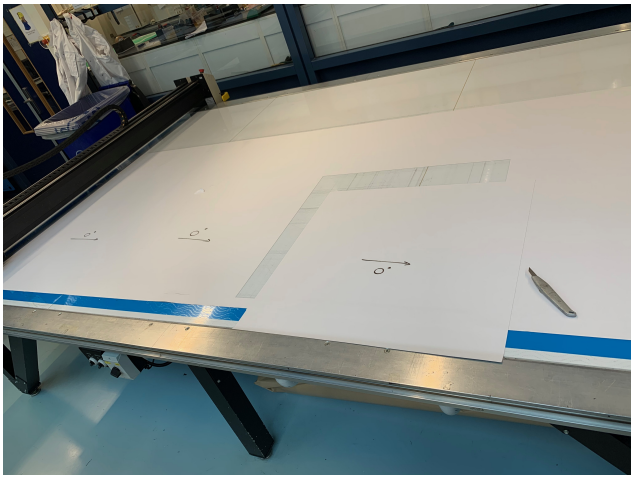

Figure G.2: Gerber cutting machine

Two sets of 8 plies were stacked together side-by-side on a large autoclave plate using hand layup with a stacking sequence as follows: $[0\ 45\ 90\ -45]_s$. After the layup of each layer de-bulking was carried out with a vacuum pump for 3 minutes. Some pictures from this process are shown in figure G.3.

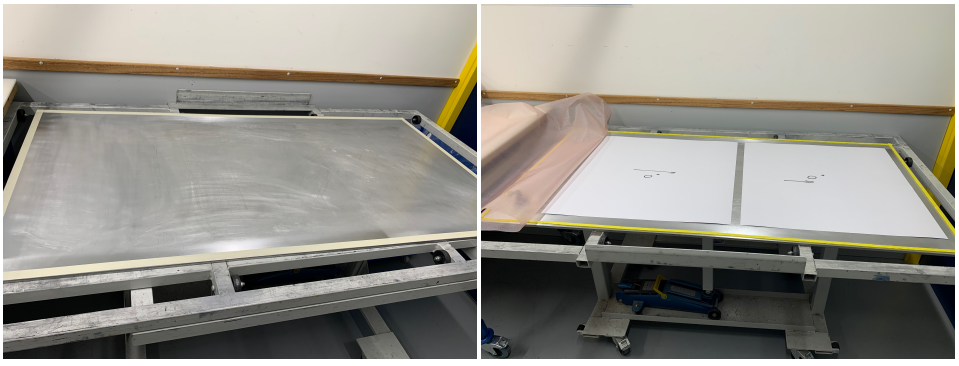

Figure G.3: Autoclave plate and hand layup process

Following the hand layup, the plate was vacuum bagged and loaded up into the autoclave as shown in figure G.4. The autoclave was programmed to follow the recommended temperature and pressure cycle mentioned in the material data sheet [89]. This cure cycle is reproduced in figure G.5.

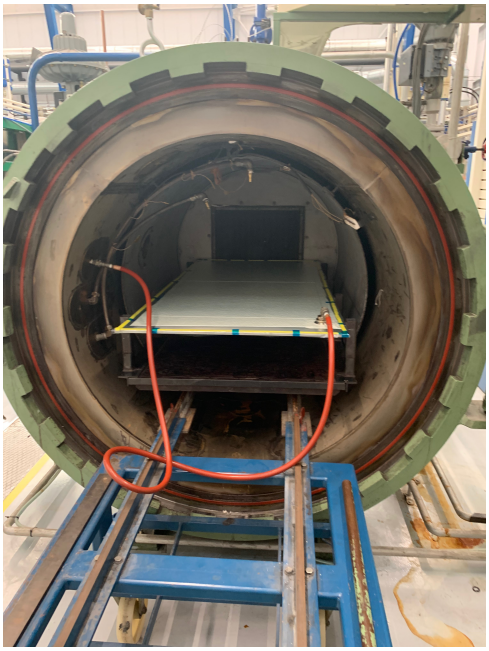

Figure G.4: Autoclave with specimens prior to curing

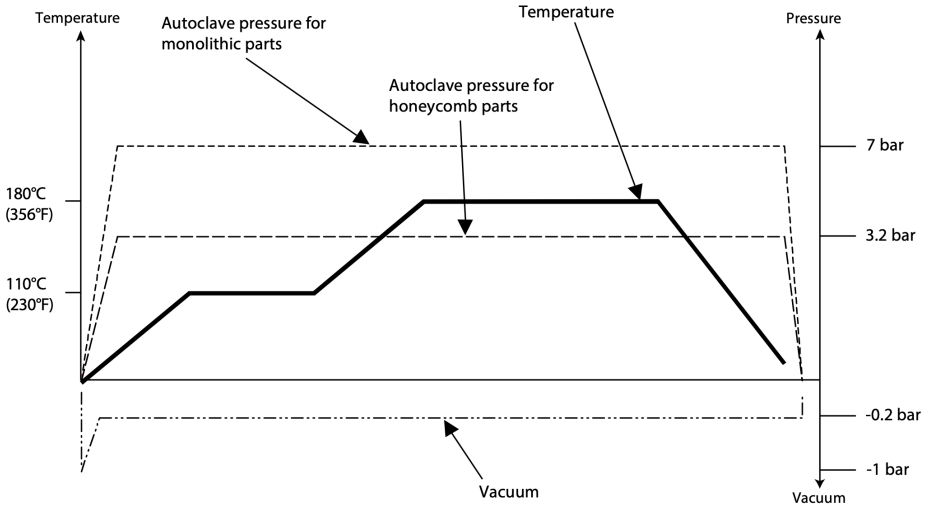

Figure G.5: Autoclave cure cycle [89]

Following the cure cycle, the vacuum bag and auxiliary layers were removed. The laminates were marked (see figure G.6) and cut with a diamond saw (see figure G.7). Note that sufficient spacing was provided at the edges and along cutting lines. This was

done in order to minimise defects and to avoid dimension loss from the thickness of the diamond saw.

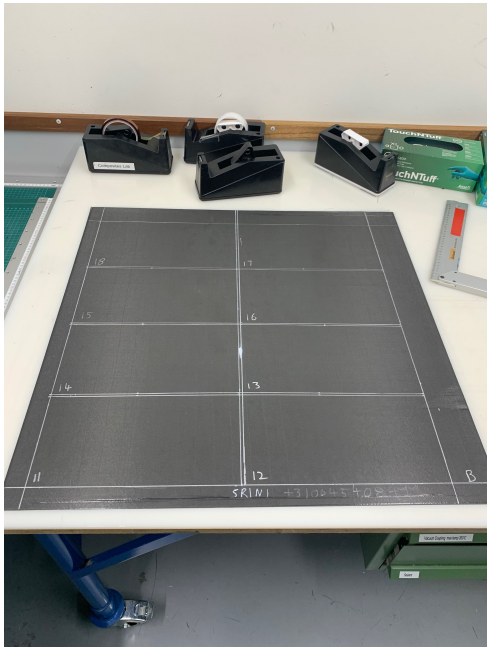

Figure G.6: Laminate with markings for cutting

Figure G.7: Laminate cutting with diamond saw

H

C-SCAN OF CFRP PANELS

Quality control check was performed on the laminates after manufacturing by subjecting them to a c-scan in the DASML (see figure H.1). The results of this c-scan can be seen in figure H.2 and H.3. A difference of over 4dB in the recorded signal is considered a delamination or defect. From these scans it is clear that there were no manufacturing defects.

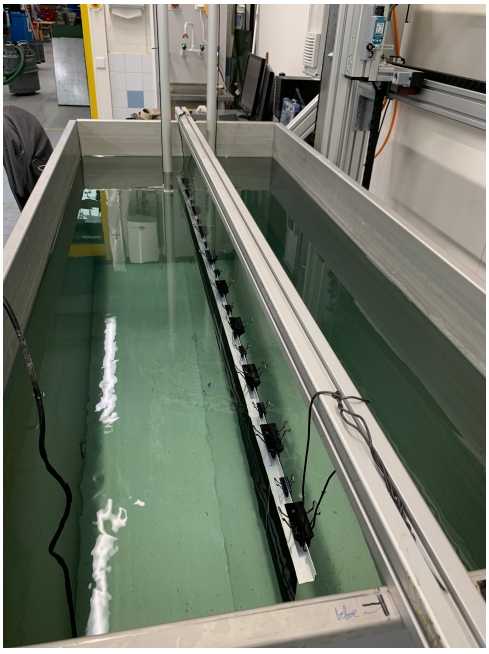

Figure H.1: C-scan in the DASML

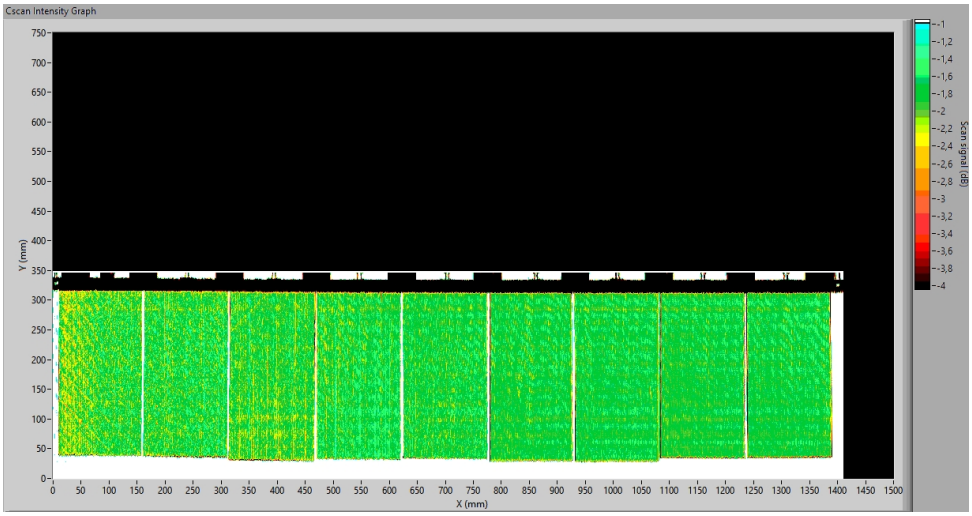

Figure H.2: C-scan results for samples 1 to 9

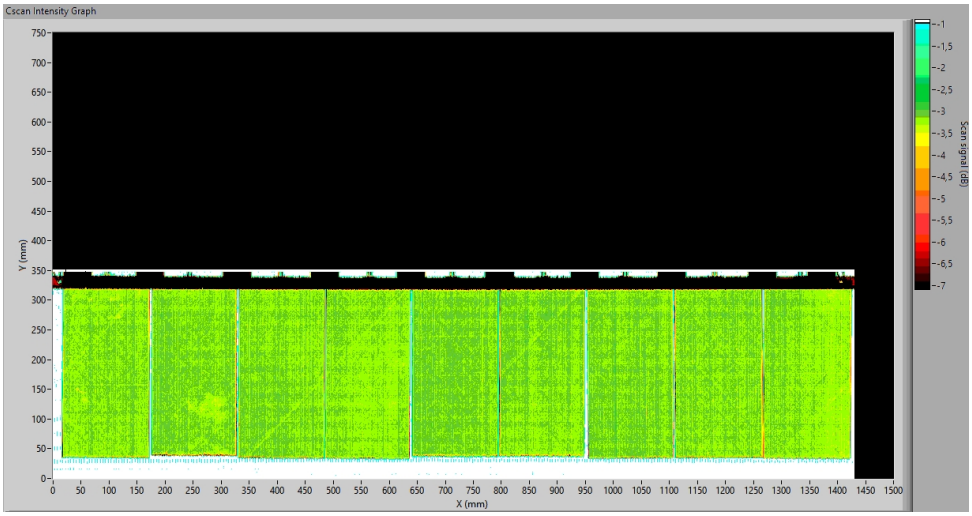

Figure H.3: C-scan results for samples 10 to 18

In order to confirm damage initiation indeed starts at 12 m/s or above for these CFRP panels with an IESIM impactor, repeated impacts at 11 m/s were carried out. These impacts were carried out on panel number 11 at the centre. Figure H.4 confirms that damage is not initiated under these conditions.

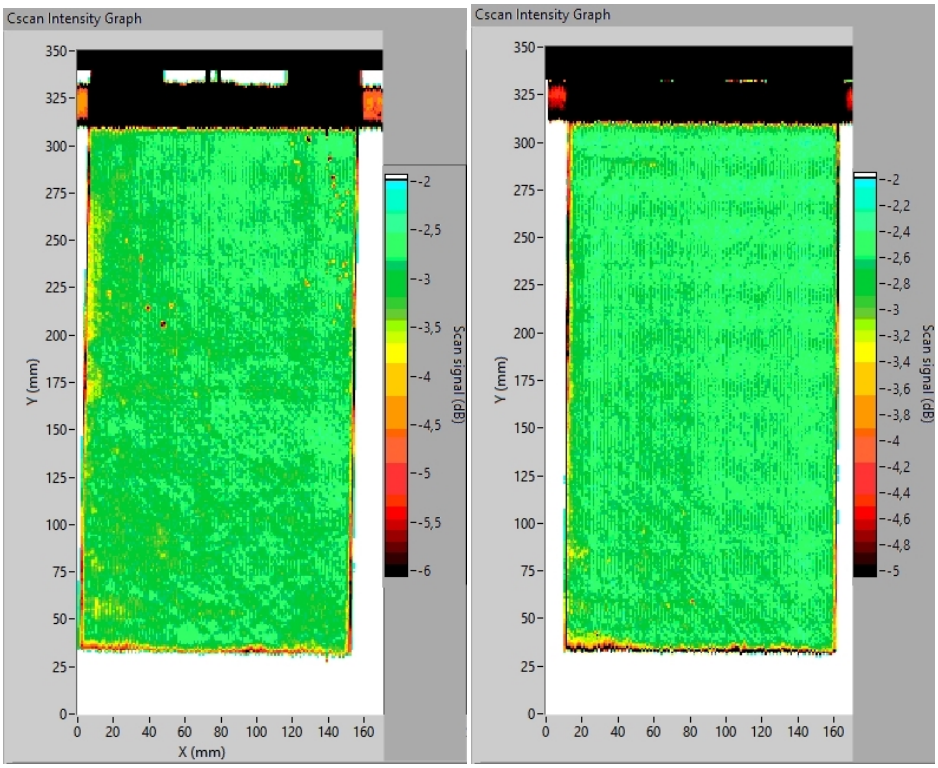

Figure H.4: C-scan after two impacts (left) and three impacts (right) with IESIM impactor at 11 m/s

REFERENCES

[1] Boeing, *Flight Routes for Boeing 787 Dreamliner family [Accessed on 01/11/2020],* (2019).

[2] R. Anand, *Everywhere You Can Fly the Airbus A350 in 2018 [Accessed on 01/11/2020],* (2018).

[3] A. F. Prein and G. J. Holland, *Global estimates of damaging hail hazard,* Weather and Climate Extremes **22**, 10 (2018).

[4] T. Púcik, C. Castellano, P. Groenemeijer, T. Kühne, A. T. Rädler, B. Antonescu, and E. Faust, *Large hail incidence and its economic and societal impacts across Europe,* Monthly Weather Review **147**, 3901 (2019).

[5] A. Heymsfield, M. Szakáll, A. Jost, I. Giammanco, and R. Wright, *A comprehensive observational study of graupel and hail terminal velocity, mass flux, and kinetic energy,* Journal of the Atmospheric Sciences **75**, 3861 (2018).

[6] C. A. Knight and N. C. Knight, *Very Large Hailstones from Aurora, Nebraska,* Bull. Amer. Meteor. Soc., 86 , 1773 (2005).

[7] P. Field, W. Hand, G. Cappelluti, A. McMillan, A. Foreman, D. Stubbs, and M. Willows, *Hail Threat Standardisation (EASA)*, Tech. Rep. (2010).

[8] I. M. Giammanco, T. M. Brown, R. G. Grant, D. L. Dewey, J. D. Hodel, and R. A. Stumpf, *Evaluating the hardness characteristics of hail through compressive strength measurements,* Journal of Atmospheric and Oceanic Technology **32**, 2100 (2015).

[9] J. L. Sánchez, B. Gil-Robles, J. Dessens, E. Martin, L. Lopez, J. L. Marcos, C. Berthet, J. T. Fernández, and E. García-Ortega, *Characterization of hailstone size spectra in hailpad networks in France, Spain, and Argentina,* Atmospheric Research **93**, 641 (2009).

[10] J. Sun, N. Lam, L. Zhang, D. Ruan, and E. Gad, *Contact forces generated by hailstone impact,* International Journal of Impact Engineering **84**, 145 (2015).

[11] J. D. Tippmann, H. Kim, and J. D. Rhymer, *Experimentally validated strain rate dependent material model for spherical ice impact simulation,* International Journal of Impact Engineering **57**, 43 (2013).

[12] D. K. Siorikis, C. S. Rekatsinas, C. V. Nastos, T. C. Theodosiou, N. A. Chrysochoidis, A. P. Christoforou, A. S. Yigit, and D. A. Saravanos, *Experimental and numerical assessment of dynamics of hailstone impact on composite plates,* COMPDYN Proceedings **3**, 4342 (2019).

[13] D. Saini and B. Shafei, *Prediction of extent of damage to metal roof panels under hail impact,* Engineering Structures **187**, 362 (2019).

[14] P. Flüeler, M. Stucki, F. Guastala, and T. Egli, *Hail Impact Resistance of Building Materials Testing , Evaluation and Classification,* 11DBMC International Conference on Durability of Building Materials and Components (2008).

[15] S. Perera, N. Lam, M. Pathirana, L. Zhang, D. Ruan, and E. Gad, *Deterministic solutions for contact force generated by impact of windborne debris,* International Journal of Impact Engineering **91**, 126 (2016).

[16] G. Marsh, *Airbus takes on Boeing with reinforced plastic A350 XWB,* Reinforced Plastics **51** (2007), 10.1016/S0034-3617(07)70383-1.

[17] M. O. Richardson and M. J. Wisheart, *Review of low-velocity impact properties of composite materials,* Composites Part A: Applied Science and Manufacturing **27**, 1123 (1996).

[18] R. M. Groves, *Comprehensive Composite Materials II*, Vol. 3 (Elsevier Ltd., 2017) pp. 300–311.

[19] C. Kassapoglou, *Composite Structural Components and Mathematical Formulation,* in *Design and Analysis of Composite Structures: With Applications to Aerospace Structures* (John Wiley and Sons, Ltd, 2010) Chap. 5, pp. 63–117.

[20] *Hailstorm Pounds Planes in Denver; United Says 31 Planes Took Damage [Accessed on 31-10-2020],* (2001).

[21] K. L. Painter, *Frontier Airlines planes damaged by hail in Denver returned to service [Accessed on 31-10-2020],* (2014).

[22] A. Ahles, *American Airlines Cancels 296 flights At DFW Airport [Accessed on 01/11/2020],* .

[23] M. Johanson, *Dallas Tornadoes 2012: DFW Airport Planes Damaged, Hundreds of Flights Canceled [Accessed on 01/11/2020],* (2012).

[24] S. Rieger, *A Canadian fix for Calgary weather: WestJet protects planes from hail with hockey boards [Accessed on 31-10-2020],* (2020).

[25] *Composite Damage Tolerance and Maintenance Safety Issues [Accessed on 01/11/2020],* (2006).

[26] C. Fualdes, *Composites @ Airbus damage tolerance methodology,* in *Proceedings of the FAA workshop for composite damage tolerance and maintenance*, 1 (2006) p. 40.

[27] A. J. Fawcet and G. D. Oakes, *Boeing composite airframe damage tolerance and service experience,* in *Proceedings of the FAA workshop for composite damage tolerance and maintenance* (2006) pp. 1–32.

[28] EASA, *AMC 20-29: Composite Aircraft Structure,* (2010).

[29] FAA, *AC 20-107B: Composite Aircraft Structure,* (2010).

[30] A. Court and J. Griffiths, *Thunderstorm Morphology and Dynamics, Kessler E (ed.). University of Oklahoma Press: Norman, USA* (1986) pp. 9–40.

[31] W. H. Hand and G. Cappelluti, *A global hail climatology using the UK Met Office convection diagnosis procedure (CDP) and model analyses,* Meteorological Applications **18**, 446 (2011).

[32] J. P. Tuovinen, A. J. Punkka, J. Rauhala, H. Hohti, and D. M. Schultz, *Climatology of severe hail in Finland: 1930-2006,* Monthly Weather Review **137**, 2238 (2009).

[33] H. Höller and M. E. Reinhardt, *The Munich Hailstorm of July 12, 1984 - Convective Development and Preliminary Hailstone Analysis,* (1986).

[34] J. T. Quinlivan and H. R. Fenbert, *Composite Applications in Commercial Transport Aircraft,* in *Polymers and Other Advanced Materials: Emerging Technologies and Business Opportunities*, edited by P. N. Prasad, J. E. Mark, and T. J. Fai (Springer US, Boston, MA, 1995) pp. 1–5.

[35] J. Walton, *Where are all the unused planes right now? [Accessed on 31-10-2020],* (2020).

[36] J. Dessens, C. Berthet, and J. L. Sanchez, *Change in hailstone size distributions with an increase in the melting level height,* Atmospheric Research **158-159**, 245 (2015).

[37] H. J. Punge and M. Kunz, *Hail observations and hailstorm characteristics in Europe: A review,* Atmospheric Research **176-177**, 159 (2016).

[38] P. Groenemeijer, T. Púcik, A. M. Holzer, B. Antonescu, K. Riemann-Campe, D. M. Schultz, T. Kühne, B. Feuerstein, H. E. Brooks, C. A. Doswell, H. J. Koppert, and R. Sausen, *Severe convective storms in Europe: Ten years of research and education at the European Severe Storms Laboratory,* Bulletin of the American Meteorological Society **98**, 2641 (2017).

[39] T. M. Brown-giammanco and I. M. Giammanco, *An Overview of the IBHS Hail Research Program,* , 1 (2017).

[40] I. M. Giammanco, M. R. Kumjian, and A. J. Heymsfield, *Observations of Hailstone Sizes and Shapes from the IBHS Hail Measurement Program: 2012-2014,* 27th Conference on Severe Local Storms , 1 (2014).

[41] W. Monfredo, *Investigation into the record hailstone on 23 July 2010 at Vivian, South Dakota, USA,* Weather **66**, 216 (2011).

[42] S. Perera, N. Lam, M. Pathirana, L. Zhang, D. Ruan, and E. Gad, *Probabilistic modelling of forces of hail,* Natural Hazards **91**, 133 (2018).

[43] D. A. Paterson and R. Sankaran, *Hail impact on building envelopes,* Journal of Wind Engineering and Industrial Aerodynamics **53**, 229 (1994).

[44] J. A. P. Laurie, *Hail and its effects on buildings,* Council for Scientific and Industrial Research **Rep. 176**, 12 pp (1960).

[45] A. Theis, S. Borrmann, S. K. Mitra, A. J. Heymsfield, and M. Szakáll, *A wind tunnel investigation into the aerodynamics of lobed hailstones,* Atmosphere **11**, 1 (2020).

[46] S. E. Petty, *Forensic Engineering: Damage Assessments for Residential and Commercial Structures* (2013).

[47] J. Pernas-Sánchez, J. A. Artero-Guerrero, D. Varas, and J. López-Puente, *Experimental analysis of normal and oblique high velocity impacts on carbon/epoxy tape laminates,* Composites Part A: Applied Science and Manufacturing **60**, 24 (2014).

[48] H. Kim, D. A. Welch, and K. T. Kedward, *Experimental investigation of high velocity ice impacts on woven carbon/epoxy composite panels,* Composites Part A: Applied Science and Manufacturing **34**, 25 (2003).

[49] J. S. Marshall and W. M. K. Palmer, *THE DISTRIBUTION OF RAINDROPS WITH SIZE,* Journal of Meteorology **5**, 165 (1948).

[50] L. Cheng, M. English, and R. Wong, *Hailstone size distributions and their relationship to strom thermodynamics,* (1985).

[51] R. Fraile, A. Castro, and J. L. Sánchez, *Analysis of hailstone size distributions from a hailpad network,* Atmospheric Research **28**, 311 (1992).

[52] B. Federer and A. Waldvogel, *Hail and Raindrop Size Distributions from a Swiss Multicell Storm,* J. Appl. Meteor. **14**, 91 (1975).

[53] J. Grieser and M. Hill, *How to express hail intensity—modeling the hailstone size distribution,* Journal of Applied Meteorology and Climatology **58**, 2329 (2019).

[54] ASTM, *Standard Test Method for Hail Impact Resistance of Aerospace Transparent Enclosures,* F320 16 , 1 (2016).

[55] ANSI, *American National Standard for Impact Resistance Testing of Rigid Roofing Materials by Impacting with Freezer Ice Balls,* ANSI FM 4473 2011 (R2020) (2020).

[56] ASTM, *Standard Practice for Determining Resistance of Solar Collector Covers to Hail by Impact With Propelled Ice Balls,* E822 92 (2015), 10.1520/E0822-92R15.

[57] ASTM, *Standard Test Method for Determining Resistance of Photovoltaic Modules to Hail by Impact with Propelled Ice Balls 1,* E1038 10 (2019), 10.1520/E1038-10R19.

[58] H. Kim, J. Nightingale, and H. Park, *Impact damage resistance of composite panels impacted by cotton-filled and unfilled ice,* ICCM International Conferences on Composite Materials , 1 (2007).

[59] M. Mahinfalah and R. A. Skordahl, *The effects of hail damage on the fatigue strength of a graphite/epoxy composite laminate,* Composite Structures **42**, 101 (1998).

[60] H. Kim and K. T. Kedward, *Modeling hail ice impacts and predicting impact damage initiation in composite structures,* AIAA Journal **38**, 1278 (2000).

[61] R. Juntikka and R. Olsson, *Experimental and modelling study of hail impact on composite plates,* ICCM International Conferences on Composite Materials (2009).

[62] H. Park and H. Kim, *Damage resistance of single lap adhesive composite joints by transverse ice impact,* International Journal of Impact Engineering **37**, 177 (2010).

[63] M. A. Lavoie, M. Nejad Ensan, and A. Gakwaya, *Development of an efficient numerical model for hail impact simulation based on experimental data obtained from pressure sensitive film,* Mechanics Research Communications **38**, 72 (2011).

[64] P. Guégan, R. Othman, D. Lebreton, F. Pasco, P. Villedieu, J. Meyssonnier, and S. Wintenberger, *Critical impact velocity for ice fragmentation,* Proceedings of the Institution of Mechanical Engineers, Part C: Journal of Mechanical Engineering Science **226**, 1677 (2012).

[65] J. Rhymer, H. Kim, and D. Roach, *The damage resistance of quasi-isotropic carbon/epoxy composite tape laminates impacted by high velocity ice,* Composites Part A: Applied Science and Manufacturing **43**, 1134 (2012).

[66] R. Olsson, R. Juntikka, and L. E. Asp, *Solid Mechanics and its Applications*, Vol. 192 (2012) pp. 427–489.

[67] J. Pernas-Sánchez, J. A. Artero-Guerrero, D. Varas, and J. López-Puente, *Analysis of Ice Impact Process at High Velocity,* Experimental Mechanics **55**, 1669 (2015).

[68] J. Pernas-Sánchez, J. A. Artero-Guerrero, D. Varas, and J. López-Puente, *Experimental analysis of ice sphere impacts on unidirectional carbon/epoxy laminates,* International Journal of Impact Engineering **96**, 1 (2016).

[69] S. Dousset, J. Girardot, F. Dau, and A. Gakwaya, *Prediction procedure for hail impact,* EPJ Web of Conferences **183**, 1 (2018).

[70] G. Luo, Y. Mo, C. Wu, F. Zhang, L. Liu, and W. Chen, *Experimental study of ice impact on aluminium/carbon fiber reinforced composite dual plate,* International Journal of Crashworthiness **0**, 1 (2020).

[71] A. Prato and M. L. Longana, *A novel approach for the investigation of low energy ice impacts,* International Journal of Impact Engineering **121**, 12 (2018).

[72] J. Petrovic, *Review Mechanical properties of ice and snow,* Journal of Materials Science **8**, 1 (2003).

[73] E. M. Schulson, *Brittle failure of ice,* Engineering Fracture Mechanics **68**, 1839 (2001).

[74] H. Kim and J. N. Keune, *Compressive strength of ice at impact strain rates,* Journal of Materials Science **42**, 2802 (2007).

[75] M. Shazly, V. Prakash, and B. A. Lerch, *High strain-rate behavior of ice under uniaxial compression,* International Journal of Solids and Structures **46**, 1499 (2009).

[76] K. S. Carney, D. J. Benson, P. DuBois, and R. Lee, *A phenomenological high strain rate model with failure for ice,* International Journal of Solids and Structures **43**, 7820 (2006).

[77] J. Pernas-Sánchez, J. A. Artero-Guerrero, J. López-Puente, and D. Varas, *Numerical methodology to analyze the ice impact threat: Application to composite structures,* Materials and Design **141**, 350 (2018).

[78] K. Liu, J. L. Liu, and Z. Wang, *A damage threshold prediction model of CFRP panel by hail impact based on delamination mechanism,* Engineering Fracture Mechanics **239**, 107282 (2020).

[79] J. D. Rhymer and H. Kim, *Prediction of delamination onset and critical force in carbon/epoxy panels impacted by ice spheres,* Computers, Materials and Continua **35**, 87 (2013).

[80] ASTM International, *Designation: D7136/D7136M - 12 "Standard test method for measuring the damage resistance of a fiber-reinforced polymer matrix composite to a drop-weight impact event",* Annual Book of ASTM Standards **i**, 1 (2012).

[81] W. J. Cantwell and J. Morton, *Comparison of the low and high velocity impact response of cfrp,* Composites **20**, 545 (1989).

[82] A. Verstraeten, *Hail Impact on Composite Aircraft: Investigation of low-velocity impacts in multiple impact loactions and effect on its fatigue life,* Ph.D. thesis, TU Delft (2019).

[83] L. Huo and R. C. Alderliesten, *The comprehensive comparison of behaviour of CFRP laminates subjected to ice and steel impacts (Unpublished),* .

[84] L. A. Coles, A. Roy, N. Sazhenkov, L. Voronov, M. Nikhamkin, and V. V. Silberschmidt, *Ice vs. steel: Ballistic impact of woven carbon/epoxy composites. Part I – Deformation and damage behaviour,* Engineering Fracture Mechanics **225**, 106270 (2018).

[85] L. A. Coles, A. Roy, and V. V. Silberschmidt, *Ice vs. steel: Ballistic impact of woven carbon/epoxy composites. Part II – Numerical modelling,* Engineering Fracture Mechanics **225**, 106297 (2018).

[86] H. Liu, J. Liu, C. Kaboglu, H. Chai, X. Kong, B. R. Blackman, A. J. Kinloch, and J. P. Dear, *Experimental investigations on the effects of projectile hardness on the impact response of fibre-reinforced composite laminates,* International Journal of Lightweight Materials and Manufacture **3**, 77 (2020).

[87] S. W. Spronk, M. Kersemans, J. C. De Baerdemaeker, F. A. Gilabert, R. D. Sevenois, D. Garoz, C. Kassapoglou, and W. Van Paepegem, *Comparing damage from low-velocity impact and quasi-static indentation in automotive carbon/epoxy and glass/polyamide-6 laminates,* Polymer Testing **65**, 231 (2018).

[88] S. Yourkowski, *777 Tour Facts Data [Accessed on 03/08/2021],* (2003).

[89] Hexcel, *HexPly 8552 material datasheet [Accessed on 04/08/2021],* (2011).